To the Graduate Council:

I am submitting herewith a thesis written by Stanford T. Verigood entitled "Analysis of Simulated Planar Waves Using an Air Jet Distortion Generator in a Gas Turbine Engine Ground Test Facility." I have examined the final copy of this thesis for form and content and recommend that it be accepted in partial fulfillment of the requirements for the degree of Master of Science, with a major in mechanical engineering.

Trevor Moulden, Major Professor

We have read this thesis
and recommend its acceptance:

Roger Crawford

Roy J. Schulz

Accepted for the Council:

Associate Vice Chancellor
and Dean of The Graduate School

STATEMENT OF PERMISSION TO USE

In presenting this thesis in partial fulfillment of the requirements for a Master's degree at The University of Tennessee, Knoxville, I agree that the library shall make it available to borrowers under the rules of the library. Brief quotations from this thesis are allowable without special permission, provided that accurate acknowledgment of the source is made.

Permission for extensive quotation from or reproduction of this thesis may be granted by my major professor, or in his absence, by the Head of Interlibrary Services when, in the opinion of either, the proposed use of the material is for scholarly purposes. Any copying or use of the material in this thesis for financial gain shall not be allowed without my written permission.

Signature A. Vaigovo

Date 7/26/95

ANALYSIS OF SIMULATED PLANAR WAVES USING AN AIR JET DISTORTION GENERATOR IN A GAS TURBINE ENGINE GROUND TEST FACILITY

A Thesis

Presented for the

Master of Science

Degree

The University of Tennessee, Knoxville

Stanford T. Verigood

August 1995

DEDICATION

This Thesis is dedicated to Jesus Christ, the King of kings and Lord of lords.

Every good and perfect gift comes from above, from the Father of lights. James 1:17

ACKNOWLEDGMENTS

The test program was conducted at the Arnold Engineering Development Center (AEDC), Air Force Material Command (AFMC) at the request of the Aeronautical Systems Center (ASC/YFZ), Wright-Patterson AFB, Ohio, under Program Element 63230F. The results of the test were obtained by Sverdrup Technology Inc., (a Sverdrup Corporation company), operating contractor of the AEDC propulsion test facilities, Arnold Air Force Base, Tennessee, under Air Force Project No. BB67AA.

I would like to thank my parents, Stanley and Helen Verigood, who encouraged me and said "you can do it" when I didn't think I could, regardless of what "it" was. Additionally, my wife and children deserve much credit for their patience and support during many long years of academic endeavor. I would also like to thank the USAF and Sverdrup Technology Inc. for the educational opportunities they provided. Finally, I want to thank my major professor, Dr. Trevor Moulden, for his patience and guidance and the other committee members, Dr. Roger Crawford and Dr. Roy Schulz for their comments and assistance.

ABSTRACT

This Thesis evaluated the qualitative and quantitative features of unsteady total-pressure distortion introduced into the inlet of a gas turbine engine during test in a ground test facility. The distortion was created in the form of spatially uniform planar waves that travel normal to the engine face and have discrete frequencies of five and fifteen Hertz. These frequencies are representative of typical sinusoidal planar waves encountered during flight tests of various high-performance jet aircraft.

An Air Jet Distortion Generator (AJDG) created the waves in the Arnold Engineering Development Center's (AEDC) Aeropropulsion Systems Test Facility (ASTF) test cell C-1 in an attempt to simulate a planar pulse inlet distortion pattern. Spatial distortion descriptors for radial intensity and circumferential extent and intensity using SAE Aerospace Recommended Practice (ARP) 1420 guidelines were calculated to evaluate the spatial uniformity of the generated planar wave. Additionally, a Fast Fourier Transform (FFT) technique was used to determine the spectral content of the waves.

Analysis indicated that the waves are representative of a spatially uniform, discrete planar wave. The AJDG did not add an appreciable amount of spatial distortion, no more than approximately 2.0%, and overall levels of distortion are comparable to those seen in typical direct-connect type test configurations. Also, spectral analysis indicated the frequency content of the waves was concentrated in the desired bands.

TABLE OF CONTENTS

SECTION	PAGE
1. INTRODUCTION	1
1.1 Overview	1
1.2 Description of PWD	3
1.3 Examples of PWD	4
1.4 Summary	6
2. TEST PROGRAM DESCRIPTION	7
2.1 Background	7
2.2 Test Facility	7
2.3 Instrumentation	10
2.4 Transducer Response	11
2.5 Test Objectives	11
2.6 Test Procedure	12
3. DATA ANALYSIS	14
3.1 Overview	14
3.2 SAE 1420 Distortion Analysis Details	14
3.3 Circumferential Descriptors	15
3.4 Radial Descriptor	16
3.5 PSD Methodology	17
3.6 Fourier Analysis Details	17
3.7 PSD Data Presentation	20
4. RESULTS AND DISCUSSION	22
4.1 Distortion Analysis Overview	22
4.2 Probe Substitution	22

4.3 Data Presentation Overview 23
4.4 5 Hertz Wave Distortion Results 25
4.5 15 Hertz Wave Distortion Results 27
4.6 Distortion Results Summary 27
4.7 DFT Results Overview 28
4.8 5 Hertz Wave Fourier Results 30
4.9 15 Hertz Wave Fourier Results 31
5. CONCLUDING REMARKS 32
5.1 Summary 32
BIBLIOGRAPHY 33
APPENDIX 36
VITA 75

LIST OF TABLES

TABLE		PAGE
1.	Rake and Probe Substitution Summary	46
2.	Individual Probe Pressures from Data Point 65 "Pre-Peak"	47
3.	Data Point 65 "Pre-Peak" Reduced Data	47
4.	Individual Probe Pressures from Data Point 65 "Peak"	49
5.	Data Point 65 "Peak" Reduced Data	49
6.	Individual Probe Pressures from Data Point 65 "Post-Peak"	51
7.	Data Point 65 "Post-Peak" Reduced Data	51
8.	Individual Probe Pressures from Data Point 65 "Pre-Valley"	53
9.	Data Point 65 "Pre-Valley" Reduced Data	53
10.	Individual Probe Pressures from Data Point 65 "Valley"	55
11.	Data Point 65 "Valley" Reduced Data	55
12.	Individual Probe Pressures from Data Point 65 "Post-Valley"	57
13.	Data Point 65 "Post-Valley" Reduced Data	57
14.	Individual Probe Pressures from Data Point 179 "Pre-Peak"	59
15.	Data Point 179 "Pre-Peak" Reduced Data	59
16.	Individual Probe Pressures from Data Point 179 "Peak"	61
17.	Data Point 179 "Peak" Reduced Data	61
18.	Individual Probe Pressures from Data Point 179 "Post-Peak"	63
19.	Data Point 179 "Post-Peak" Reduced Data	63
20.	Individual Probe Pressures from Data Point 179 "Pre-Valley"	65
21.	Data Point 179 "Pre-Valley" Reduced Data	65
22.	Individual Probe Pressures from Data Point 179 "Valley"	67
23.	Data Point 179 "Valley" Reduced Data	67

24. Individual Probe Pressures from Data Point 179 "Post-Valley" 69

25. Data Point 179 "Post-Valley" Reduced Data 69

26. Average Distortion Indices 71

LIST OF FIGURES

FIGURE		PAGE
1.	Direct-Connect Test Configuration	37
2.	Categories of Planar Wave Distortion	37
3.	Local Flow Separation on the B-1B Inlet Ramp at Off-Design, Low Airflow	38
4.	B-1B Inlet Duct Resonance at Mach 0.85	38
5.	Time History of F-16 inlet Instability	39
6.	YF120-GE-100 Installation in Test Cell C-1	39
7.	Inlet Duct Configuration Details	40
8.	AJDG/PP and Inlet Rake Configuration Relative to the Engine Face	40
9.	Functional Schematic of the AJDG/PP System in C-1	41
10.	AJDG Strut Details	42
11.	Functional Schematic of the AJDG Airflow Distribution System	43
12.	Logic Block Diagram for the AJDG Airflow Distribution System	43
13.	AIP Rake and Probe Location Details	44
14.	Definition of Ring Circumferential Distortion Extent and Intensity	45
15.	Definition of Ring Radial Distortion Intensity	45
16.	AJDG Created Planar Waveforms	46
17.	Data Point 65 "Pre-Peak" Ring Average Total Pressure	47
18.	Data Point 65 "Pre-Peak" Circumferential and Radial Distortion Intensity	48
19.	Data Point 65 "Pre-Peak" Circumferential Extent	48
20.	Data Point 65 "Peak" Ring Average Total Pressure	49
21.	Data Point 65 "Peak" Circumferential and Radial Distortion Intensity	50
22.	Data Point 65 "Peak" Circumferential Extent	50
23.	Data Point 65 "Post-Peak" Ring Average Total Pressure	51

24. Data Point 65 "Post-Peak" Circumferential and Radial Distortion Intensity 52
25. Data Point 65 "Post-Peak" Circumferential Extent 52
26. Data Point 65 "Pre-Valley" Ring Average Total Pressure 53
27. Data Point 65 "Pre-Valley" Circumferential and Radial Distortion Intensity 54
28. Data Point 65 "Pre-Valley" Circumferential Extent 54
29. Data Point 65 "Valley" Ring Average Total Pressure 55
30. Data Point 65 "Valley" Circumferential and Radial Distortion Intensity 56
31. Data Point 65 "Valley" Circumferential Extent 56
32. Data Point 65 "Post-Valley" Ring Average Total Pressure 57
33. Data Point 65 "Post-Valley" Circumferential and Radial Distortion Intensity 58
34. Data Point 65 "Post-Valley" Circumferential Extent 58
35. Data Point 179 "Pre-Peak" Ring Average Total Pressure 59
36. Data Point 179 "Pre-Peak" Circumferential and Radial Distortion Intensity 60
37. Data Point 179 "Pre-Peak" Circumferential Extent 60
38. Data Point 179 "Peak" Ring Average Total Pressure 61
39. Data Point 179 "Peak" Circumferential and Radial Distortion Intensity 62
40. Data Point 179 "Peak" Circumferential Extent 62
41. Data Point 179 "Post-Peak" Ring Average Total Pressure 63
42. Data Point 179 "Post-Peak" Circumferential and Radial Distortion Intensity 64
43. Data Point 179 "Post-Peak" Circumferential Extent 64
44. Data Point 179 "Pre-Valley" Ring Average Total Pressure 65
45. Data Point 179 "Pre-Valley" Circumferential and Radial Distortion Intensity 66
46. Data Point 179 "Pre-Valley" Circumferential Extent 66
47. Data Point 179 "Valley" Ring Average Total Pressure 67
48. Data Point 179 "Valley" Circumferential and Radial Distortion Intensity 68
49. Data Point 179 "Valley" Circumferential Extent 68

50. Data Point 179 "Post-Valley" Ring Average Total Pressure 69
51. Data Point 179 "Post-Valley" Circumferential and Radial Distortion Intensity 70
52. Data Point 179 "Post-Valley" Circumferential Extent 70
53. Average Radial Distortion for Data Points 65 and 179 71
54. Average Circumferential Distortion for Data Points 65 and 179 71
55. PSD of a 5 Hertz, Unity Amplitude, Cosine Wave 72
56. PSD of a 15 Hertz, Unity Amplitude, Cosine Wave 72
57. Data Point 65: 5 Hz. Planar Wave Power Spectral Density 73
58. Data Point 179: 15 Hz. Planar Wave Power Spectral Density 74

LIST OF TERMS

A16	Engine Flowpath Area
AEDC	Arnold Engineering Development Center
AIP	Aerodynamic Interface Plane
AIR	Aerospace Information Report
AJDG/PP	Air Jet Distortion Generator - Planar Pulse System
ALF	Aft Looking Forward
AMT	Accelerated Mission Test
ARP	Aerospace Recommended Practice
ASTF	Aeropropulsion System Test Facility
ATF	Advanced Tactical Fighter
DFT	Discrete Fourier Transform
DoD	Department of Defense
DPC/P	Circumferential Distortion Itensity Index (percent)
DPR/P	Radial Distortion Intensity Index (percent)
EGMS	Exhaust Gas Management System
FFT	Fast Fourier Transform
FOD	Foreign Object Damage
GE	General Electric
Hz	Hertz (cycles per second)
IRD	Industry Review Draft
Mach no.	Ratio of Velocity to Speed of Sound
MPR	Multiple-per-Revolution
N	Number of Samples (Integer)
NASA	National Aeronautics and Space Administration
NIST	National Institute of Standards and Technology
P	Power
P0	Test Cell Pressure (psia)
P1	Engine Inlet Pressure (psia)
PAV	Ring Average Presssure (psia)
PAVLOW	Average Low Pressure (psia)
PC	Personal Computer
PCN2R	Percent Corrected Compressor Speed (percent)
PFAV	Compressor Face Average Pressure (psia)
PLA	Power Lever Angle (degrees)
Pman	Airjet Manifold Pressure (psia)
PMEL	Precision Measurement Equipment Laboratory
PSD	Power Spectral Desnsity
Pt	Total Pressure (psia)
PWD	Planar Wave Distortion
Q	Low Pressure Region Counter (Integer)
RMS	Root Mean Square
SAE	Society of Automotive Engineers

SLS	Sea Level Static
T	Fourier Sampling Interval (seconds)
T. O.	Technical Order
T1	Engine Inlet Temperature (Fahrenheit)
USAF	United States Air Force
$W(s)$	Window Function
WIB	Engine Inbleed Flow Rate (pounds per second)
$X(k)$	Fourier Transform Value at k
e	Exponential
f	Frequency (Hertz)
i	Imaginary Number = $\sqrt{-1}$
k	Fourier Coefficient Index (Integer)
n	Discrete Time Sample Number (Integer)
s	Frequency Offset in Bins (Integer)
t	Time (seconds)
w	Parzen Window Function
$x(t)$	Function Evaluated at Time t
θ	Circumferential Extent (degrees)

Superscripts

-	Circumferential Low Pressure Region

Subscripts

c	Critical Sampling Frequency (Hertz)
i	Ring Number (Integer)
j	Window Function Index Counter (Integer)
k	Low Pressure Region Counter (Integer)
s	Sampling Frequency (Hertz)

1. INTRODUCTION

1.1 Overview

The increasing complexity of airborne weapon systems combined with the need to reduce development costs presents designers of such systems with significant challenges. For example, engine developers must shorten development times, test less, provide longer and more comprehensive warranties while continuing to lower engine costs. Obviously, these are competing objectives but they are not necessarily mutually exclusive. For example, the Pratt & Whitney F100-PW-100 engine developed in the early seventies underwent development testing but was still fraught with myriad problems that did not surface until it began its operational life. The Air Force was then forced to spend millions of dollars to correct the deficiencies uncovered during the initial operational life of the F100. Some of these problems were the result of management decisions while others were inherent in the design of the engine (Drewes, 1987). A more complete understanding of the operational service cycle of the engine along with more comprehensive and realistic test techniques would have uncovered some of the flaws. Problems detected early in the development cycle of an engine are easier and less costly to fix. Therefore, a detailed and comprehensive test program is essential.

The F119-PW-100, the USAF's newest engine, will undergo a much more rigorous and well defined ground test program before production begins than did the F100. That is, operability and durability testing will be based on expected "real-world" service cycles. Similarly, the F100-PW-229, the latest incarnation of the venerable F100, must also undergo a rigorous series of Accelerated Mission Test cycles (AMT's) in a ground test facility. These "mission" cycles are an attempt to simulate the wear and tear an engine will endure during operational service. By cycling the throttle or power lever angle (PLA) between various power settings from idle to maximum augmentation or afterburner

the most severe aspects of a gas turbine engine's service life can be duplicated. These cycles, accumulated at an accelerated rate relative to normal service life, may uncover problems that would result from operational service. For example, "fatigue type" problems may manifest themselves during this accelerated "aging" process. As the deficiencies become evident, sufficient lead time exists to correct them before the operational engines are afflicted. In short, development testing must accurately reflect the environment that the engine will see during operational service. The use of efficient, comprehensive ground test techniques will shorten development times, provide a more mature engine when put into operational service and result in lower life-cycle costs.

This thesis will describe and evaluate one such test technique that can be used during turbine engine ground testing. Specifically, a technique for simulating a planar-wave inlet distortion pattern (PWD) was implemented at the Arnold Engineering Development Center (AEDC) using the Air Jet Distortion Generator/Planar Pulse system (AJDG/PP). The test article was a YF120-GE-100 engine with a generic inlet duct common to direct-connect ground test configurations. Figure 1[1] illustrates the direct-connect type test configuration discussed in this thesis.

Planar-wave distortion is an in-phase, one-dimensional, spatially uniform pressure disturbance represented by the change of inlet total pressure with time at the Aerodynamic Interface Plane (AIP). A comprehensive description of planar wave distortion is given in the following section. The wave, normal to the engine face, can have a deleterious effect on engine compression system stability as the examples in section 1.3 serve to illustrate.

---

[1]All Figures are presented sequentially in the Appendix.

1.2 Description of PWD

For standardization purposes throughout the aerospace industry the Society of Automotive Engineers (SAE) has developed several definitions for use in dealing with engine inlet distortion. These include the Aerodynamic Interface Plane (AIP), the pressure probe/rake array and spatial distortion descriptors (SAE ARP 1420, 1978). The AIP is the instrumentation plane at the aerodynamic interface of the inlet and engine and is used to define distortion performance for the system being tested. The rake/probe array used is generally a compromise between pattern measurement accuracy, data acquisition system complexity and rake induced flow blockage (SAE AIR 1419, 1983). A comprehensive discussion of the merits of various rake/probe arrays and configurations is given in SAE AIR 1419. SAE AIR 1419 also discusses transducer and probe characteristics in terms of frequency response and probe size. It is generally concluded that a 40 probe array (8 rakes of 5 probes each) is the minimum probe density allowable to obtain reasonably accurate measurements without adversely affecting the flow field entering the engine (SAE AIR 1419, 1983). This is the configuration used during the test reported in this thesis. The detailed location of the rakes and probes are explained in section 2.3 below. Spatial distortion descriptors, which are defined in section 3.2, are used to characterize the inlet distortion in terms of severity and extent. For example, what is the magnitude of the pressure defect (intensity) and how much of the compressor face is affected (extent)? These spatial descriptors will be used to define the spatial uniformity of the planar wave evaluated in this thesis.

Planar waves are also defined in terms of their time-history and power. To quote from the SAE Industry Review Draft (IRD), 1990 report on planar waves, "Planar waves can be categorized through use of the power spectral density (PSD) of the time-varying compressor-face-average total-pressure recovery. That is, planar waves are defined for the N probes of an inlet AIP rake-probe array as follows:

$$P(t) = \frac{1}{N}\sum_{i=1}^{N} P_i(t)$$

where $P_i(t)$ is the time-varying total-pressure at the i-th probe and $P(t)$ is the time-varying spatial-average total pressure at the AIP". Planar waves may be, sinusoidal with a discrete frequency, periodic with multiple discrete frequencies, random with broad-band energy content or random plus harmonic. Figure 2 illustrates the categories of PWD and lists some potential sources for these disturbances. Additionally, spatial distortion, as described above, may be superimposed on the wave form. Non-planar and non spatially-uniform waves are not considered in this thesis. However, this is not a limitation of the AJDG but of the scope of the test project reported herein.

1.3 Examples of PWD

As a first example of a PWD problem, a NASA Dryden F-111A with steady-state and dynamic pressure probes experienced supersonic inlet buzz at Mach numbers from 1.8 to 2.1 (Burcham and Hughes, 1970). Analysis conducted on data from Mach 2.0 at 44,300 feet indicate a discrete planar wave frequency of 27 Hz and the presence of a significant circumferential spatial distortion component. It is unclear whether the circumferential distortion and the PWD are related. It may be recalled that the F-111 is an aircraft that has a well documented history of engine/inlet compatibility problems.

Secondly, a B-1B experienced at least three incidents involving planar-wave distortion (MacMiller and Hagenson, 1986). The first circumstance occurred when an inlet duct resonance was excited at a low inlet mass flow ratio during high Mach number flight with the aircraft under leeward sideslip. Local separation and reattachment of the flow along an inlet ramp excited a duct resonance which resulted in an 11 Hz planar distortion wave at the engine face. Figure 3 shows the location of local flow separation and reattachment along the ramp surface forward of the cowl. Figure 4 shows power spectral

density (PSD) and time-trace data of the instability. A second incident occurred when an environmental control system precooler excited a duct resonance during a "no-flow" condition. The RMS wave amplitude of approximately 2.4 psi. was high enough to cause structural failure in this system and several instances of foreign object damage (FOD) during the flight test program were attributed to this cause. Finally, the wake vortex from an extended nose gear assembly was ingested by the inlet and resulted in a planar wave distortion pattern. This incident resulted in the installation of a movable cowl lip which was scheduled to respond to both nose gear position and aircraft Mach number. This cowl lip on the inlet duct was found to attenuate nose gear induced planar waves in the inlet and hence at the engine face.

Lastly, an F-16 with an untested air data probe experienced an 8 Hz planar-wave phenomenon at Mach 1.97 and 30,000 feet during an engine control mode change (McCallum, 1989). Figure 5 presents time-trace data for this case. PSD data were unavailable for this situation.

All of the aircraft in the preceding examples experienced compressor stalls during these recorded planar-wave distortion events. Fortunately, compressor instability was the only effect of this inlet distortion and all the aircraft recovered safely. However, that may not always be the case and if such flows were encountered repeatedly, more severe consequences could result. Clearly, these examples serve to illustrate the need for a test methodology to evaluate the effects of planar-wave distortion on newly designed aircraft engines. As the integration of airframes and engines along with their respective control systems continues to evolve, the need for this capability will be more acute. This is especially true considering the financial and physical constraints mentioned earlier.

1.4 Summary

This thesis discusses the use of AEDC's Air Jet Distortion Generator/Planar Pulse system, described in section 2.2, to create a planar wave in the inlet of a turbine engine during ground testing. Specifically, the thesis will evaluate the "quality" of the planar wave in terms of SAE Aerospace Recommended Practice (ARP) 1420 total-pressure spatial distortion descriptors. Additionally, Fourier analysis in the form of power spectral densities (PSD), are used to evaluate the spectral content of the generated waves. The evaluation of the planar wave's effect on compressor stability is beyond the scope of this thesis and is not reported. This omission however, does not detract from the overall relevance or importance of this work. Steenken, 1988, gives a methodology to account for stability margin loss due to planar wave distortion.

In summary, this work will show, using the techniques mentioned, that the AJDG created planar wave introduced into the inlet of an engine under test had the following characteristics:

1. The planar wave was spatially uniform. That is, use SAE ARP 1420 analysis techniques to show that the spatial distortion level in the wave is at or below those levels typical for a direct-connect type engine test.
2. The wave was sinusoidal or periodic in nature. Specifically, use an FFT technique to show that the frequency of the wave was concentrated in the desired band and that random frequencies or high amplitude harmonic frequency components were not significant.

The total-pressure data recorded during the test discussed in this thesis was provided to the author in ASCII format for analysis and evaluation for the purpose of reporting on the AEDC's Airjet Distortion Generator Planar Pulse system. The author's contribution to the test program was limited to the SAE 1420 distortion analysis and PSD analysis of the transient data on a post-test basis for reporting in this thesis.

2 TEST PROGRAM DESCRIPTION

2.1 Background

During the late 1980's the USAF sponsored a competition to determine what engine would power the service's new Advanced Tactical Fighter (ATF). The Air Force determined that a new engine should be developed, rather than using a derivative of an existing power plant, to take advantage of newly developed technologies and to provide capability for future growth. Additionally, the USAF wanted to develop the airframe and engine concurrently, as an integrated system, rather than trying to mate separately developed components later in the design cycle.

The fierce competition pitted the General Electric F120 against the Pratt & Whitney F119. Both engines are low bypass ratio, mixed flow, augmented turbofans. Much of the competition was conducted in the Aeropropulsion Systems Test Facility (ASTF) at AEDC and included operability, performance and durability testing. This thesis concerns a test technique used during a portion of the operability test of the General Electric YF120-GE-100 engine in ASTF test cell C-1.

2.2 Test Facility

ASTF is a large gas turbine engine test facility capable of providing a wide range of simulated flight conditions covering most of the flight envelope of modern aircraft. The facility utilizes multiple air-supply compressors along with temperature conditioning equipment, including mechanical refrigeration and natural gas fired heaters, to supply air at the appropriate pressure and temperature to the engine under test. Exhaust compressors are used to evacuate the test cell to the correct pressure (altitude). Because the facility is of an open-circuit configuration with separate air-supply and exhaust machines, test periods are limited only by practical considerations such as personnel availability, machine

maintenance requirements and mechanical failures. A typical test period will last about 14 hours. During that time multiple flight conditions and test article configurations can be tested. A complete description of ASTF including the air supply machinery, exhaust machinery, air temperature conditioning equipment and system operating modes is given in Mitchell, 1972.

C-1 is a propulsion development test cell which is 28-ft in diameter and 50-ft-long. The facility is capable of providing a range of flight conditions from sea level static (SLS) to approximately Mach 3.8 (with true temperature) and altitudes up to about 100,000 feet. The actual conditions available are dependent on airflow and temperature requirements. The cell inlet consists of a 22-ft-diameter settling plenum, flow measuring venturis, and a flow straightening grid overlaid with a 20-mesh screen for foreign object damage (FOD) prevention. A labyrinth type air seal coupled the engine to the plenum via a system of generic inlet ducts. The labyrinth seal isolates the fixed inlet hardware from the movable thrust stand/engine hardware to allow thrust measurement. The test cell layout with the YF120-GE-100 engine is shown in Figure 6. Engine exhaust along with cell cooling flow is ducted from the cell via an Exhaust Gas Management System (EGMS) through the exhaust duct where it is cooled by water injection and subsequently discharged to the atmosphere.

The AJDG/PP system is mounted in the inlet duct approximately one engine diameter, about 35 inches, upstream of the AIP rakes and provides a way to set either a steady-state, total-pressure spatial distortion pattern or a planar pressure wave at a specified frequency at the inlet of a turbine engine. For a complete description of the AJDG including its development history see Overall, 1976.

The system operates by injecting a specified volume of secondary air in counter flow to the primary airflow through a series of nozzles arrayed around the inlet duct. Figure 7 illustrates in detail the inlet duct stack-up and gives the dimensions of the AJDG duct

relative to the AIP. Figure 8 shows the configuration and location of the AJDG relative to the engine inlet. By controlling which nozzles inject air, a wide range of distortion patterns can be generated.

The planar pulse system consists of 56 chain-driven, rotating valves in series with the spatial distortion valves. By simultaneously operating the planar pulse valves a planar-wave from 5 to 15 Hz can be generated with the amplitude dependent upon inlet pressure. The air supply conditioning system provides pressure and temperature control of the secondary air for the AJDG. The secondary air is heated or cooled, from -65° to 350° F., as required to match the primary airflow and then throttled to the required pressure for delivery to the supply manifold. The conditioned air is directed from the supply manifold to the desired spatial location using a set of 56 metering valves, tubing and drilled struts. The struts are designed to minimize primary airflow disturbance. Turbulence levels on the order of 2 percent, normalized by face average pressure, at frequencies of 5 to 125 Hz have been reported during airjet operation (McIlveen, 1979). The metering valves regulate the flow rate through the struts to provide the required decrement of pressure at the appropriate location. The system is shown schematically in Figure 9, and a sketch of the AJDG struts and nozzle layout is shown in Figure 10.

The airjet valves are individually controlled by a Modcomp digital computer. A functional schematic is presented in Figure 11. Engine inlet pressure is determined from total-pressure measurements at the AIP (40 transducers). These pressures are transposed to equivalent locations at the plane of the jets and normalized by face average total pressure. The command to each valve is determined by the logic program as shown in Figure 12. A fast vent system is also incorporated to relieve the manifold pressure, thereby eliminating the distortion in the event of an engine surge.

2.3 Instrumentation

A full complement of facility instrumentation including inlet pressures and temperatures, cell pressures and temperatures, fuel flow, and primary and secondary (cell cooling) air flow measurements were used to allow for the safe operation of the facility and test article, and to thoroughly document all test conditions. The engine was extensively instrumented with health monitoring and development instrumentation to accurately characterize all engine parameters of interest. Due to security and classification restrictions specific engine instrumentation and characteristics will not be discussed herein.

The inlet duct was instrumented with eight rakes each containing five probes at the AIP in keeping with SAE ARP 1420 convention. The rakes designated as A, D, G, K, N, R, T, and Y were spaced radially around the circumference of the inlet duct at angles of 14, 57, 99, 141, 184, 226, 268 and 332 degrees looking upstream. Each probe location was designated 1 through 5 from the hub (innermost) to the tip (outermost). Specifically, the rake-probes included fast-response thermocouples, Kulite® type high-frequency response pressure transducers and individual Taber pressure transducers located less than three feet from the rake exit. The probes on each rake are located at the centroids of equal annular areas across the inlet duct diameter, thereby exposing each probe to an equivalent flow area and maintaining the SAE ARP 1420 convention. The inlet duct also contained eight wall-static pressure taps at the AIP. Figure 13 illustrates the rake angular locations and the probe radial location. Total-pressures were recorded in the steady-state using a scani-valve system and transiently using the individual Taber transducers. The high-response pressure (Kulite) and thermocouple data were recorded on analog magnetic tape.

All instrumentation systems were calibrated prior to the test using calibration procedures and standards traceable to the National Institute of Standards and Technology (NIST). These standards are maintained by the AEDC Air Force Type 2c Precision

Measurement Equipment Laboratory (PMEL) in compliance with Department of Defense (DoD) Technical Orders 00-20-14, 1982 and 33K-1-100, 1985.

Measurement uncertainties, for steady-state data, were determined using AEDC-TR-73-5, "Handbook - Uncertainty in Gas Turbine Measurement" (Abernethy and Thompson, 1973). Transient and dynamic uncertainties were not determined.

2.4 Transducer Response

The transient data from the Taber pressure transducers were used for the analysis in this thesis. The Taber transducers provide good frequency response to about 300 Hz with little attenuation below 100 Hz. Research has shown that for comparable line lengths of less than four feet, tube diameters on the order of 0.060", and frequencies from five to fifteen Hertz the magnitude ratio and phase lag have been calculated at about one dB and ten degrees respectively (Whitmore, et. al., 1990). Bergh and Tijdeman, 1965, also shows that for sinusoidal input frequencies of less than 50 Hertz with comparable line lengths and tube diameters non-linearity in the response (output) is virtually non-existent. These data indicate that the system response as-tested was sufficient to validate the results presented herein. Additionally, the data were low-pass filtered at 100 Hz essentially band-width limiting the individual transducer pressure data and eliminating the possibility of Aliasing. The phenomenon of Aliasing is discussed in detail in section 3.6.

2.5 Test Objectives

The test data for this thesis were obtained during test period 13 conducted on 13 May 1989. The objectives for this particular test were: 1. Determining engine dynamic distortion limits using the AJDG/PP system and 2. Engine performance with a conic nozzle. Only those aspects of the AJDG performance relative to the stated objectives of

this thesis are reported herein. The response and performance of the particular engine under test are beyond the scope of this thesis and are not reported.

The facility provided conditions of inlet pressure (P1) = 5.85 psia, cell pressure (P0) = 3.46 psia and inlet temperature (T1) = -2°F corresponded to a flight condition of 35,000 ft at Mach 0.9 Standard Day.

2.6 Test Procedure

Once the flight condition was set and the facility stabilized, the engine was accelerated to 88% corrected compressor speed (PCN2R). The AJDG control was set to a planar pulse frequency of 5 Hertz with the supply manifold (Pman) pressurized to 240 psia to provide a wave amplitude of 1.46 psia peak-to-peak (25%). At this point steady-state and transient data points were taken to document set conditions such as inlet temperature, manifold pressure, facility (plant) settings and engine operating condition. Next, a 200 sample-per-second transient data point was started. Two transient points, numbers 65 @ 5 Hz and 179 @ 15 Hz, were evaluated post test. During the transient data acquisition process the electronic engine control was manipulated to reduce (close) an engine flow path area (A16). This has the net effect of raising the compressor operating line toward the unstable (surge) limit at a constant speed. If the flow area is sufficiently reduced the compressor will stall until the blockage is reduced or the operating line is lowered below the surge limit by some other means. A16 was, in fact, reduced until an engine stall occurred. At this point the airjet manifold was vented, A16 was returned to nominal to relieve the stall condition and the engine recovered to stable operation. Then, the transient data acquisition was stopped and the test program continued as planned.

The 15 Hz planar pulse procedure was similar except the compressor speed was 92% PCN2R and facility provided auxiliary air (inbleed) was used to back pressure the compressor and raise the operating line. This inbleed air flow (WIB) reached 10 pounds

per second when the engine stalled. Again, the airjet manifold was vented, the inbleed airflow was stopped, and the engine recovered normally to stable operation.

These are but two of many procedures used to determine a compressor's stable operating limit. Typically, the nominal, no-distortion stall line is determined first. Subsequently, various mechanisms, such as screens or as in the case of this thesis an airjet are employed to distort the inlet flow and then the distorted stall line is determined as above. The difference between the nominal and distorted stall lines defines the engine's sensitivity to inlet distortion. However, a well-developed consensus method of analyzing engine response to planar wave distortion does not exist (SAE IRD, 1990). A particular engine's response to planar wave distortion depends on many variables including wave frequency and amplitude, control system frequency response and compressor rotating speed and must be determined using analytical methods in combination with a well designed, comprehensive test program.

Additionally, the airframe developer, through wind tunnel tests, determines the pressure distortion patterns that a particular aircraft inlet may generate. This is done for a range of Mach numbers, angles of attack, sideslip angles and airflows. The engine manufacturer and the airframe manufacturer then jointly determine "worst case" distortion patterns in terms of engine compressor stability. Through the use of complex screens these patterns are then reproduced during an engine test in a ground test facility such as ASTF. In this way, installation effects can be determined and solutions applied to inlet/engine compatibility problems.

3 DATA ANALYSIS

3.1 Overview

The post-test planar-wave analysis was carried out in two steps. First the distortion analysis was accomplished to characterize the spatial distortion in terms of the descriptors found in SAE ARP 1420 and described in detail below. Additionally, the wave forms were analyzed for spectral content using a Fast Fourier Transform (FFT) technique found in the Microsoft® Excel software package. The power spectral density (PSD) of the wave was also calculated in Excel using equations discussed in Press et. al. 1986.

3.2 SAE 1420 Distortion Analysis Details

SAE ARP 1420 and SAE AIR 1419 provide guidelines for evaluating the quality of the air being delivered to the inlet of a turbine engine. These standards have been developed by experts in industry, government and academia to provide a common methodology for evaluating the severity of spatial distortion. As mentioned in section 2.6, a consensus method for dealing with time-varying distortion has not been developed. Distortion, whether time-varying, spatial, or a combination of both, if too severe, can cause an engine compressor instability known as stall (or surge) to occur.

Spatial distortion is described in circumferential and radial terms. Circumferential distortion is described in terms of extent, intensity and multiple-per-revolution elements on a ring-by-ring basis. That is, each ring formed by the instrumentation probes is evaluated separately and the results are reported on that basis.

3.3 Circumferential Descriptors

The circumferential distortion descriptors as defined in SAE publications AIR 1419 and ARP 1420 are given as follows:

Extent ≡ "The circumferential distortion extent element (θ^-) for each ring is the angular region, in degrees, in which the pressure is below ring average pressure."

Mathematically the extent is expressed as:

$$(\theta^-)_i = \theta_{2_i} - \theta_{1_i}$$

Theta minus, $(\theta^-)_i$, is defined by the intersection between the ring average pressure (PAV) and the linear interpolation which subtends the low-pressure region in the ring. The extent is used to indicate what portion of the compressor face is affected by circumferential distortion. If large areas of the compressor face are influenced, or if the intensity is extreme compressor instabilities may result. However, each engine's sensitivity to distorted inflow conditions must be evaluated separately. Figure 14 provides a graphical depiction of how the extent is determined.

Intensity ≡ "The circumferential distortion intensity element (DPC/P) describes the magnitude of the pressure defect for each ring."

Mathematically the circumferential intensity is given by:

$$\left(\frac{DPC}{P}\right)_i = \frac{(PAV)_i - (PAVLOW)_i}{(PAV)_i}$$

where

$$(PAV)_i = \frac{1}{360}\int_0^{360} P(\theta)_i d\theta = \text{Ring Average Pressure.}$$

$P(\theta)_i$ is a function resulting from a linear fit, per the SAE standard, between the data points. *PAVLOW* is defined on the basis of the extent previously given (See Figure 14). It is expressed mathematically as follows:

$$(PAVLOW)_i = \frac{1}{\theta_i^-} \int_{\theta_i^-} P(\theta)_i d\theta$$

The preceding definitions are given for a one-per-revolution distortion pattern, that is, one pressure defect per 360°. For distortion patterns with more than one low pressure region per 360° ring, a Multiple-per-Revolution (MPR) descriptor is employed.

> Multiple-per-Revolution ≡ "The circumferential distortion multiple-per-revolution element (MPR) describes the number of low-pressure regions for each ring."

The intensity and extent are calculated as above for each low pressure region in the ring with the equations written for the k-th low-pressure region for Q low-pressure regions per ring.

3.4 Radial Descriptor

Radial distortion is also defined on a ring-by-ring basis per SAE ARP 1420 as follows:

> Radial distortion element ≡ "The radial distortion intensity element (DPR/P) describes the difference between the ring average pressure and the face average pressure for each ring. Positive values reflect an average ring pressure that is below the face average pressure.

Mathematically the radial distortion element is defined as follow:

$$\left(\frac{DPR}{P}\right)_i = \frac{(PFAV) - (PAV)_i}{(PFAV)}$$

Where $PFAV$ is the area-weighted face-average pressure. For rings at the centers of equal annular areas:

$$(PFAV) = \frac{1}{N} \sum_{i=1}^{N} (PAV)_i$$

Figure 15 illustrates the definition of radial intensity graphically.

These equations were programmed in the Microsoft ® Quick BASIC version 4.5 computing language along with data reading and output routines to provide the results for this thesis. The programming and analysis was carried out using an *i*486DX2-50 based desk top personal computer.

3.5 PSD Methodology

The PSD analysis was accomplished using a power-of-two Fast Fourier Transform algorithm available in the Microsoft® Excel spreadsheet software package. The Excel FFT was chosen for several reasons. Chief among them was its fidelity in characterizing a pure-tone wave-form. For example, PSD's were calculated for cosine waves of 5 and 15 Hertz and unity amplitude. The Excel results were consistent with expected results, produced no spurious peaks and produced a sharp definition of the amplitude/frequency curve. Additionally, as the FFT is a built-in function in the Excel program it is extremely easy to use. One only has to "highlight" the appropriate data and specify a location for the results to be displayed. The Fourier coefficients can then be manipulated as any other cells in the spreadsheet.

3.6 Fourier Analysis Details

The Fourier Transform allows for the transformation of periodic functions from the time domain, $x(t)$ to the frequency domain, $X(f)$ through the use of a series sum of sinusoids of appropriate amplitudes at known frequencies (Elliott and Rao, 1982). "For many purposes it is useful to think of $x(t)$ and $X(f)$ as being two different representations of the same function. One goes back and forth between these two representations by means of the Fourier transform equations" (Press, et al., 1986).

The Fourier transform $X(f)$ is given by:

$$X(f) = \int_{-\infty}^{\infty} x(t) e^{-i2\pi ft} dt$$

where $x(t)$ is a periodic function, f is the frequency and t is time. The inverse transform is given as :

$$x(t) = \int_{-\infty}^{\infty} X(f) e^{i2\pi ft} df$$

The Discrete Fourier Transform (DFT) is evaluated in practical applications as its input is a sequence of numbers rather than a continuous function of time $x(t)$. The sequence of numbers usually results from the periodic sampling of a continuous signal $x(t)$ at an interval of T seconds (Elliot and Rao, 1982). The DFT is derived from a time function $x(t)$ using N samples taken at times $t = 0, T, 2T, \ldots, (N-1)T$, where T is the sampling interval. If $a \leftarrow b$ is used to mean a is approximated by b, the relationship between continuous and discrete-time values can be expressed as:

$$t \leftarrow nT, \quad dt \leftarrow T, \quad x(t) = x(n) \ \ at \ \ t = nT$$

If the continuous function $x(t)$ is replaced by discrete values, the integration is replaced by a summation and the approximations from the above relationships are substituted into the integral equation above, the following results:

$$\int_{-\infty}^{\infty} x(t) e^{-i2\pi ft} dt \leftarrow \frac{1}{NT} \sum_{n=0}^{N-1} x(n) e^{\frac{-i2\pi knT}{NT}} T$$

The summation represents an approximation of the Fourier series. The derivation uses the N data points $x(0), x(1), \ldots, x(N-1)$ which allows only for the solution of N unknown coefficients. Therefore restricting k to be one of the finite integers $0, 1, 2, \ldots, N-1$ gives:

$$X(k) = \frac{1}{N} \sum_{n=0}^{N-1} x(n) e^{\frac{-i2\pi kn}{N}}, \quad \text{k} = 0, 1, 2, \ldots, \text{N-1}$$

Again, the inverse transform is given by:

$$x(n) = \sum_{k=0}^{N-1} X(k) e^{\frac{i2\pi kn}{N}}$$

The transform coefficient number k identifies the frequency component given by:

$$f_k = \frac{k}{N} f_s$$

where f_s is the sampling frequency of the signal.

The power spectrum or PSD of the transform indicates what frequencies are represented in the signal being evaluated and the relative power or energy present in each frequency. The periodogram estimate of the power spectrum at $N/2+1$ frequencies is given by:

$$P(0) = P(f_0) = \frac{1}{N^2} |X_0|^2$$

$$P(f_k) = \frac{1}{N^2} \left[|X_k|^2 + |X_{N-k}|^2 \right] \quad for\ k = 1,2,\ldots,\left(\frac{N}{2} - 1\right)$$

$$P(f_c) = P(f_{N/2}) = \frac{1}{N^2} \left| X_{N/2} \right|^2$$

where f_k is defined only for zero and positive frequencies:

$$f_k \equiv \frac{k}{NT} = 2 f_c \frac{k}{N} \quad \text{for } k = 0,1,\ldots,\frac{N}{2}$$

Once the Fourier coefficients were calculated Excel was again used to calculate the PSD using the above equations for the periodogram estimator. The spreadsheet is well suited for manipulating a large volume of discrete values and was very effective at computing the PSD values presented herein.

Another factor to consider when conducting the Fourier analysis concerns the Nyquist sampling theorem. For any sampling interval T, there is also a special frequency f_c, called the Nyquist critical frequency, given by:

$$f_c \equiv \frac{1}{2T}$$

To quote, "The Nyquist critical frequency is important for two related, but distinct, reasons. First, if a continuous function *x(t)*, sampled at interval *T*, is band-width limited to frequencies less than f_c then the function is completely determined by its samples. However, if the function is not band-width limited all of the power spectral density which is outside the range $-f_c < f < f_c$ is spuriously moved into that range as a result of discrete sampling" (Press, et al., 1986). This phenomenon is known as Aliasing. To prevent Aliasing the wave form must be either bandwidth limited or sampled at a rate greater than twice the highest frequency component present. The data in this paper, as explained in the instrumentation section, have been low-pass filtered at 100 Hz which effectively bandwidth limits the data. Additionally, the sampling frequency of 200 Hz is well above any expected frequency components present in the wave which are on the order of five to fifteen Hertz. Therefore the possibility of aliased power components in the data is minimized.

3.7 PSD Data Presentation

Since the DFT operates on discretely sampled values the results are given at discrete frequencies. The f_k's on the abscissa are actually representative of frequency "bins" which extend from halfway between the preceding discrete frequency to halfway between the next one (Press, et al., 1986). The $P(f_k)$ is an average $P(f)$ over a narrow window function centered on its f_k. The window function *W*, as a function of *s*, the frequency offset in bins, is given by:

$$W(s) = \frac{1}{N^2}\left[\frac{\sin(\pi s)}{\sin(\pi s/N)}\right]^2$$

W(s) has oscillatory lobes but falls off as $W(s) \approx (\pi s)^{-2}$. This fall-off is not very rapid and results in significant "leakage" (that is the technical term) from one frequency bin to another (Press, et al., 1986). If the time function *x(t)* is a pure sine wave of a frequency equal to one of the f_k's there is no leakage. However, if the frequency is between the f_k's there can be significant leakage to adjacent f_k's.

One solution to the problem of leakage is a process called data windowing. The purpose of data windowing is to modify *W(s)*, which expresses the relation between the spectral estimate, $P(f_k)$, at a discrete frequency and the actual underlying $P(f)$ at nearby frequencies (Press, et al., 1986). The discrete values in time *x(n)*'s are multiplied by a window function that changes gradually from zero to one and then back to zero as *n* ranges from *0* to *N-1* during the transformation process. For example, the "Parzen" window is defined as (Press, et al., 1986):

$$w_j \equiv 1 - \left| \frac{j - \frac{1}{2}(N-1)}{\frac{1}{2}(N+1)} \right|$$

The principle tradeoff between the various window functions is in making the central peak as narrow as possible versus making the tails of the distribution fall off as rapidly as possible. The PSD results reported herein are based on a square window function (no windowing) and are explained in detail in section 4.6

4 RESULTS AND DISCUSSION

4.1 Distortion Analysis Overview

Transient data point numbers 65 and 179 were chosen for analysis for two important but distinct reasons. First, they represent "real world" data. That is, they were recorded during an actual engine distortion sensitivity test immediately prior to an induced stall event. Data during the stall were not available, however, this lack does not affect the analysis conducted herein. Therefore, the results presented in this thesis are representative of the type of performance attained by the AJDG during planar pulse distortion testing. Secondly, the data chosen were readily available and were the only set formatted for analysis on a desktop PC. Albeit not necessarily the most important reason for choosing a particular data set, availability is a prime consideration in the present circumstances.

To obtain a representative "picture" of the distortion level, six discrete points on the wave form were analyzed. Data were chosen before the peak amplitude, at the peak amplitude and after peak amplitude. Similarly, values were chosen before minimum amplitude, at minimum amplitude and after minimum amplitude. The same method of selection was used for both the 5 and 15 Hz waves. The individual points were chosen arbitrarily. Once the individual data were identified each time-slice was evaluated separately using the SAE ARP 1420 methods previously discussed. The end result is that at each discrete time slice a representative picture of the overall distortion level is provided. Presumably the information obtained at the extrema and during the transients will adequately characterize the wave form in terms of the distortion level present.

4.2 Probe Substitution

Before the final analysis can be completed spurious data channels must be identified and appropriate substitutions made. Several techniques exist for the identification and

substitution of bad probes and are discussed in detail in SAE AIR 1419. In the case of the data presented herein the erroneous channels were identified during post test analysis by comparison to adjacent probe values. Only obviously bad channels (variations of 40% in total pressure) were flagged for substitution. The probable cause of the bad channels were leaks in the pneumatic transmission lines which allowed the transducer to "see" cell pressure resulting in an obviously errant signal. These pneumatic lines were pressure checked and the leaks repaired before the next test period.

Once the bad probes were identified their output was replaced by the average of the two circumferentially adjacent probes. This method was used for one primary reason: the direct-connect configuration of testing results in a relatively small amount (≈2%) of radial distortion occurring in the blade tip region of the inlet duct. This is due to the boundary layer that exists along the wall of the inlet duct. The goal of the AJDG/PP test was to add as little spatial distortion as possible. Since no mechanism was in place to intentionally generate circumferential components, such as a screen, and since the radial component is inherently present, adjacent circumferential probes were used. The intent was to maintain the ring-to-ring integrity of the data. This method of substitution is particularly appropriate for probes on the extremities of the rake. Table 1[2] on page 46 summarizes the probe substitutions made before the distortion and Fourier analysis was carried out. The rake and probe nomenclature is as defined in Figure 13.

4.3 Data Presentation Overview

The results are presented in tabular and graphical form in the Appendix and are organized as follows: Figure 16 (a and b) presents time-trace data and face-average total-pressure for the 5 and 15 Hertz waves respectively with the individual points selected for

---

[2] All Tables are presented in the Appendix.

analysis annotated. The 5 hertz (data point 65) distortion analysis results are presented first in Tables 2 through 13 and Figures 17 through 34. The individual time slices are evaluated sequentially and are identified as "pre-peak", "peak", "post-peak" and so on through "post-valley". The first table in each sequence, beginning with Table 2 on page 47, presents the 40 individual probe pressures used in the SAE 1420 analysis. They are identified by rake from hub to tip. The second table in the sequence presents the results of the SAE 1420 analysis for that time-slice. The results are shown on a ring-by-ring basis per the SAE convention. The ring average (PAV) and the ring average low (PAVLOW) pressures are given, followed by the SAE distortion indices for circumferential intensity (DPC/P), radial intensity (DPR/P) and then the circumferential extents, high and low, (θ, θ^-). Also shown for comparison is the face average pressure (PFAV). Graphical representations of the results are then shown.

The first figure in each sequence, beginning with Figure 17, shows the ring average pressure (PAV), ring average low pressure (PAVLOW) and the face average pressure (PFAV) from hub to tip as calculated from the equations in sections 3.3 and 3.4. The second figure in each sequence shows the circumferential and radial distortion indices for each ring from hub to tip. The side-by-side bar-graph format shows the ring-to-ring variations and also the circumferential and radial intensities relative to each other. The third figure in the sequence shows the high and low circumferential extent for each ring. The horizontal bar-graph format shows the high and low extents summing to 360 degrees as expected. Also, the graph illustrates the relative magnitudes of the extents. The results for data point 179 (15 Hz), beginning with Table 14 on page 59, and Figures 35 through 52 are organized and presented identically to the data point 65 results. Figures 53 and 54 present average radial and circumferential distortion indices versus ring number for comparison purposes. Figures 55 and 56 show the PSD's of the 5 and 15 Hz cosine wave

4.4 5 Hertz Wave Distortion Results

Total pressure distortion in the 5 Hertz wave is typical of levels present during direct-connect type tests. As mentioned above, a typical "clean inlet" distortion profile may have about 2% radial distortion primarily in the tip region due to viscous effects at the inlet duct wall. Figure 17 shows the individual ring average pressure (PAV), ring average low pressure (PAVLOW), and face average pressure (PFAV), from the equations in sections 3.3 and 3.4 versus the ring number. As expected, the pressure decreases from the hub to the tip region with a corresponding increase in the radial distortion index (DPR/P). This is due, as stated earlier, to the viscous effects associated with the boundary layer at the duct wall.

The highest radial distortion level calculated was 2.09% at the "post-peak" of the wave. The tabular results for this time-slice of the wave are presented in Table 7 with the graphical representation shown in Figure 23. Again, the figure shows the characteristic "rolling off" of the pressure in the tip region at the duct wall. It is interesting to note that at the peak of the wave the AJDG is not operating. The AJDG is used to decrement the pressure, that is create a pressure defect, since its discharge is contrary to the primary flow direction. The levels of radial distortion during the "valley" of the wave, when the airjet is operating, are generally lower than the "peak" portions of the wave (1.9% vs. 2.1%). It should be noted that steady-state distortion levels when the AJDG is not operating are on the order of typical "clean" inlet distortion levels (1 to 2 percent tip radial).

One theory advanced to explain this apparent discrepancy concerns the "washing out" of the tip radial distortion as the airjet is operated. This can be inferred by considering the effect of the airjet on the boundary layer. As the airjet flow and the boundary layer interact, local turbulent mixing of the flow occurs. The increased momentum present in the turbulent boundary shows up as increased total-pressure at the AIP rakes. This theory has not been substantiated by detailed tests or analysis. Also,

boundary layer interact, local turbulent mixing of the flow occurs. The increased momentum present in the turbulent boundary shows up as increased total-pressure at the AIP rakes. This theory has not been substantiated by detailed tests or analysis. Also, AJDG limitations have been reported in setting "higher" steady-state tip radial distortion patterns (Amundson and Holm, 1989). The speculation in Amundson and Holm concerns the location of the airjet discharge orifices relative to the duct periphery. Further investigation and analysis is required to answer these questions.

The circumferential distortion levels are, as expected, slightly lower in magnitude than the radial levels. Typically, a "clean" inlet will have slightly less than one percent circumferential distortion. The highest circumferential component is shown in Table 3 and Figure 17. The level is 1.38% in ring 2 at the point prior to the wave "peak". The circumferential extents for all other points are virtually even for all rings at all time slices, and are in excellent agreement with clean inlet results. No discernible trends were expected in the circumferential results and none were noted.

The multiple-per-rev parameter (MPR) was computed to be one for all cases. This is purely a result of the algorithm used to calculate the various distortion indices. The algorithm is written to default to an MPR value of one in the event multiple low pressure regions are not found. The extent (θ^-) is calculated based on the equations in section 3.3. In the event of no discernible or very small (in magnitude) circumferential defects, the extent will turn out to be very close to 180 degrees with the corresponding circumferential intensities being very low. The circumferential intensities (DPC/P) can then be used to evaluate the circumferential results. In those cases where the extent is not 180°, e.g., the ring 2 "pre-peak" point, the magnitude is very small (1.38%). On a practical level, it can be inferred from the data that no appreciable circumferential distortion component existed during the 5 Hz operation of the AJDG at a flight condition of 35,000 feet and Mach 0.9.

4.5 15 Hertz Wave Distortion Results

The results for the 15 Hertz wave were similar in magnitude to the 5 Hertz wave results. The same characteristics, from hub to tip, are evident in the plots of total pressure versus ring number. The maximum radial distortion level of 2.51% occurs at the "pre-valley" point in the tip region. Table 21 and Figure 44 show the results in tabular and graphical form respectively. Contrary to the 5 Hz results the highest radial distortion level occurs when the airjet is operating. Although, in general, the radial distortion levels are lower during airjet operation and again comparable to levels present during "clean" inlet tests.

The maximum circumferential distortion level of 3.18 % is found at the "pre-peak" point in ring three. Again, the calculation routine defaulted to a one-per-rev MPR, as a distinct low level pressure region was not detected. In general, the circumferential levels are higher for the 15 Hz wave. However, the distortion is very low and comparable to direct-connect type engine tests.

For comparison purposes Table 26 and Figures 53 and 54 present average values for the circumferential and radial distortion indices for both waves. These values were calculated by averaging the distortion indices for each ring at each time slice. Figure 53 presents the average radial distortion level for both the 5 and 15 Hz wave. Figure 54 presents the circumferential indices for both waves. Evident, are the comparable distortion levels between the 5 and 15 Hz wave and the generally low distortion levels overall.

4.6 Distortion Results Summary

The SAE ARP 1420 analysis results are summarized as follows:

1. The maximum radial distortion level in the 5 Hz wave was 2.09 % at the wave "post-peak" in the tip region.

2. The maximum circumferential distortion level in the 5 Hz wave was 1.38 % at the "pre-peak" point in ring 2.

3. The MPR and DPC/P indices, when evaluated together, imply that there are no distinct circumferential low pressure regions.

4. The overall spatial distortion content, in the 5 Hertz wave, is consistent with levels present in "clean" inlet direct-connect type engine tests.

5. The maximum radial distortion level in the 15 Hz wave was 2.51 % at the wave "pre-valley" in the tip region.

6. The maximum circumferential distortion level in the 15 Hz wave was 3.18 % at the "pre-peak" point in ring 3.

7. The overall spatial distortion content, in the 15 Hertz wave, is consistent with levels present in "clean" inlet direct-connect type engine tests.

8. Generally, the radial distortion levels are comparable, on average, for the 5 Hz and 15 Hz waves.

9. The overall circumferential distortion levels are greater, on average, for the 5 Hertz wave. However, the magnitudes are low enough ($\approx$ 1% to 2%) for both waves to be considered inconsequential.

4.7 DFT Results Overview

The intent of the Fourier analysis was to determine whether or not the AJDG produced a discrete or very nearly discrete planar wave. The magnitude of the PSD is not the prime consideration. The frequency, however, at which the power is concentrated is of primary importance.

As stated earlier, the data points used in this analysis were recorded immediately prior to an engine stall event. A three second span of data, recorded at a sampling rate of 200 samples per second, resulted in 600 samples available for analysis. Since only 600

time slices were available and the DFT algorithm required an integer power-of-two number of values, a total of 2^9 or 512 discrete pressure values were used in an attempt to resolve the PSD as finely as possible. Sample lengths of 2^7 and 2^8 points were evaluated but the frequency resolution was inadequate. It is recognized that the number of samples is not very large for conducting Fourier analysis and a larger number of samples is desirable. However, the 512 sample Fourier transform represents approximately 13 cycles of the 5 Hz wave and 38 cycles of the 15 Hz wave. It is presumed that the number of cycles completed during the sampling duration are adequate for use in characterizing the wave forms of interest. It should be noted however, that the PSD's reported herein may not be accurate representations of long periods of AJDG operation. For example, facility perturbations or engine instabilities may adversely affect the air jet's operation. Such disturbances are not captured in the data reported in this thesis. Though, it is fair to say that the AJDG is generally used for a relatively short duration during a particular test sequence and any large disturbances would likely result in repeating the experiment.

Additionally, an increase in the number of samples does not necessarily increase the accuracy of the PSD, however, it does increase the fidelity of the results. The information contained in a larger number of samples simply increases the frequency resolution. That is, the PSD is calculated for a greater number of discrete frequencies within the sampled frequency range. The frequency band-width of a transformed point is inversely related to the number of samples transformed. The frequency resolution of 512 samples taken at a sampling frequency of 200 Hz resulted in a discrete frequency band-width of 0.39 Hz. The magnitude of the PSD, normalized by the number of samples squared (N^2), is related to the wave amplitude through the transform function.

Time domain plots of the average total-pressure $P(t)$ versus time t for both the 5 Hz and 15 Hz waves are shown in Figure 16 (a and b). Additionally, the mean value of the each wave is shown in the aforementioned figures. This mean value was subtracted from

each discrete time slice before the Fourier transform was applied. This was done to eliminate the large, non time-varying (DC) component from the wave. Since the average value of 5.8 psia was larger than the peak-to-peak amplitude of 1.46 psia the PSD would indicate a very high power density at zero hertz and relatively low power density at frequencies greater than zero. The primary interest is, of course, at frequencies greater than zero.

Finally, the decision was made not to window the data per the technique discussed in section 3.7 for the following reason. As described in section 3.5, five and fifteen Hertz cosine wave PSD's were calculated, with no windowing, to evaluate the Excel FFT (Figures 55 and 56). The cosine wave PSD's were sharply defined in the appropriate frequency bins with no oscillatory side lobes or spurious peaks. The test data were then transformed and the PSD's calculated per section 3.6 with a window function equal to unity (no windowing). The PSD's of both the five and fifteen Hertz waves, from the test data, were also clearly concentrated in the appropriate frequency bins. Additionally, there were no side lobes or oscillatory lobes in the adjacent bins. In fact, the peak was sharply defined and very concentrated for both waves. The test data waves appeared to be of a nearly discrete frequency and were well behaved, similar to the cosine wave test cases. Based on these observations, it was determined that the PSD's of the AJDG created waves were sufficient, as calculated with no windowing, to convey the required information.

4.8 5 Hertz Wave Fourier Results

The power of the 5 Hz wave is indeed concentrated in the 5.5 Hertz frequency bin as expected. Evaluation of the waveform shown in figure 16a indicated the AJDG was actually operating at a frequency of 5.4 Hz. Hence the power was concentrated in the 5.5 Hz bin. Figure 57 shows the PSD for each ring. There is no variation in frequency from ring-to-ring. That is, each curve indicates that the power is concentrated in the 5.5 Hz

bin. The magnitude of the tip ring is the lowest indicating the higher distortion and lower energy levels present in the tip region. A harmonic in the 10.9 Hz bin, about twice the fundamental frequency, also is indicated. The amplitude is approximately an order of magnitude less than the fundamental frequency. There are no other higher order harmonics within the frequency band analyzed. Whether the harmonic is physical or a consequence of the data analysis is undetermined. Also, there is no broad-band energy present. The magnitude of the PSD shows very clearly the power is indeed concentrated in the 5.5 Hz bin. Overall, the AJDG/PP system appears to be a credible method of producing a spatially-uniform discrete five Hertz planar wave.

4.9 15 Hertz Wave Fourier Results

The PSD of the 15 Hz wave was concentrated in the 15.6 Hz bin which extends from 15.23 to about 16.02 Hz. Again, evaluation of the frequency of the waveform shown in figure 16b indicates the AJDG was operating at a frequency of 15.4 Hz. Figure 58 presents the 15 Hertz PSD in graphical format. The PSD was sharp and well defined with no oscillatory lobes present. Additionally, each of the five rings was also in the same bin indicating there was no ring-to ring variation. The magnitude of the tip ring was again the lowest indicating the tip radial distortion inherently present in a direct-connect type engine test. As with the 5 Hz wave there appeared to be a first order harmonic at 30.86 Hz., exactly twice the fundamental frequency. Again, it is undetermined if this is a physical phenomenon or a result of the data analysis. The level was two orders of magnitude lower than the fundamental frequency and should not pose any problems. No higher order harmonics were noted. Also, no broad-band spectra are present. The 15 Hz wave, as with the 5 Hz wave, appeared to be a high quality representation of a spatially-uniform discrete planar wave.

5 CONCLUDING REMARKS

5.1 Summary

The AEDC Airjet Distortion Generator was operated in propulsion development test cell C-1 during the development testing of the General Electric YF120 mixed flow turbofan engine. The AJDG was operated in planar pulse mode at discrete frequencies of five and fifteen Hertz. The facility set conditions of P1 = 5.85 psia, P0 = 3.46 psia and T1 = -2° F. corresponded to a flight condition of Mach 0.9 at 35,000 feet Standard Day. The wave amplitude was set at approximately 1.46 psia (25% of P1) at each frequency.

Overall, the AJDG appears capable of providing five and fifteen Hertz discrete or sinusoidal planar waves. Radial distortion levels were comparable to those typically found in direct-connect type engine tests (≈ 2%) with the effects concentrated in the tip region as expected. Circumferential levels were generally low (≈ 1%) with no multiple-per-rev elements present. The operating frequency of the AJDG was shown to be approximately 0.4 hertz higher than the target frequency, 5.4 and 15.4 Hz respectively. The PSD's of the waves indicated the frequencies are concentrated in the appropriate bins and no high-energy harmonics or broad-band spectra appeared to be present.

The AJDG appears to be an effective tool for use during engine ground testing. However, the system must be operated over a greater range of flight conditions to fully evaluate its potential. For example, a comprehensive test matrix including high and low airflow, pressures and temperatures must be established and conducted to completely document the AJDG's performance in the planar pulse mode.

BIBLIOGRAPHY

BIBLIOGRAPHY

Amundson, M. H., Holm, R. G., "Distortion Test Capabilities for Future Fighter Aircraft Engines," AIAA Paper No. 89-2956, AIAA/ASME/SAE/ASEE 25th Joint Propulsion Conference, July 10-12 1989.

Abernethy, R. B., Thompson, J. W., "Handbook - Uncertainty in Gas Turbine Measurements," AEDC-TR-73-5, February 1973

Bergh, H., Tijdeman, H., "Theoretical and Experimental Results for the Dynamic Response of Pressure Measuring Systems," NLR-TR F.238, 1965.

Burcham, F. W., Hughes, D. L., "Analysis of In-Flight Pressure Fluctuations Leading to Engine Compressor Surge in an F-111A Airplane for Mach Numbers to 2.17," AIAA Paper No. 70-624, AIAA 6th Joint Specialist Conference, June 15-19, 1970.

Drewes, R. W., The Air Force and the Great Engine War. National Defense University Press, Washington D. C., 1987

Elliot, D. F., Rao, K. R., Fast Transforms, Algorithms, Analyses, Applications. Academic Press, Orlando, 1982.

MacMiller, C. J., Hagenson, W. R., "Unsteady Inlet Distortion Characteristics with the B-1B," 68th(A) Specialists Meeting of the AGARD Propulsion and Energetics Panel on Engine Response to Distorted Inflow Conditions, September, 8-9, 1986.

McCallum B., "F-16 Inlet Stability Investigation," AIAA Paper No. 89-2465, AIAA/ASME/SAE/ASEE 25th Joint Propulsion Conference, July 10-12, 1989.

McIlveen, M. W., "Further Test Results with the Airjet Distortion Generator System," AIAA Paper No. 79-1185, AIAA/SAE/ASME 15th Joint Propulsion Conference, June 18-20, 1979.

Mitchell, Dr. J. G., "The Aeropropulsion Systems Test Facility," AIAA Paper No. 72-1034, AIAA 7th Aerodynamic Testing Conference, September, 1972.

Overall, W. B., "Evaluation of an Airjet Distortion Generator Used to Produce Steady-State, Total-Pressure Distortion at the Inlet of Turbine Engines," AEDC-TR-76-141, 1976.

Press, W. H., Flannery, B. P., Teukolsky, S. A., Vetterling, W. T., Numerical Recipes - The Art of Scientific Computing. Cambridge University Press, New York, 1986.

SAE S-16 Committee, AIR 1419, "Inlet Total-Pressure Distortion Considerations for Gas Turbine Engines," Society of Automotive Engineers, Inc., May 1983.

SAE S-16 Committee, ARP 1420, "Gas Turbine Engine Inlet Flow Distortion Guidelines," Society of Automotive Engineers, Inc., March 1978.

SAE S-16 Committee, Industry Review Draft, "A Current Assessment of Planar Waves," Society of Automotive Engineers, Inc., February 1990.

Steenken, W. G., "Planar Wave Stability Margin Loss Methodology," AIAA Paper No. 88-3264, AIAA/ASME/SAE/ASEE 24th Joint Propulsion Conference, July 11-13, 1988.

Strum, R. D., Kirk, D. E., First Principles of Discrete Systems and Digital Signal Processing. Addison-Wesley, Reading, Massachusetts, 1988.

Technical Order 00-20-14, Air Force Metrology and Calibration Program, May 1982.

Technical Order 33K-1-100, TMDE Internal Calibration and Repair Technical Order Reference Guide and Work Unit Code Manual, July 1985.

Whitmore, S. A., Lindsey, W. T., Curry R. E., Gilyard, G. B., "Experimental Characterization of the Effects of Pneumatic Tubing on Unsteady Pressure Measurements," NASA Technical Memorandum 4171, March 1990.

APPENDIX

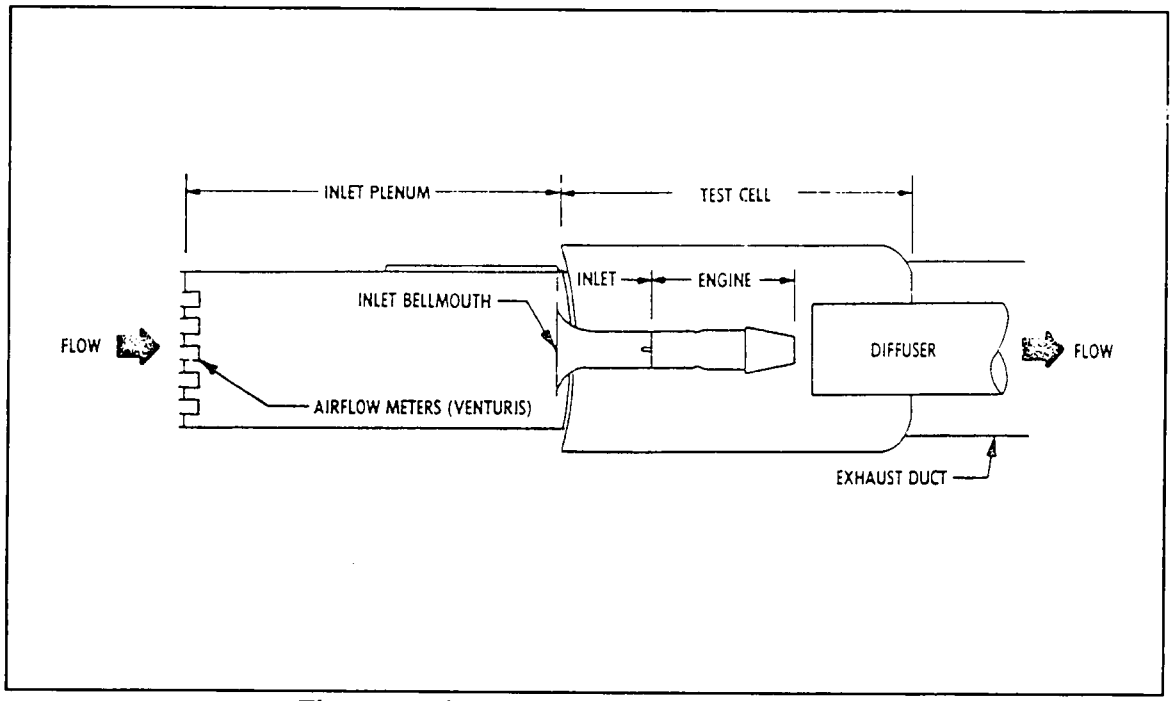


Figure 1, Direct-Connect Test Configuration

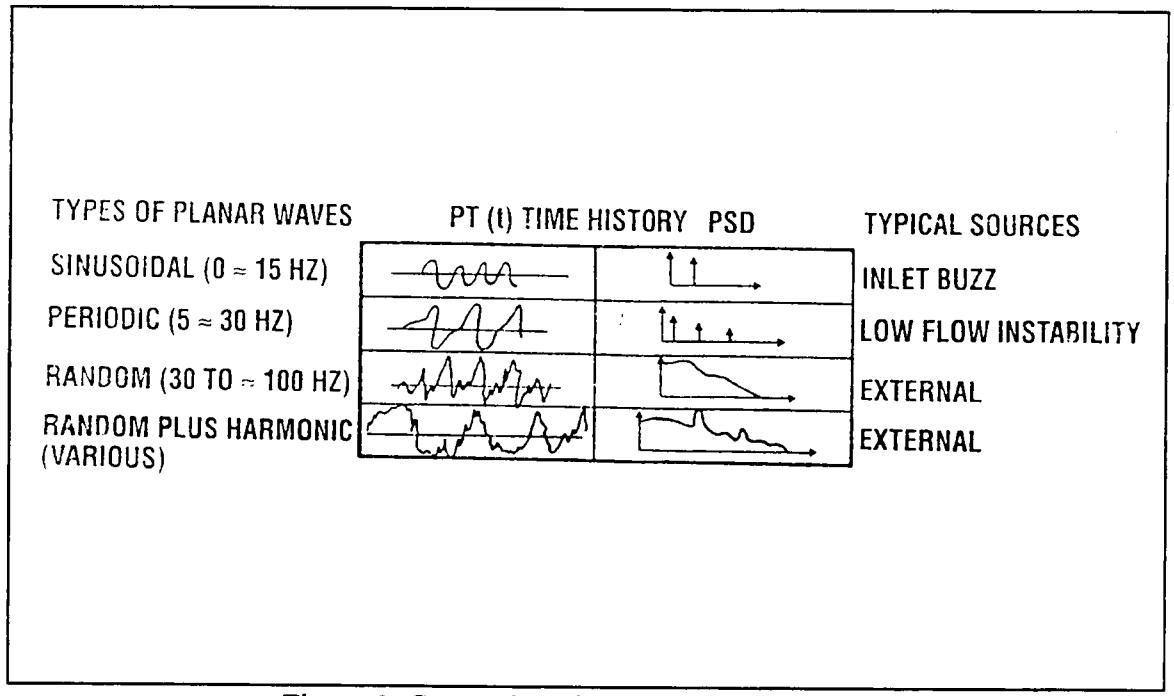


Figure 2, Categories of Planar Wave Distortion
Source(s): SAE S-16 Committee, Industry Review Draft, "A Current Assessment of Planar Waves," Society of Automotive Engineers, Inc., February 1990.

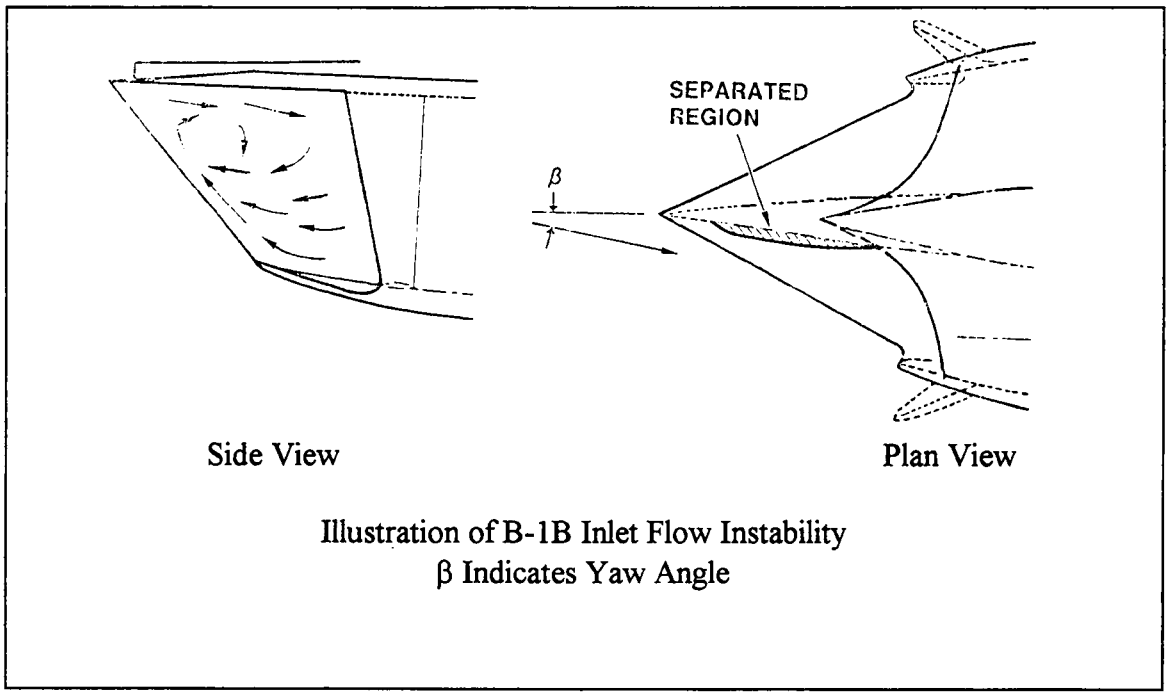


Figure 3, Local Flow Separation on the B-1B Inlet Ramp at Off-Design, low Airflow
Source(s): MacMiller, C. J., Hagenson, W. R., "Unsteady Inlet Distortion Characteristics with the B-1B," 68th(A) Specialists Meeting of the AGARD Propulsion and Energetics Panel on Engine Response to Distorted Inflow Conditions, September 8-9, 1986.

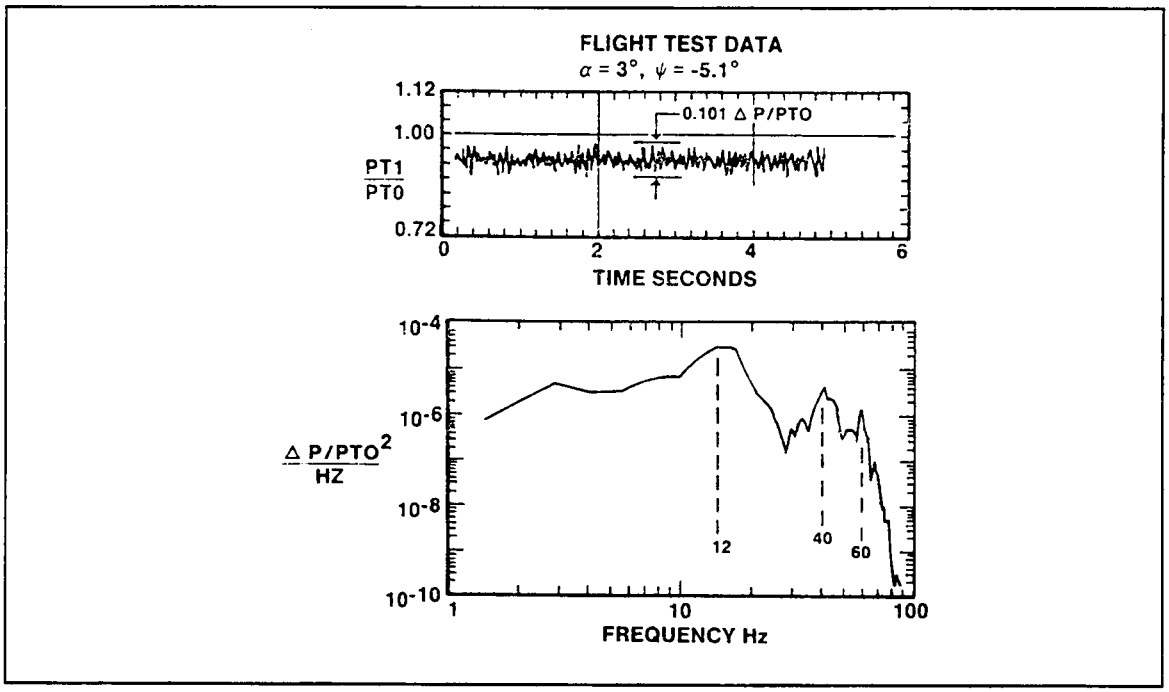


Figure 4, B-1B Inlet Duct Resonance at Mach 0.85
Source(s): MacMiller, C. J., Hagenson, W. R., "Unsteady Inlet Distortion Characteristics with the B-1B," 68th(A) Specialists Meeting of the AGARD Propulsion and Energetics Panel on Engine Response to Distorted Inflow Conditions, September 8-9, 1986.

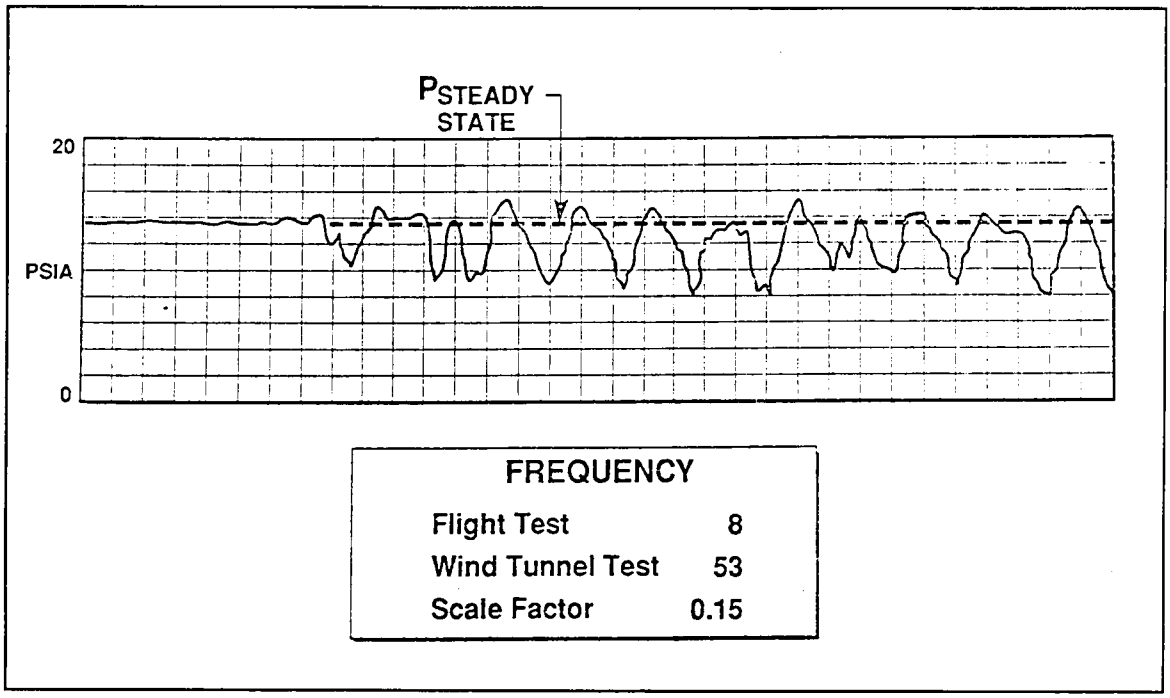


Figure 5, Time-History of F-16 Inlet Instability
Source(s): McCallum, B. N., "F-16 Inlet Instability Investigation," AIAA Paper 89-2465, AIAA/ASME/SAE/ASEE 25th Joint Propulsion Conference, July 10-12, 1989.

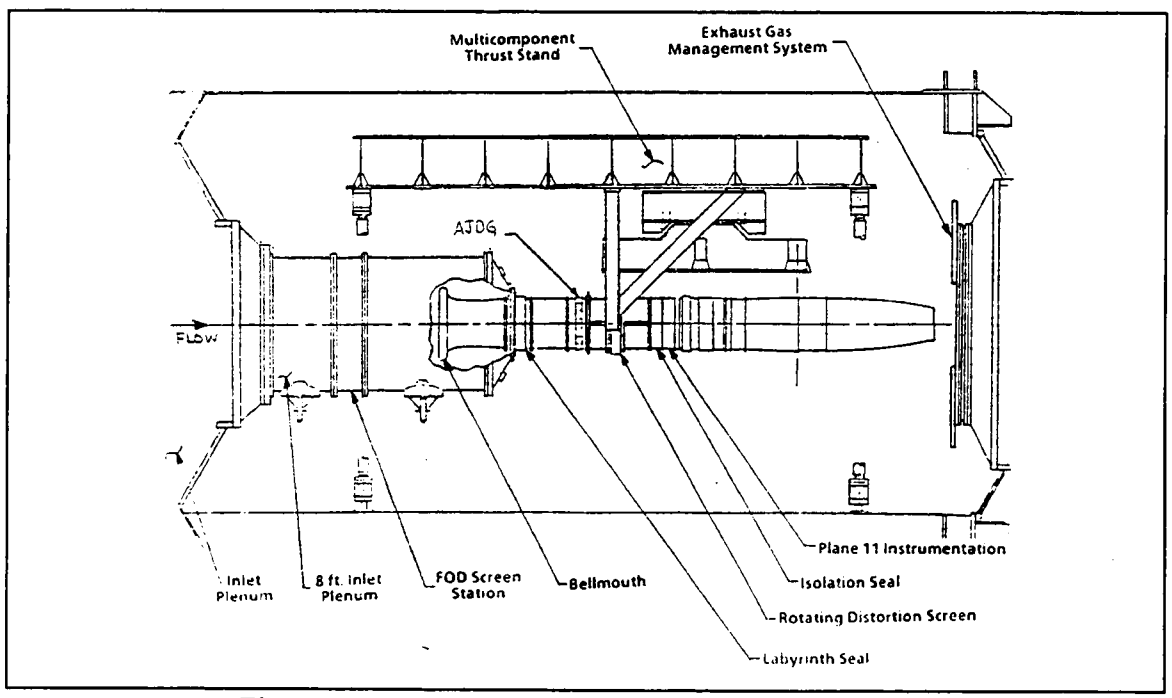


Figure 6, YF120-GE-100 Installation in Test Cell C-1

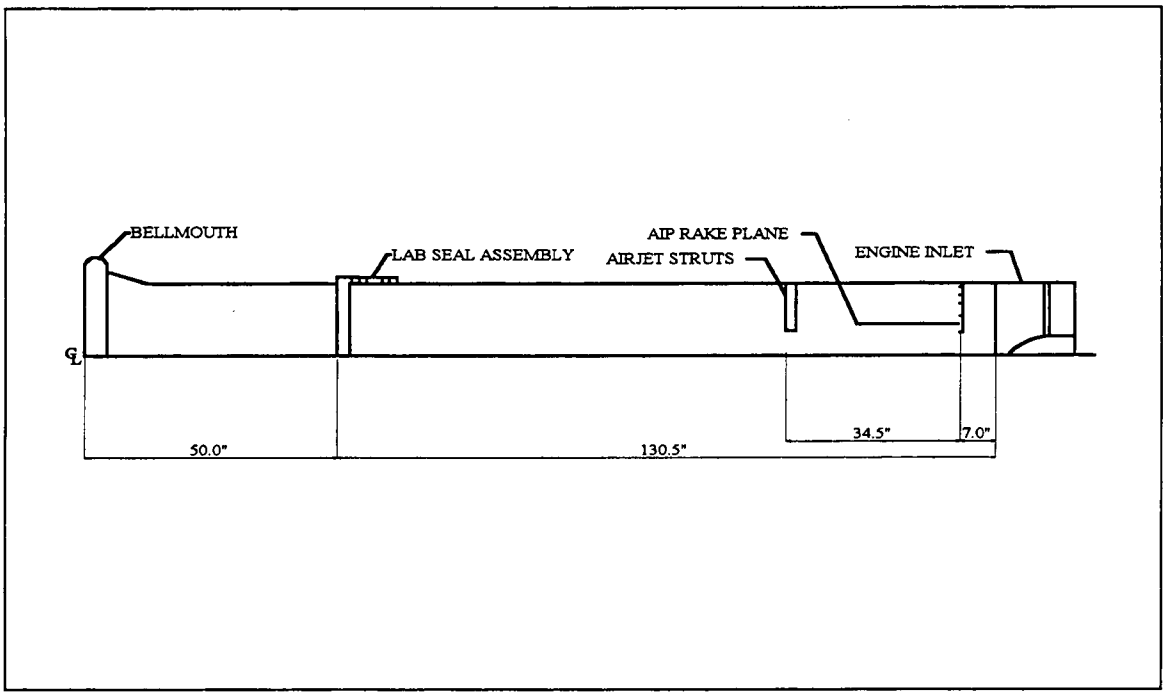


Figure 7, Inlet Duct Configuration Details

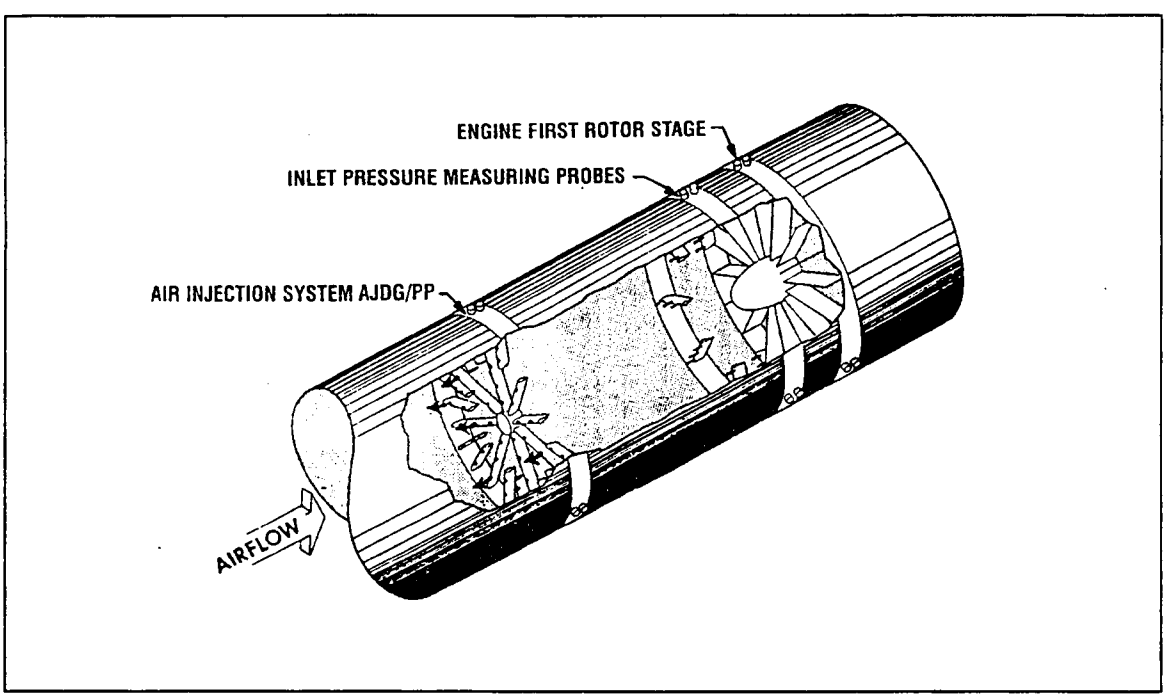


Figure 8, AJDG/PP and Inlet Rake Configuration Relative to the Engine Face

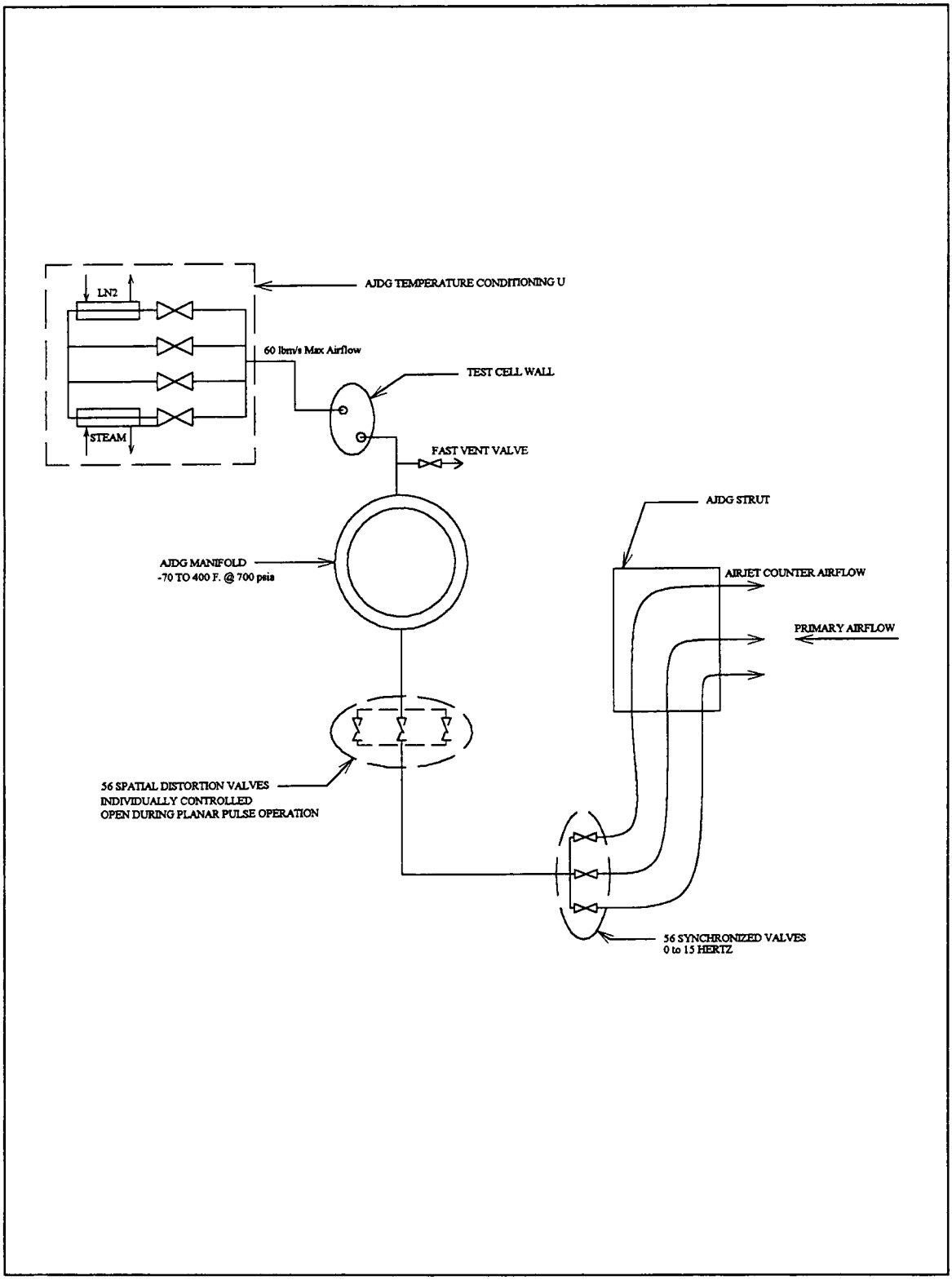


Figure 9, Functional Schematic of the AJDG/PP System in C-1

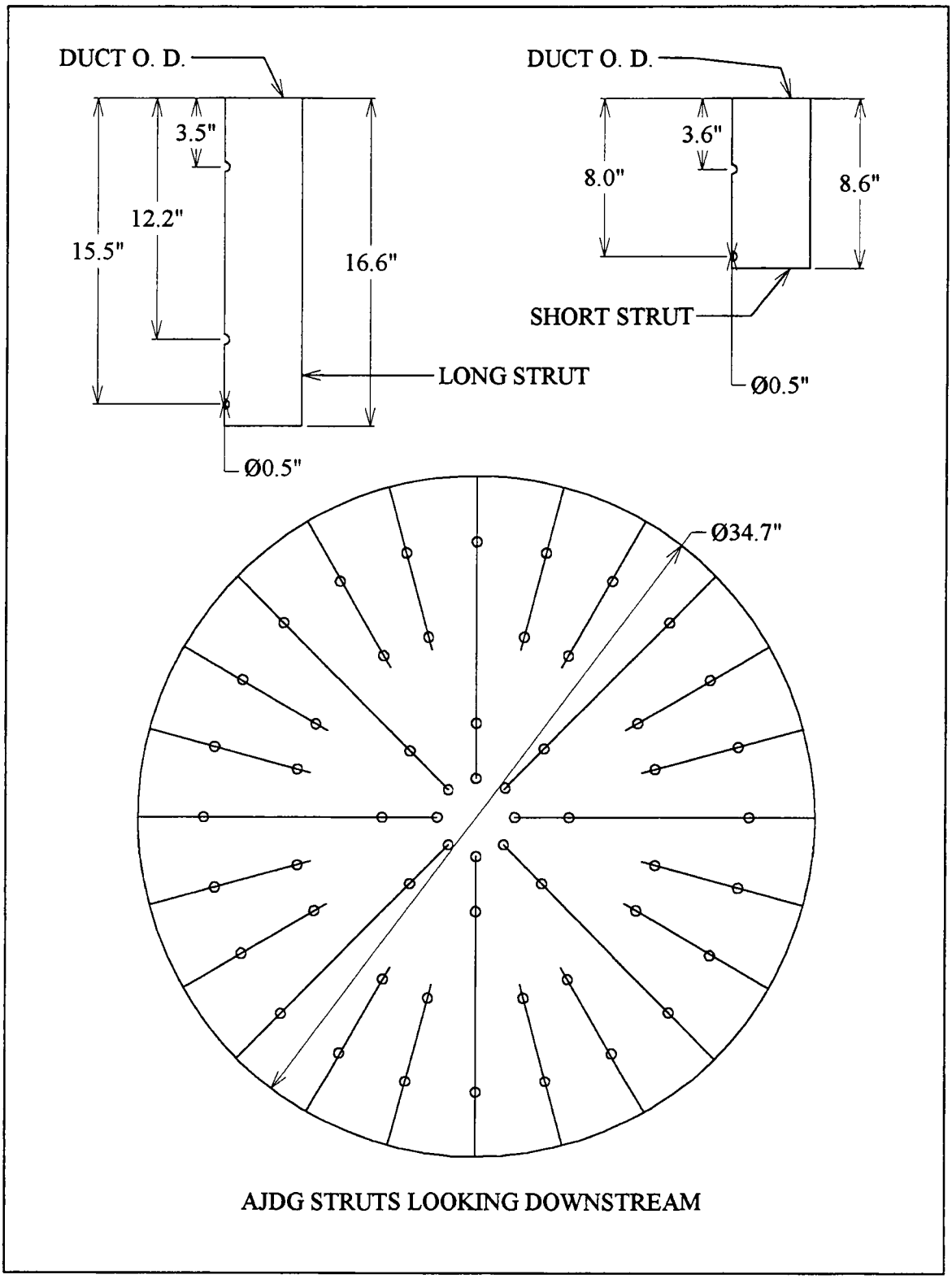


Figure 10, AJDG Strut Details

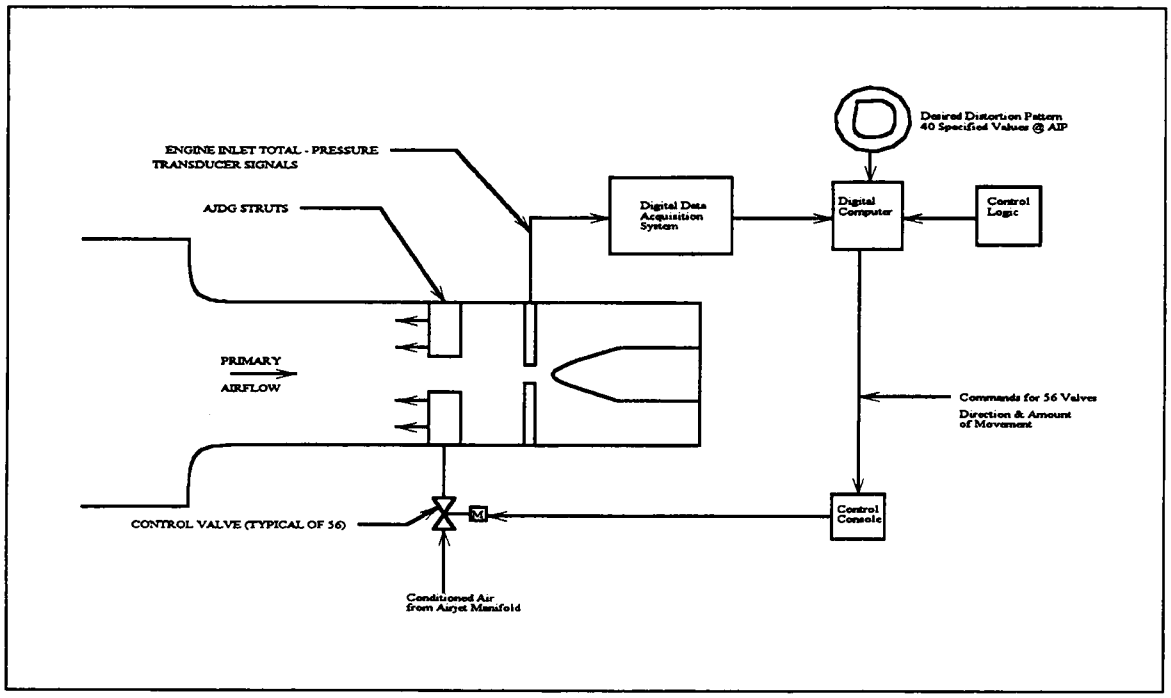


Figure 11, Functional Schematic of the AJDG Airflow Distribution System

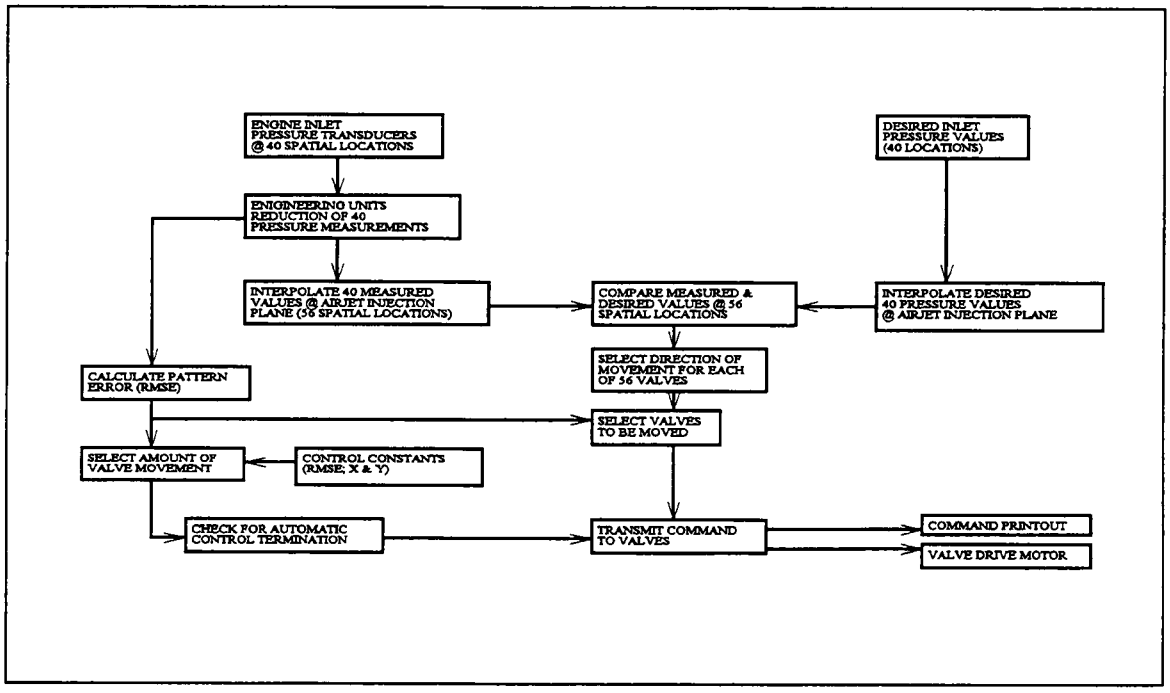


Figure 12, Logic Block Diagram for the AJDG Airflow Distribution System

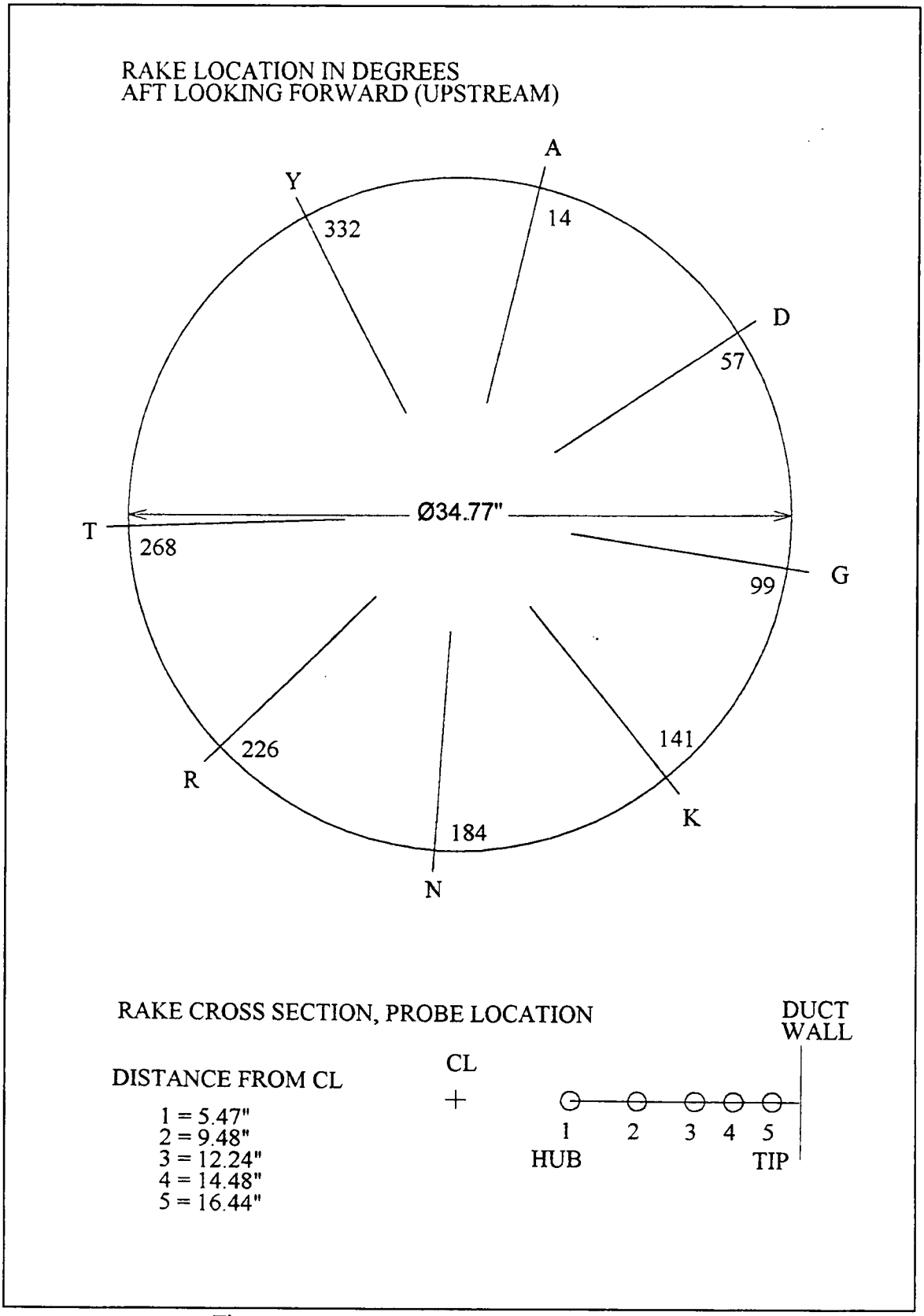


Figure 13, AIP Rake and Probe Location Details

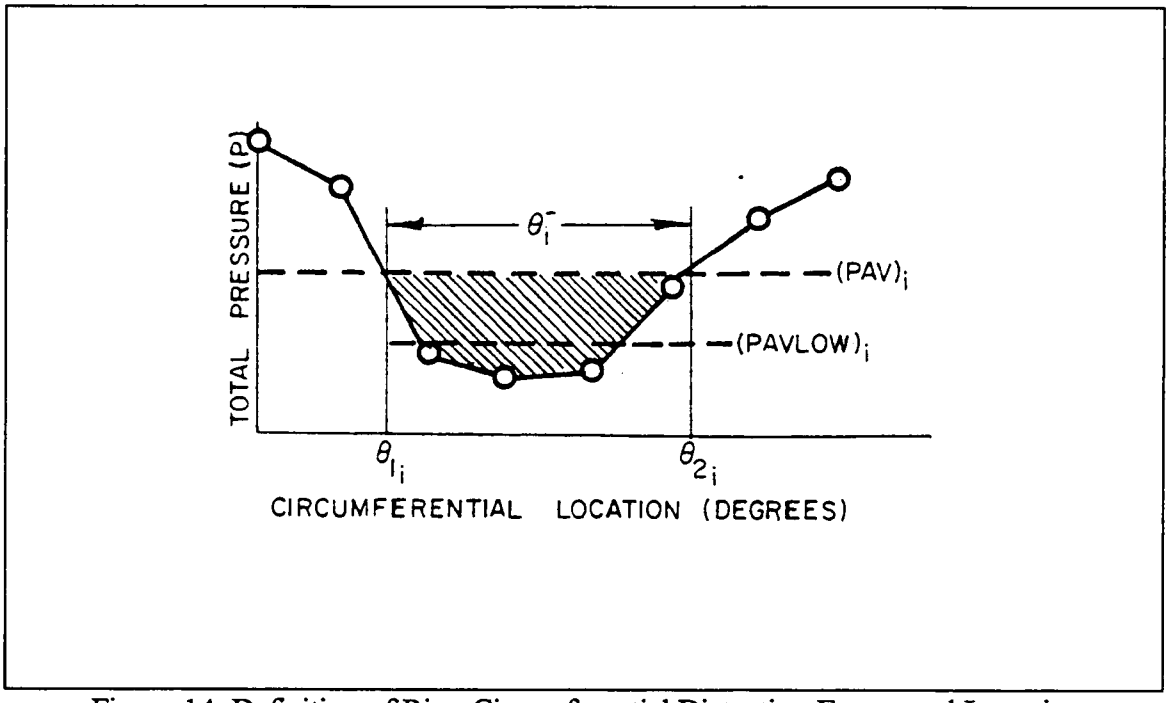


Figure 14, Definition of Ring Circumferential Distortion Extent and Intensity
Source(s): SAE S-16 Committee, AIR 1419, "Inlet Total-Pressure Distortion Considerations for Gas Turbine Engines," Society of Automotive Engineers, Inc., May 1983.

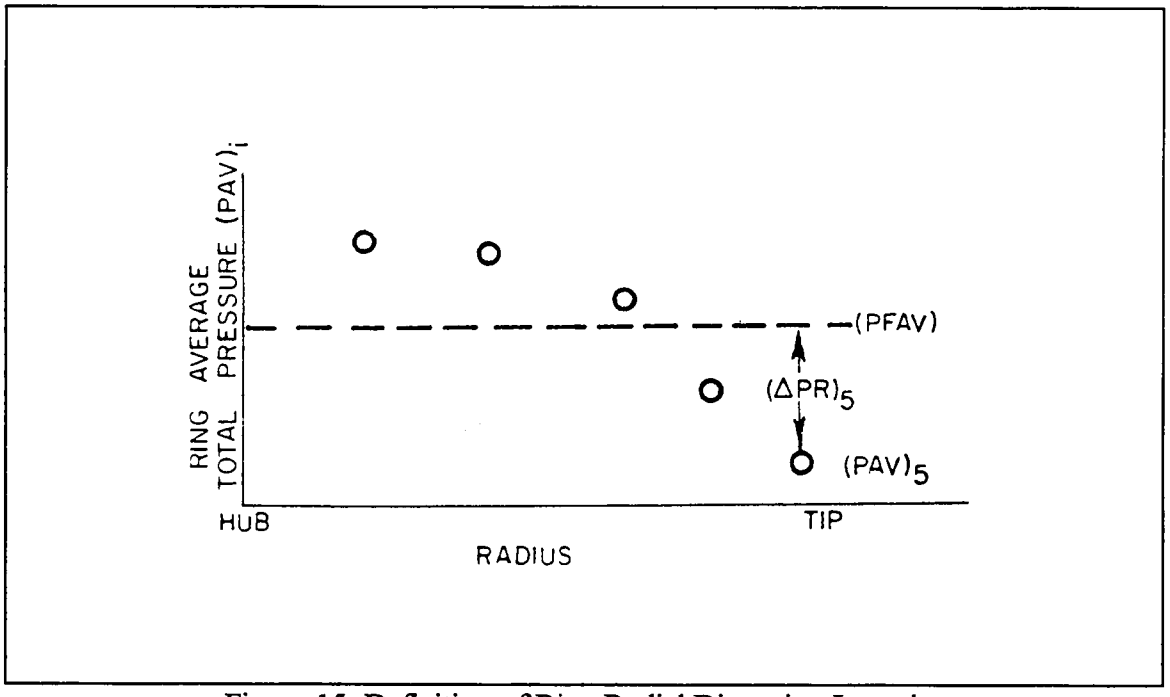
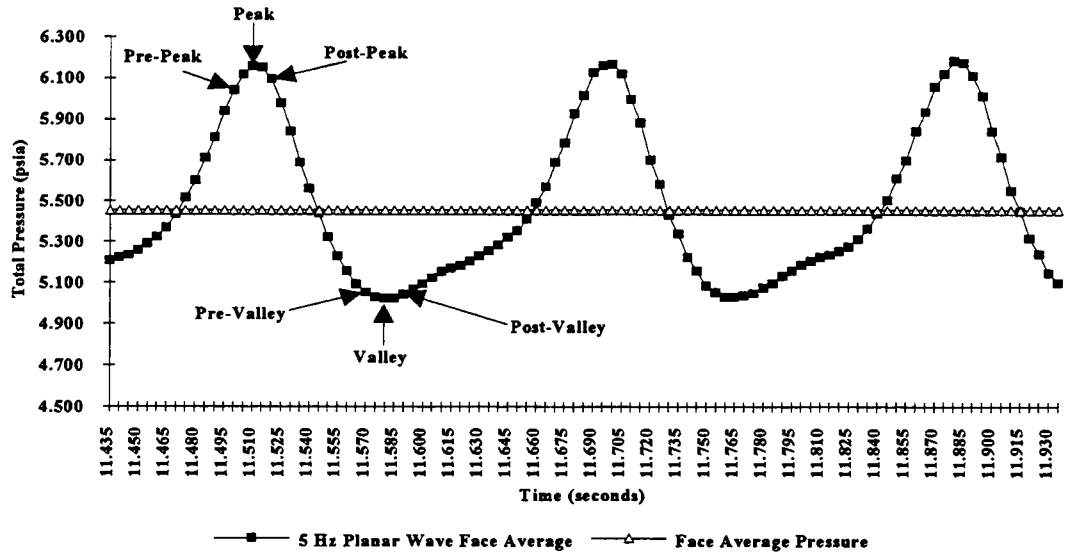


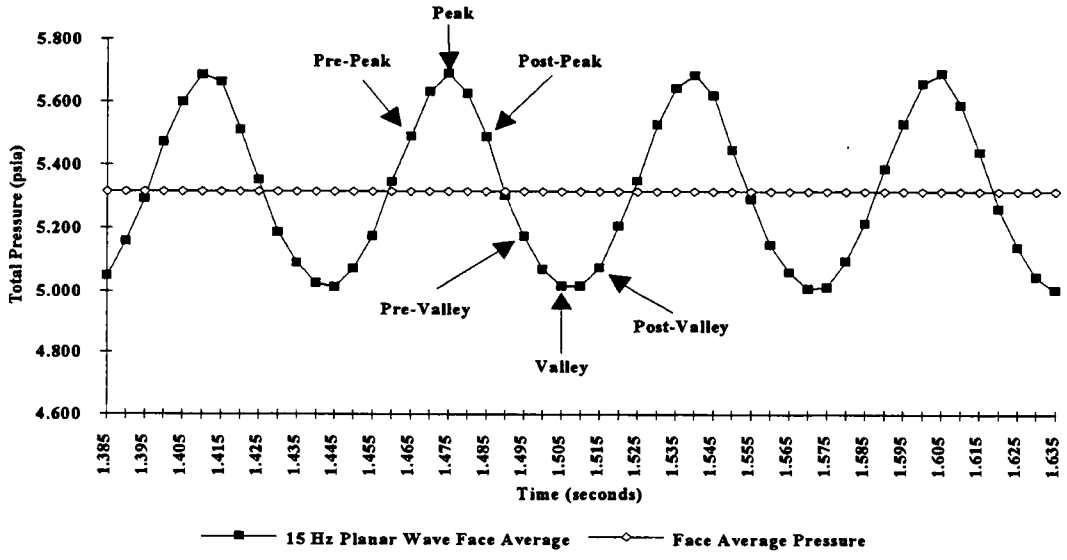
Figure 15, Definition of Ring Radial Distortion Intensity
Source(s): SAE S-16 Committee, AIR 1419, "Inlet Total-Pressure Distortion Considerations for Gas Turbine Engines," Society of Automotive Engineers, Inc., May 1983.

Table 1, Rake & Probe Substtitution Summary

Data Point	Probe/Rake	Substitute Probe	Substitute Rake(s)
65	5/N	5	K & R
65	3/D	3	A & G
179	5/N	5	K & R
179	4/R	4	N & T
179	3/D	3	A & G
179	2/G	2	D & K
179	2/R	2	N & T



a. 5 Hz Planar Wave and Face Average Pressure vs. Time



b. 15 Hz Planar Wave and Face Average Pressure vs. Time
Figure 16, AJDG Created Planar Waveforms

Table 2, Individual Probe Pressures from Data Point 65 "Pre-Peak"

RAKE	A 14°	D 57°	G 99°	K 141°	N 184°	R 226°	T 268°	Y 332°
RING								
Hub	6.085	6.059	6.116	6.128	6.085	6.070	6.005	6.133
2	6.173	6.170	6.178	6.122	6.052	5.935	6.089	6.248
3	6.165	6.115	6.027	6.185	5.972	6.073	6.090	6.290
4	6.089	6.131	5.968	6.126	6.030	6.144	6.003	6.304
Tip	6.043	5.897	5.874	5.947	5.784	5.977	5.927	6.128

Table 3, Data Point 65 "Pre-Peak" Reduced Data

Ring Number	PAV (psia)	PAVLOW (psia)	DPC/P	DPR/P	Extent (Low) (degrees)	Extent (High) (degrees)	PFAV (psia)
1	6.084	6.059	0.0041	-0.0013	181.39	178.61	6.076
2	6.124	6.040	0.0138	-0.0078	142.39	217.61	6.076
3	6.119	6.062	0.0094	-0.0071	193.18	166.82	6.076
4	6.103	6.054	0.0079	-0.0043	197.32	162.68	6.076
5	5.952	5.894	0.0098	0.0205	208.51	151.49	6.076

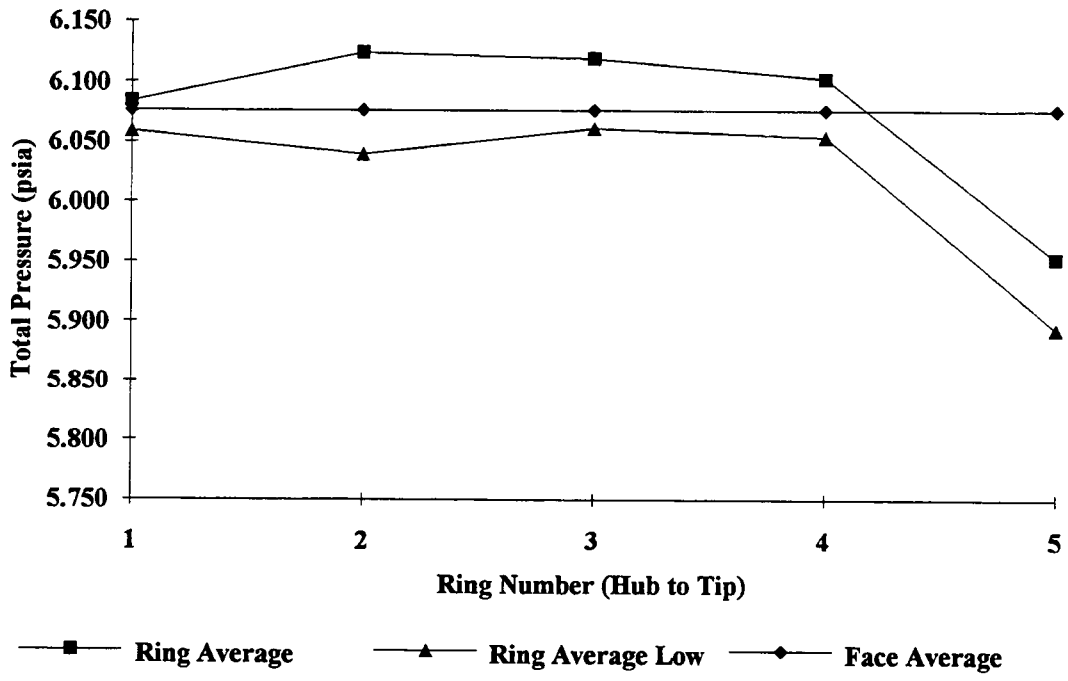


Figure 17, Data Point 65 "Pre-Peak" Ring Average Total Pressure

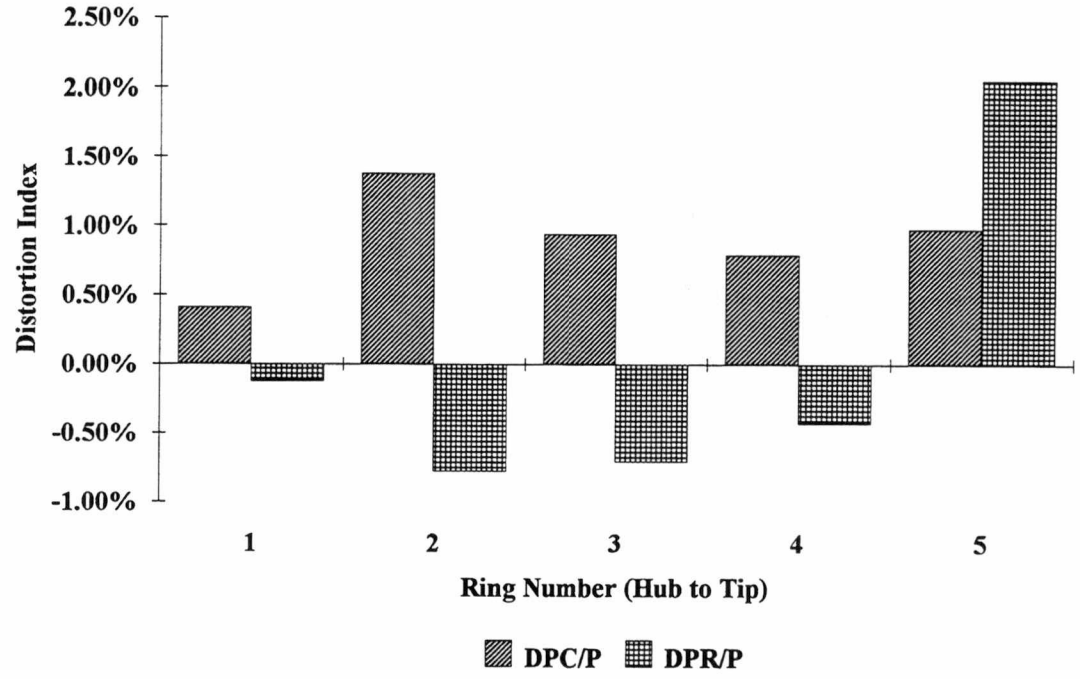


Figure 18, Data Point 65 "Pre-Peak" Circumferential and Radial Distortion Intensity

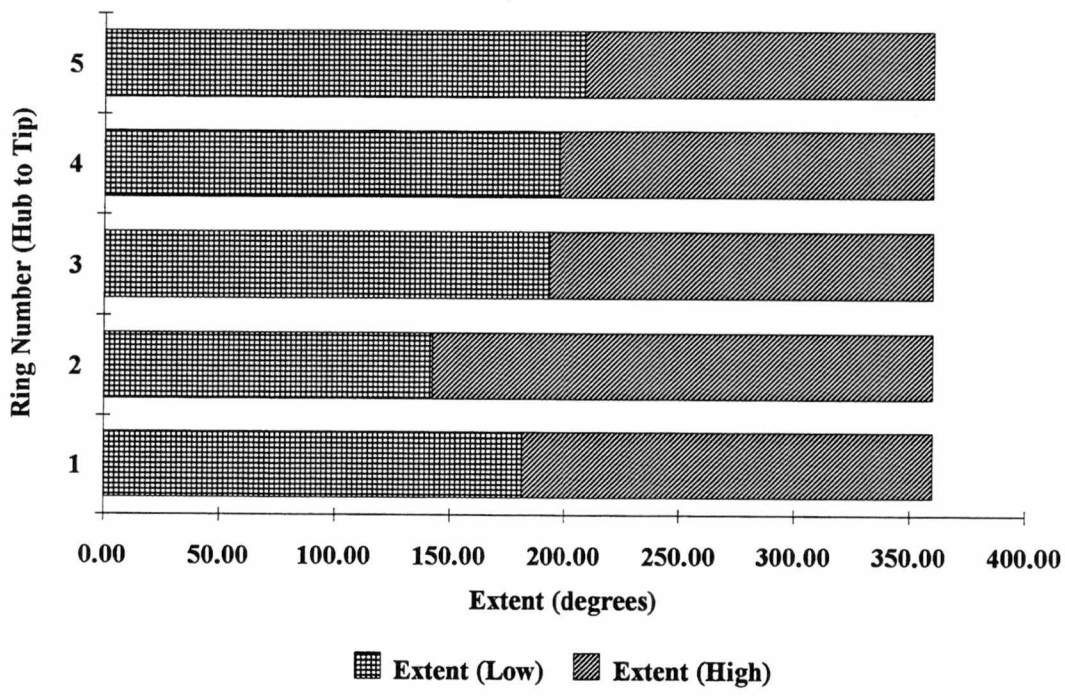


Figure 19, Data Point 65 "Pre-Peak" Circumferential Extent

Table 4, Individual Probe Pressures from Data Point 65 "Peak"

RAKE	A 14°	D 57°	G 99°	K 141°	N 184°	R 226°	T 268°	Y 332°
RING								
HUB	6.182	6.173	6.264	6.204	6.136	6.204	6.124	6.171
2	6.363	6.227	6.393	6.222	6.171	6.053	6.247	6.191
3	6.370	6.252	6.251	6.266	6.100	6.245	6.266	6.267
4	6.247	6.270	6.173	6.169	6.172	6.319	6.179	6.257
TIP	6.085	6.035	6.023	6.023	5.936	6.096	6.047	6.132

Table 5, Data Point 65 "Peak" Reduced Data

Ring Number	PAV (psia)	PAVLOW (psia)	DPC/P	DPR/P	Extent (Low) (degrees)	Extent (High) (degrees)	PFAV (psia)
1	6.180	6.160	0.0032	-0.0015	220.30	139.70	6.171
2	6.233	6.172	0.0097	-0.0100	187.29	172.71	6.171
3	6.253	6.208	0.0072	-0.0133	145.46	214.54	6.171
4	6.223	6.185	0.0061	-0.0084	170.30	189.70	6.171
5	6.050	6.011	0.0065	0.0196	173.46	186.54	6.171

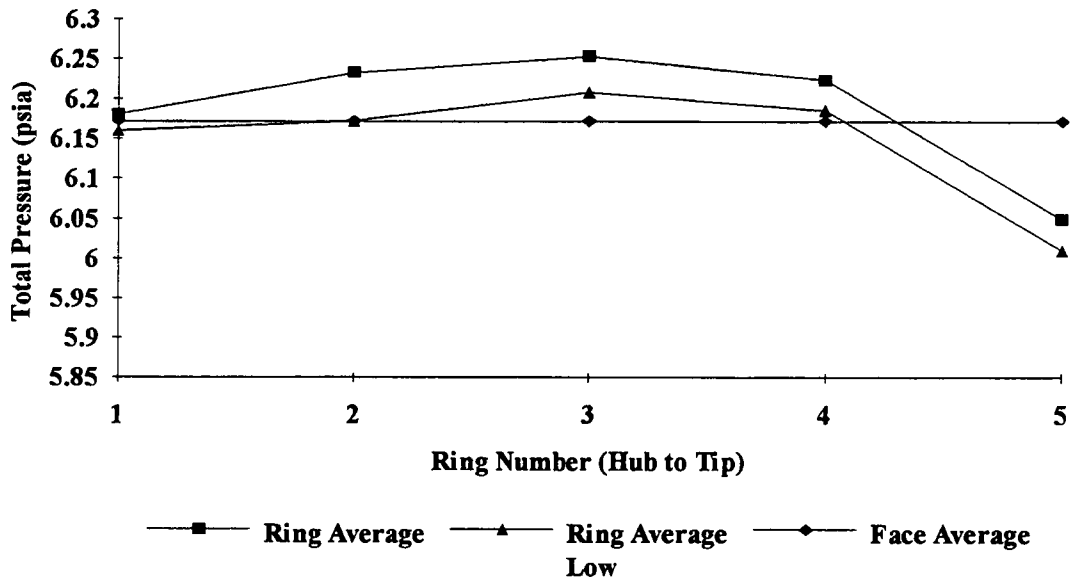


Figure 20, Data Point 65 "Peak" Ring Average Total Pressure

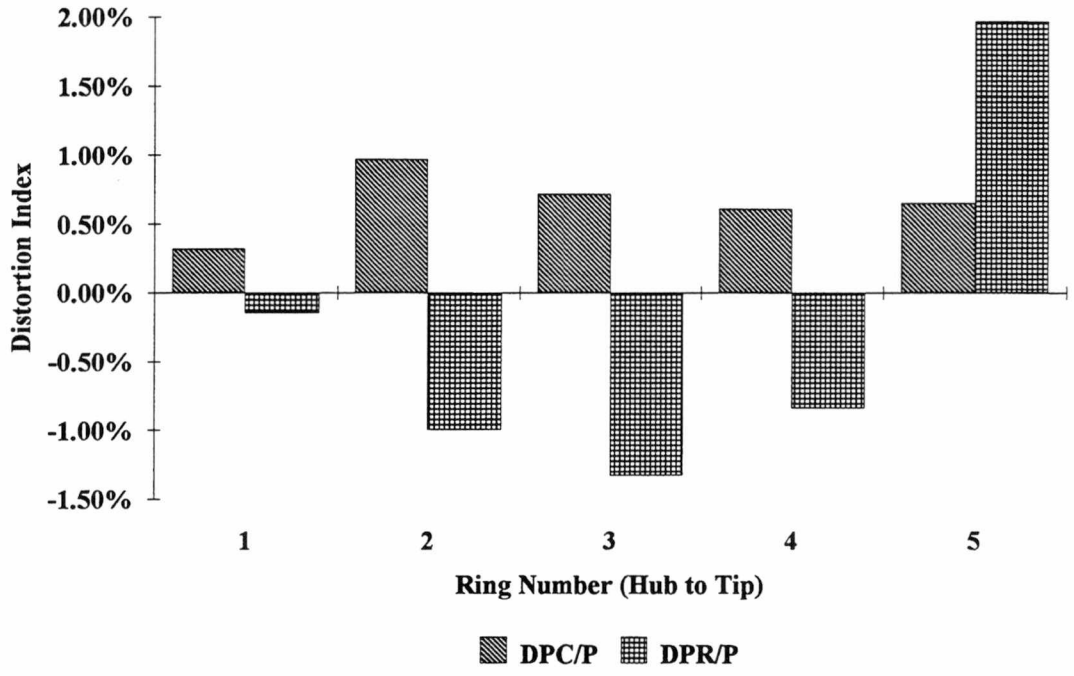


Figure 21, Data Point 65 "Peak" Circumferential and Radial Distortion Intensity

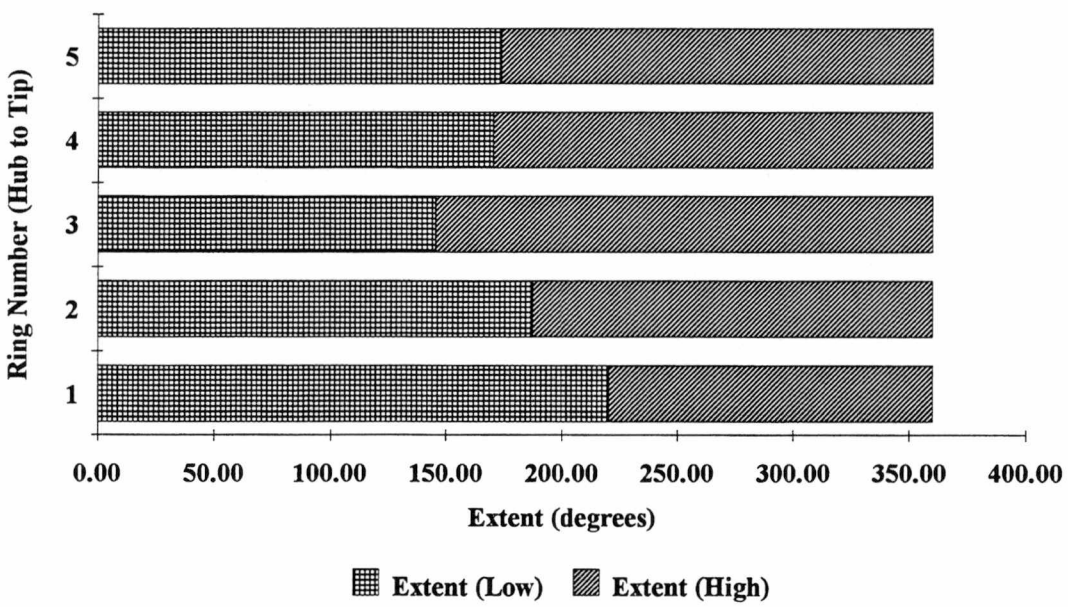


Figure 22, Data Point 65 Peak Circumferential Extent

Table 6, Individual Probe Pressures from Data Point 65 "Post-Peak"

RAKE	A 14°	D 57°	G 99°	K 141°	N 184°	R 226°	T 268°	Y 332°
RING								
HUB	6.135	6.178	6.350	6.027	6.097	6.194	6.053	6.047
2	6.230	6.127	6.531	6.127	6.185	5.987	6.137	5.971
3	6.251	6.204	6.418	6.123	6.158	6.274	6.214	5.990
4	6.156	6.098	6.274	6.021	6.101	6.210	6.098	5.985
TIP	6.028	6.016	6.046	5.899	6.012	6.034	5.975	5.923

Table 7, Data Point 65 "Post-Peak" Reduced Data

Ring Number	PAV (psia)	PAVLOW (psia)	DPC/P	DPR/P	Extent (Low) (degrees)	Extent (High) (degrees)	PFAV (psia)
1	6.130	6.072	0.0095	-0.0021	196.94	163.06	6.117
2	6.155	6.076	0.0129	-0.0063	210.29	149.71	6.117
3	6.198	6.118	0.0128	-0.0132	160.73	199.27	6.117
4	6.113	6.059	0.0089	0.0006	178.82	181.18	6.117
5	5.989	5.950	0.0065	0.0209	160.34	199.66	6.117

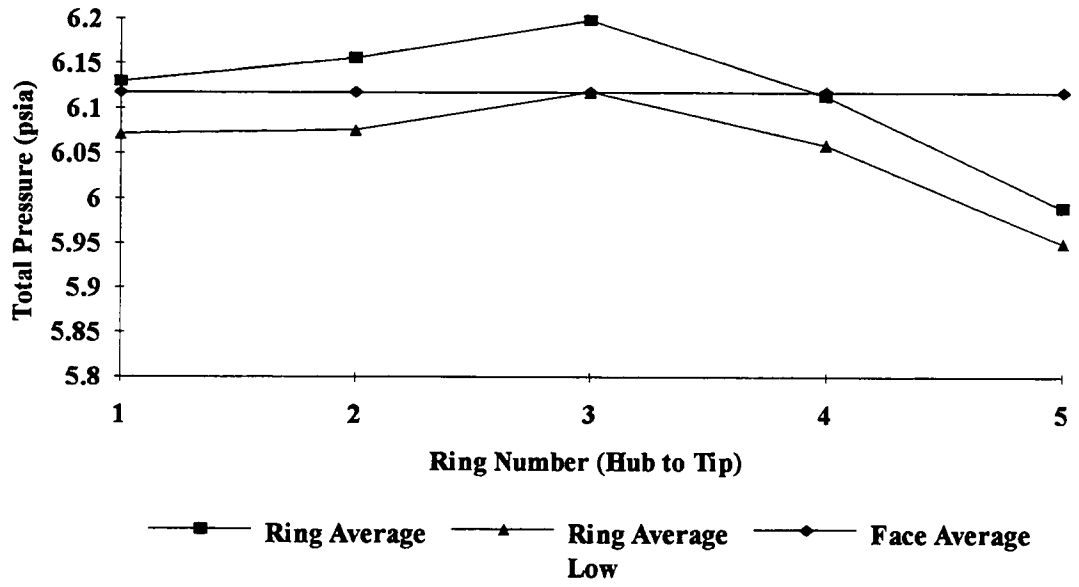


Figure 23, Data Point 65 "Post-Peak" Ring Average Total Pressure

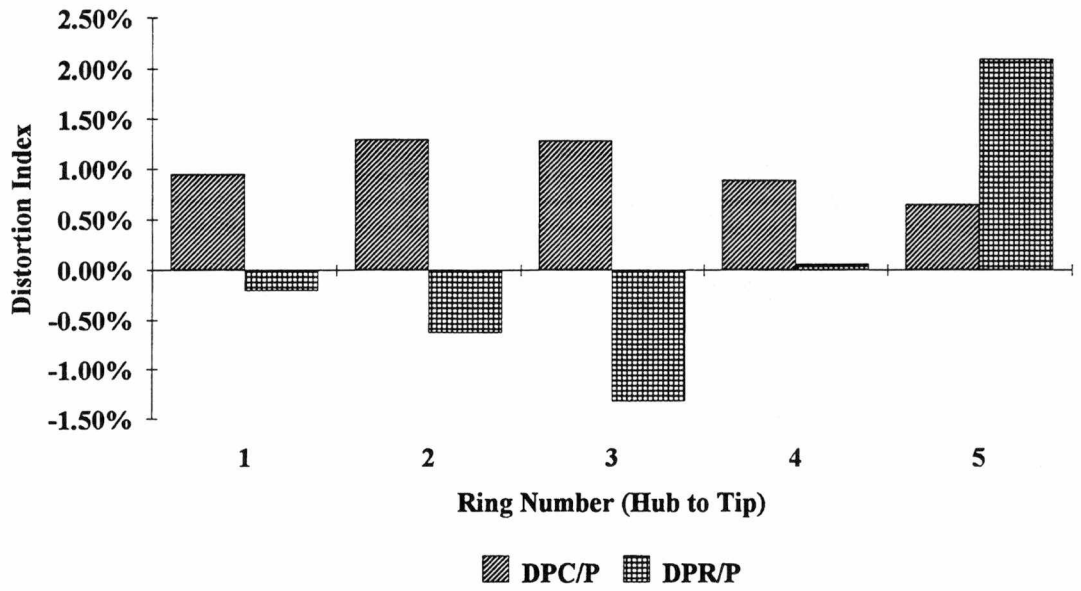


Figure 24, Data Point 65 "Post-Peak" Circumferential and Radial Distortion Intensity

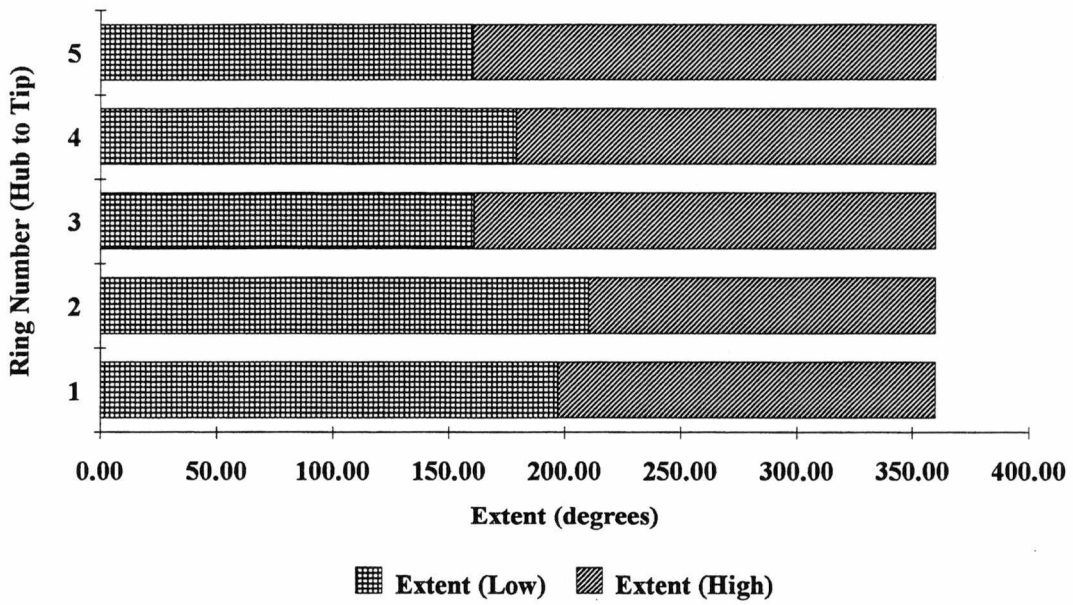


Figure 25, Data Point 65 "Post-Peak" Circumferential Extent

Table 8, Individual Probe Pressures from Data Point 65 "Pre-Valley"

RAKE	A 14°	D 57°	G 99°	K 141°	N 184°	R 226°	T 268°	Y 332°
RING								
HUB	5.197	5.266	5.506	5.068	5.174	5.124	5.135	5.107
2	5.124	5.192	5.585	5.195	5.248	5.022	5.198	5.135
3	5.152	5.220	5.540	5.153	5.308	5.151	5.213	5.024
4	5.136	5.096	5.336	5.085	5.169	5.189	5.175	5.027
TIP	5.045	5.092	5.142	5.014	5.225	5.052	5.113	4.991

Table 9, Data Point 65 "Pre-Valley" Reduced Data

Ring Number	PAV (psia)	PAVLOW (psia)	DPC/P	DPR/P	Extent (Low) (degrees)	Extent (High) (degrees)	PFAV (psia)
1	5.192	5.133	0.0115	-0.0045	242.76	117.24	5.169
2	5.209	5.144	0.0126	-0.0078	240.98	119.02	5.169
3	5.214	5.147	0.0128	-0.0086	227.41	132.59	5.169
4	5.148	5.101	0.0092	0.0040	189.68	170.32	5.169
5	5.082	5.044	0.0075	0.0168	188.66	171.34	5.169

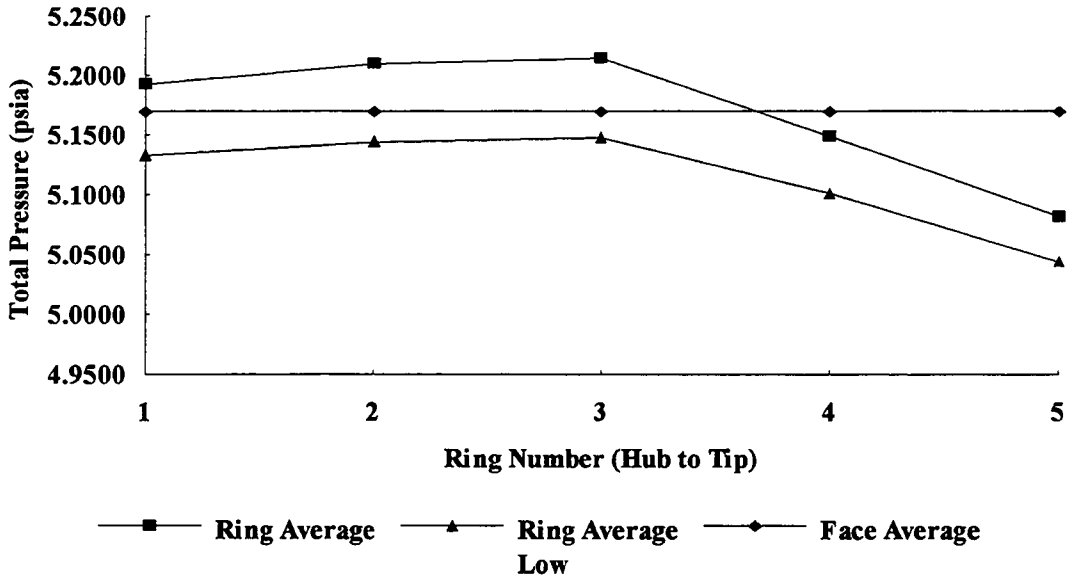


Figure 26, Data Point 65 "Pre-Valley" Ring Average Total Pressure

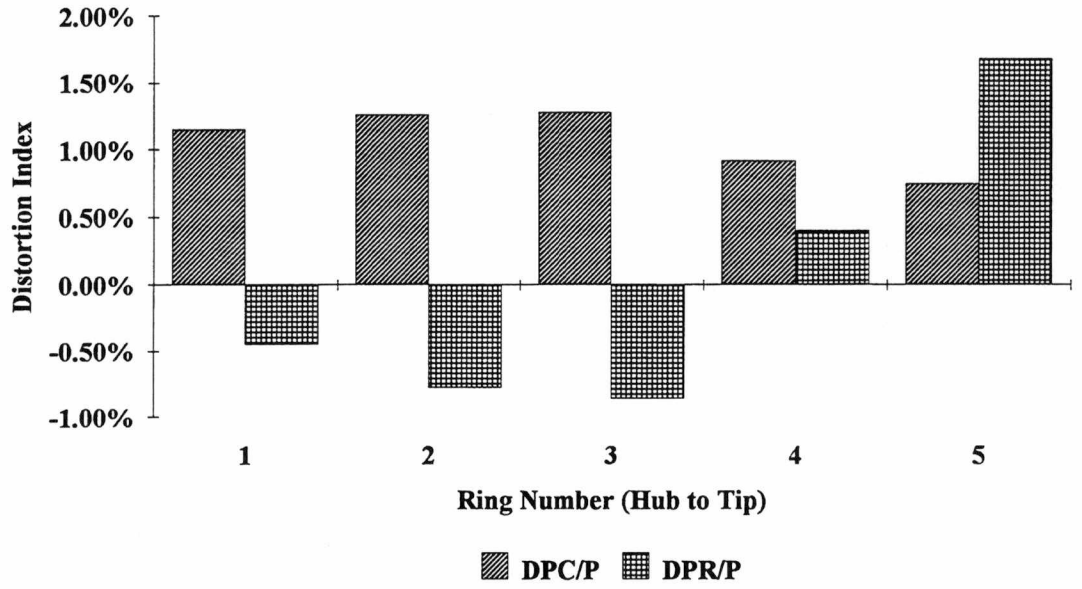


Figure 27, Data Point 65 "Pre-Valley" Circumferential and Radial Distortion Intensity

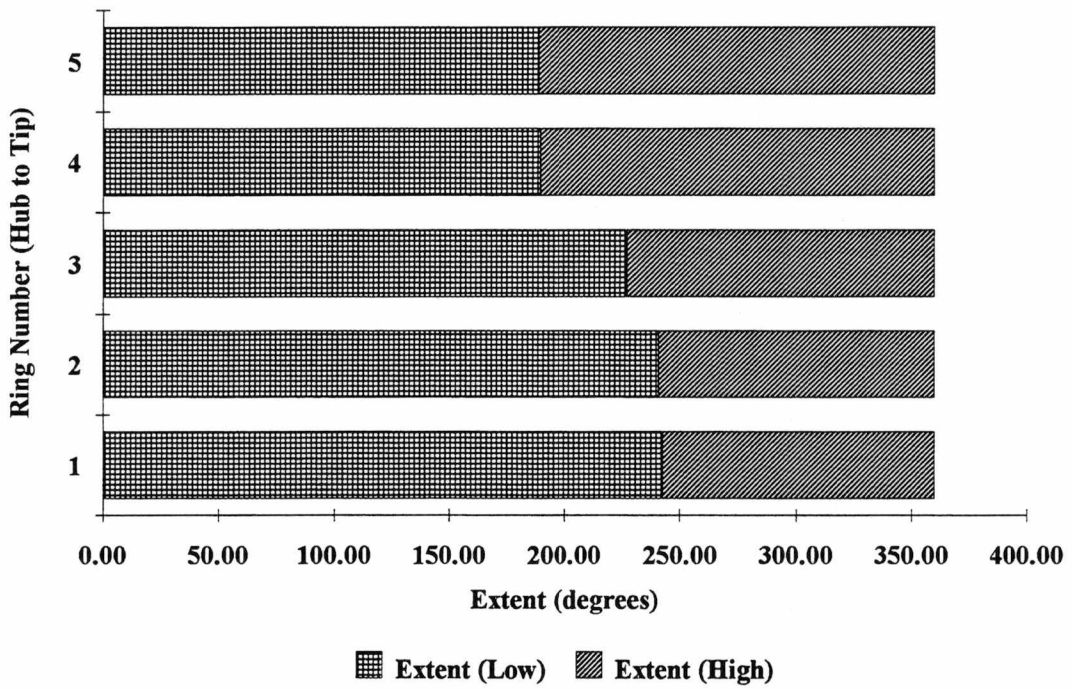


Figure 28, Data Point 65 "Pre-Valley" Circumferential Extent

Table 10, Individual Probe Pressures from Data Point 65 "Valley"

RAKE	A 14°	D 57°	G 99°	K 141°	N 184°	R 226°	T 268°	Y 332°
RING								
HUB	5.098	5.114	5.416	4.991	5.073	5.024	5.035	5.031
2	5.057	5.082	5.480	5.100	5.143	4.946	5.103	5.088
3	5.032	5.111	5.378	5.053	5.189	5.031	5.113	4.981
4	5.021	5.039	5.169	4.985	5.108	5.052	5.071	4.974
TIP	4.974	4.958	4.998	4.895	5.098	4.933	5.017	4.905

Table 11, Data Point 65 "Valley" Reduced Data

Ring Number	PAV (psia)	PAVLOW (psia)	DPC/P	DPR/P	Extent (Low) (degrees)	Extent (High) (degrees)	PFAV (psia)
1	5.094	5.040	0.0105	-0.0048	240.41	119.59	5.069
2	5.123	5.069	0.0106	-0.0106	258.49	101.51	5.069
3	5.107	5.052	0.0108	-0.0075	227.11	132.89	5.069
4	5.051	5.015	0.0070	0.0037	176.99	183.01	5.069
5	4.972	4.946	0.0052	0.0192	206.09	153.91	5.069

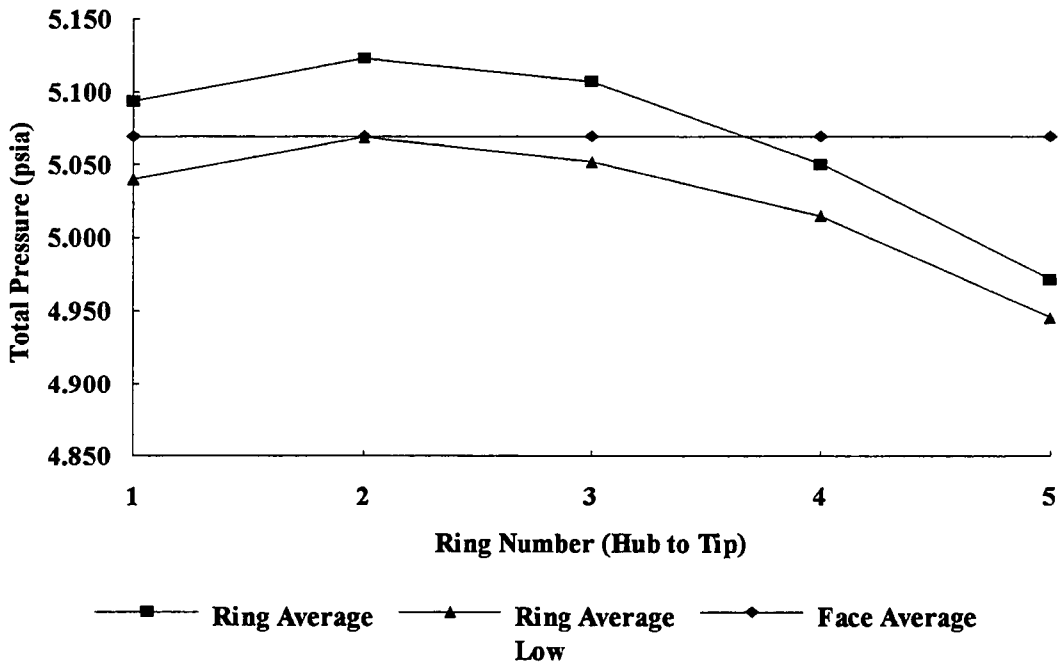


Figure 29, Data Point 65 "Valley" Ring Average Total Pressure

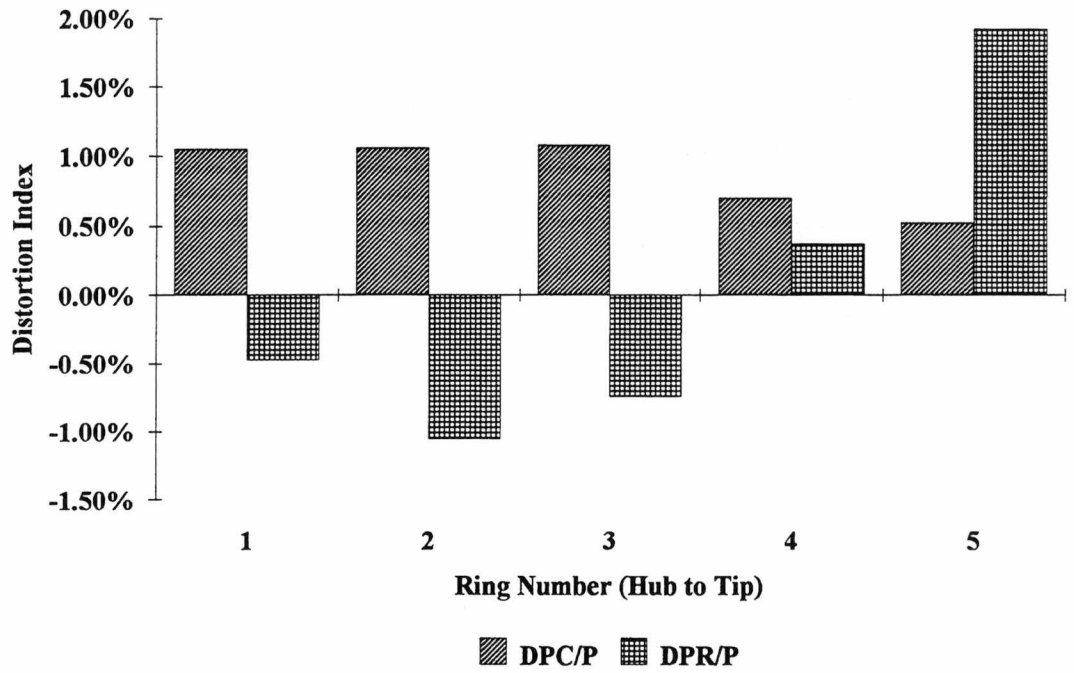


Figure 30, Data Point 65 "Valley" Circumferential and Radial Distortion Intensity

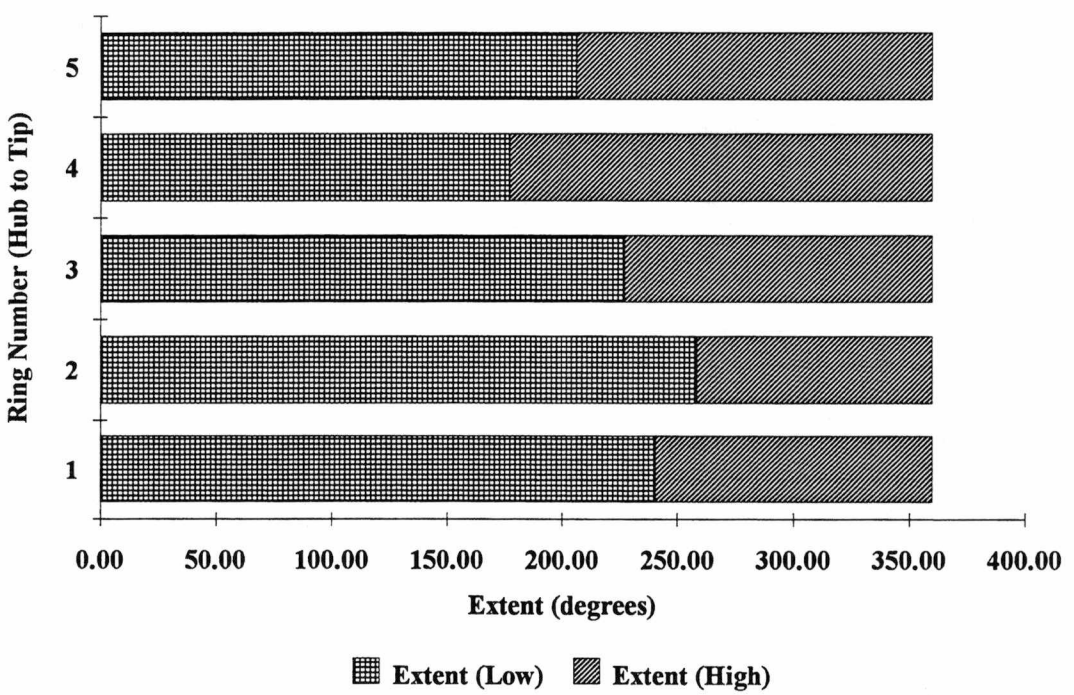


Figure 31, Data Point 65 "Valley" Circumferential Extent

Table 12, Individual Probe Pressures from Data Point 65 "Post-Valley"

RAKE	A 14°	D 57°	G 99°	K 141°	N 184°	R 226°	T 268°	Y 332°
RING								
HUB	5.062	5.019	5.368	5.020	5.040	4.977	5.007	5.002
2	5.048	5.053	5.337	5.114	5.076	4.922	5.069	5.069
3	5.032	5.084	5.340	5.058	5.103	4.959	5.084	5.014
4	4.997	4.981	5.155	4.932	5.041	5.057	5.042	5.003
TIP	4.931	4.920	4.922	4.871	5.012	4.895	4.984	4.962

Table 13, Data Point 65 "Post-Valley" Reduced Data

Ring Number	PAV (psia)	PAVLOW (psia)	DPC/P	DPR/P	Extent (Low) (degrees)	Extent (High) (degrees)	PFAV (psia)
1	5.058	5.017	0.0082	-0.0040	278.91	81.09	5.038
2	5.085	5.040	0.0088	-0.0093	247.77	112.23	5.038
3	5.082	5.039	0.0084	-0.0087	249.27	110.73	5.038
4	5.026	4.994	0.0062	0.0025	187.34	172.66	5.038
5	4.939	4.915	0.0049	0.0196	195.88	164.12	5.038

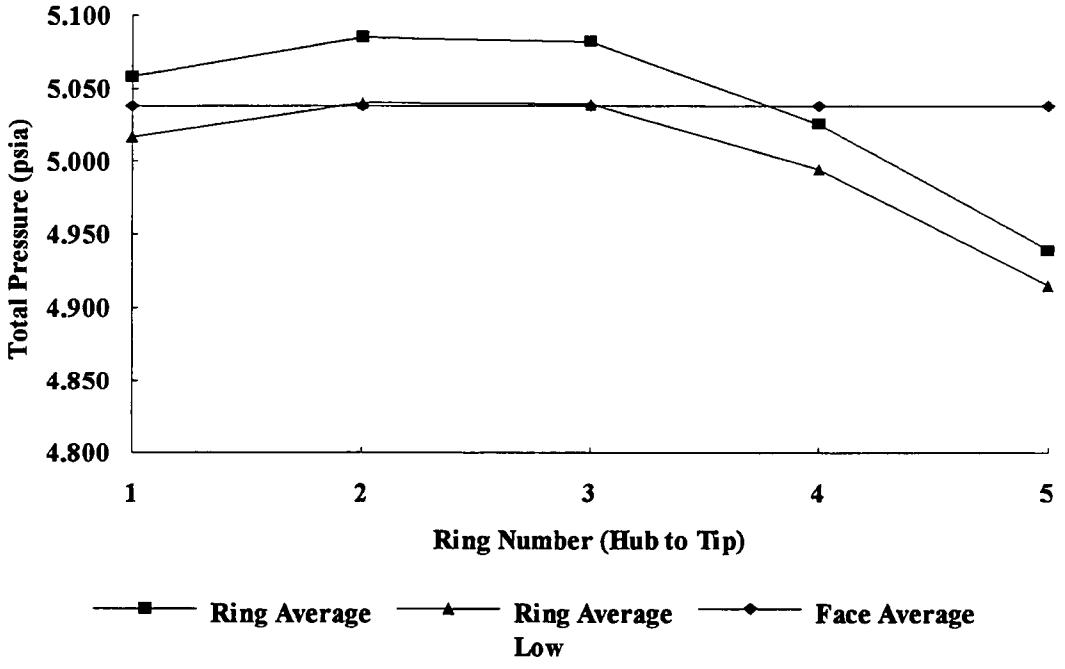


Figure 32, Data Point 65 "Post-Valley" Ring Average Total Pressure

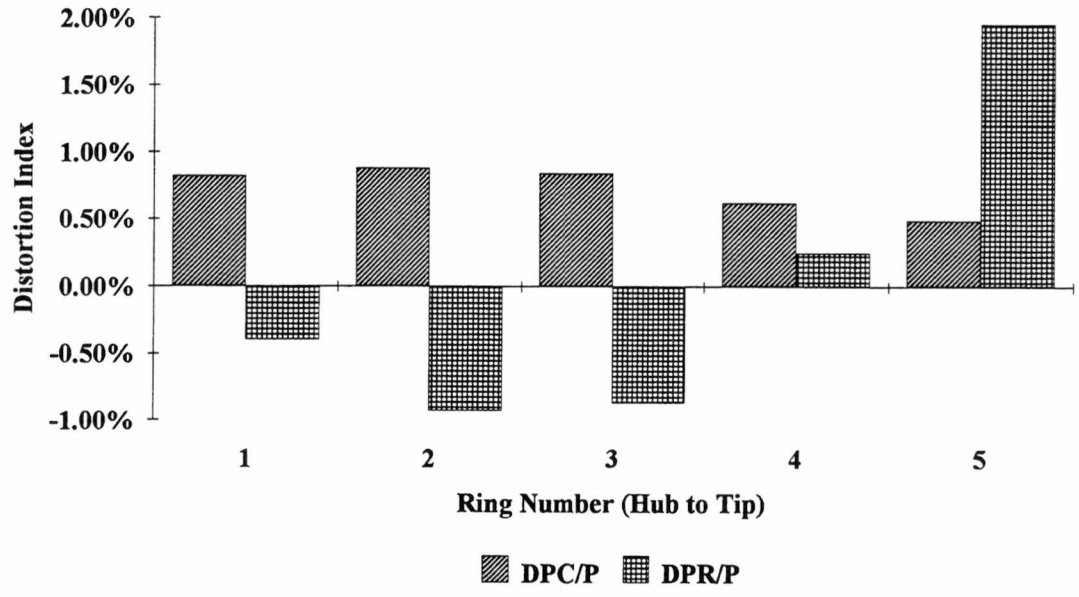


Figure 33, Data Point 65 "Post-Valley" Circumferential and Radial Distortion Intensity

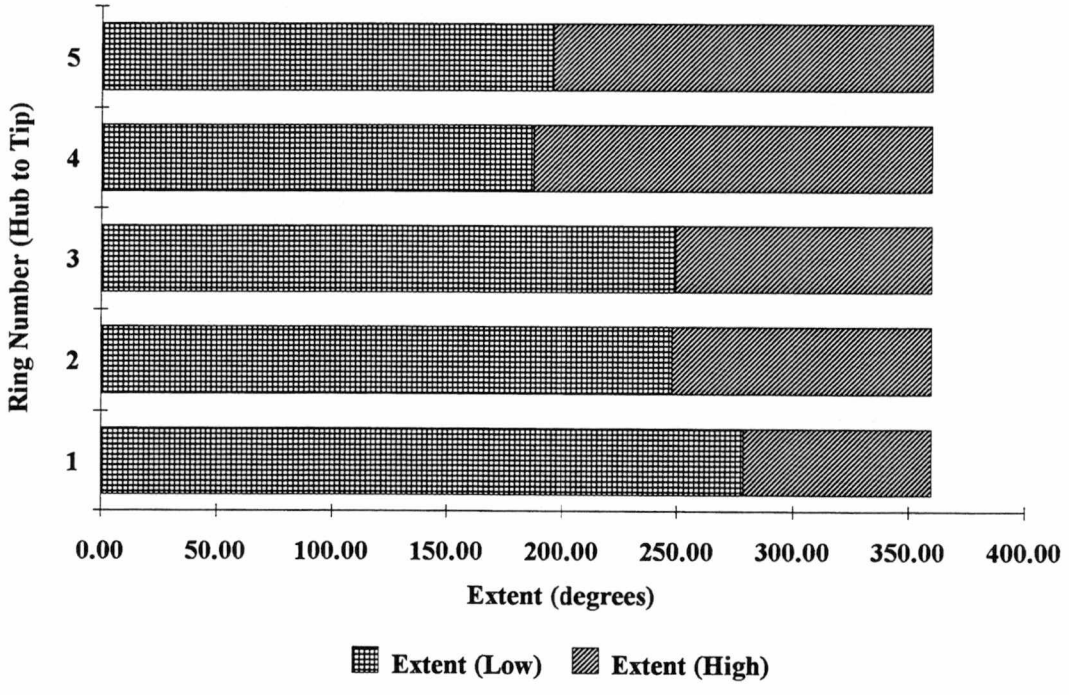


Figure 34, Data Point 65 "Post-Valley" Circumferential Extent

Table 14, Individual Probe Pressures from Data Point 179 "Pre-Peak"

RAKE	A 14°	D 57°	G 99°	K 141°	N 184°	R 226°	T 268°	Y 332°
RING								
HUB	5.758	5.730	5.735	5.574	5.510	5.424	5.539	5.514
2	5.570	5.902	5.683	5.768	5.711	5.683	5.446	5.699
3	5.701	5.638	6.003	5.798	5.585	5.681	5.499	5.200
4	5.855	5.769	6.073	5.711	5.657	5.786	5.799	5.637
TIP	5.434	5.741	5.902	5.744	5.709	5.771	5.782	5.589

Table 15, Data Point 179 "Pre-Peak" Reduced Data

Ring Number	PAV (psia)	PAVLOW (psia)	DPC/P	DPR/P	Extent (Low) (degrees)	Extent (High) (degrees)	PFAV (psia)
1	5.707	5.575	0.0231	-0.0055	209.94	150.06	5.676
2	5.782	5.710	0.0123	-0.0186	147.46	212.54	5.676
3	5.621	5.442	0.0318	0.0097	150.20	209.80	5.676
4	5.676	5.582	0.0167	-0.0001	184.65	175.36	5.676
5	5.594	5.512	0.0146	0.0145	119.50	240.50	5.676

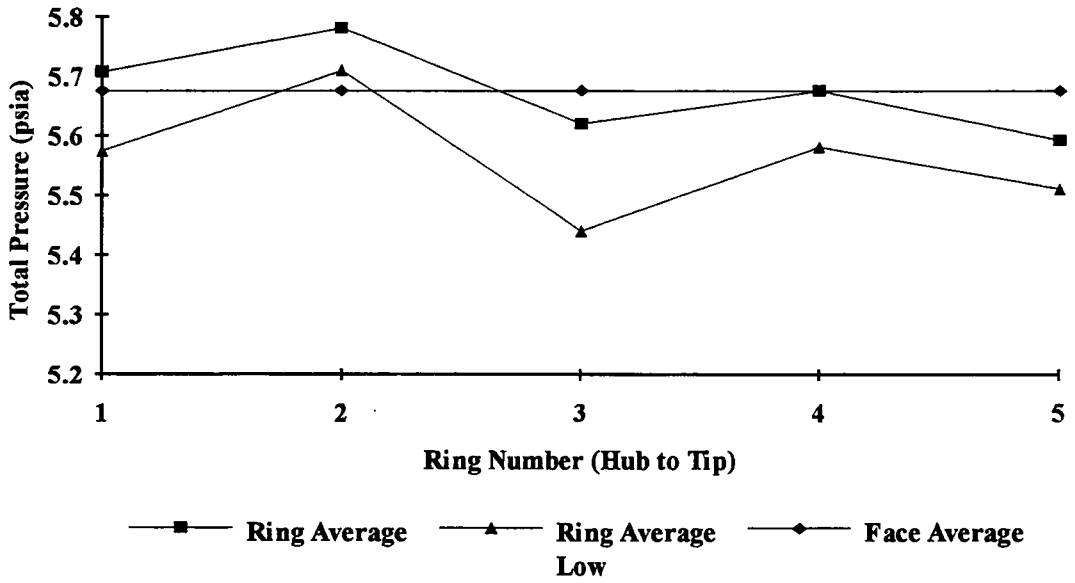


Figure 35, Data Point 179 "Pre-Peak" Ring Average Total Pressure

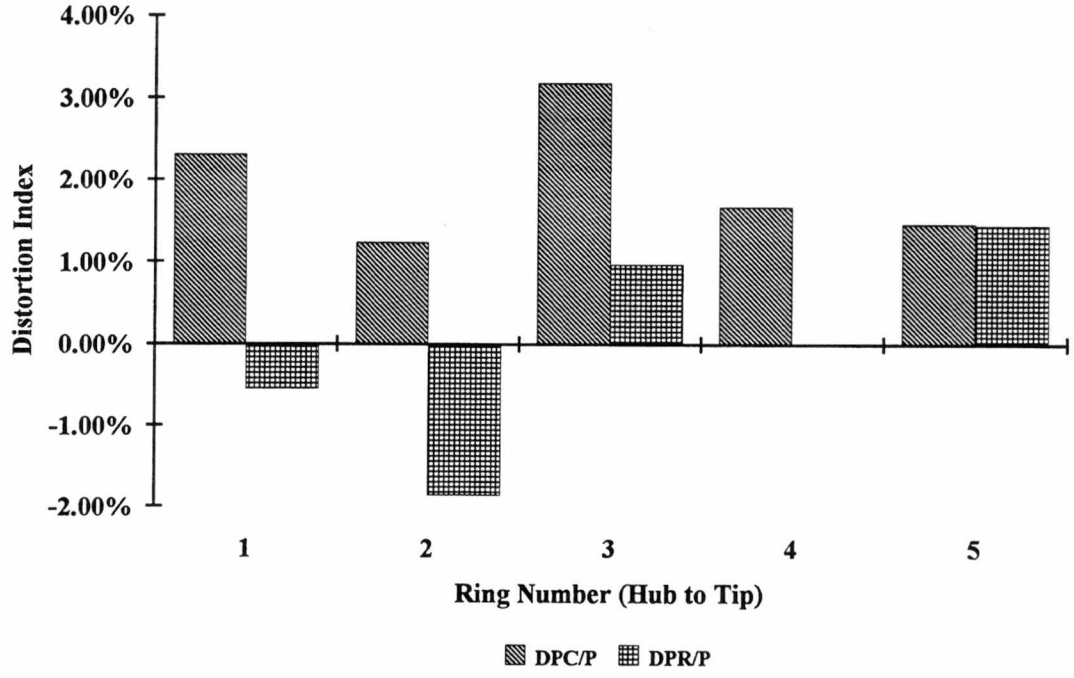


Figure 36, Data Point 179 "Pre-Peak" Circumferential and Radial Distortion Intensity

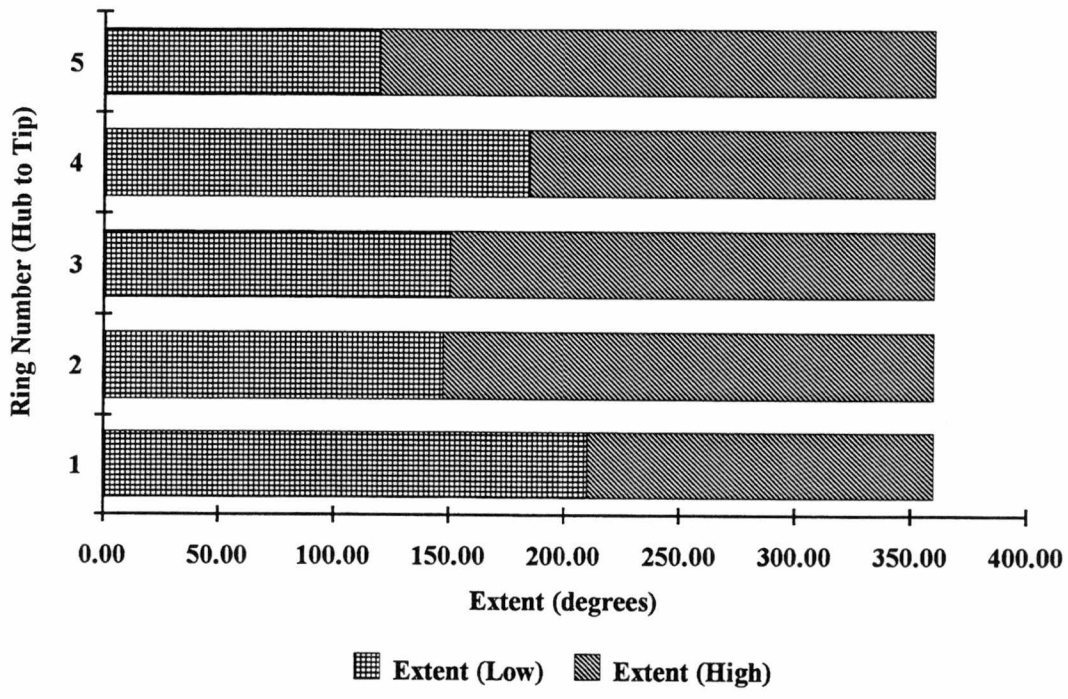


Figure 37, Data Point 179 "Pre-Peak" Circumferential Extent

Table 16, Individual Probe Pressures from Data Point 179 "Peak"

RAKE	A 14°	D 57°	G 99°	K 141°	N 184°	R 226°	T 268°	Y 332°
RING								
HUB	5.810	5.826	5.841	5.827	5.746	5.743	5.769	5.885
2	5.927	5.926	5.901	5.863	5.863	5.901	5.817	6.009
3	5.978	5.898	6.223	5.884	5.833	5.992	5.909	5.467
4	5.974	6.046	6.268	5.878	5.905	6.000	5.984	5.947
TIP	5.572	5.879	6.188	5.941	5.921	5.994	5.953	5.923

Table 17, Data Point 179 "Peak" Reduced Data

Ring Number	PAV (psia)	PAVLOW (psia)	DPC/P	DPR/P	Extent (Low) (degrees)	Extent (High) (degrees)	PFAV (psia)
1	5.922	5.751	0.0288	-0.0032	137.51	222.49	5.903
2	5.998	5.953	0.0075	-0.0161	198.17	161.83	5.903
3	5.885	5.745	0.0239	0.0030	151.84	208.16	5.903
4	5.902	5.870	0.0054	0.0002	253.56	106.44	5.903
5	5.807	5.762	0.0077	0.0162	93.07	266.93	5.903

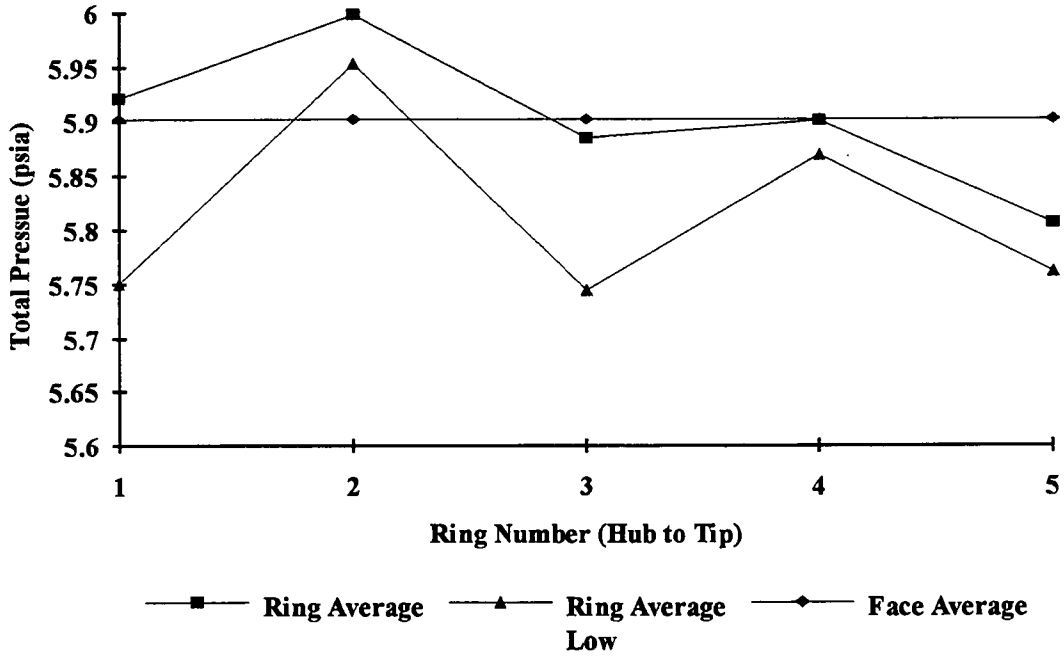


Figure 38, Data Point 179 "Peak" Ring Average Total Pressure

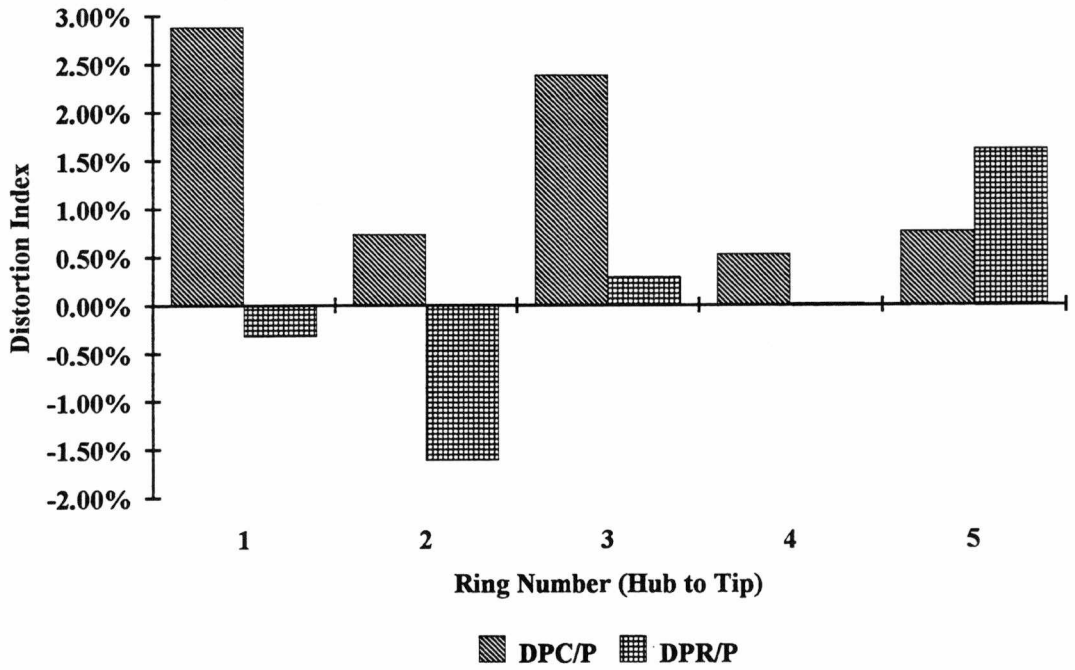


Figure 39, Data Point 179 "Peak" Circumferential and Radial Distortion Intensity

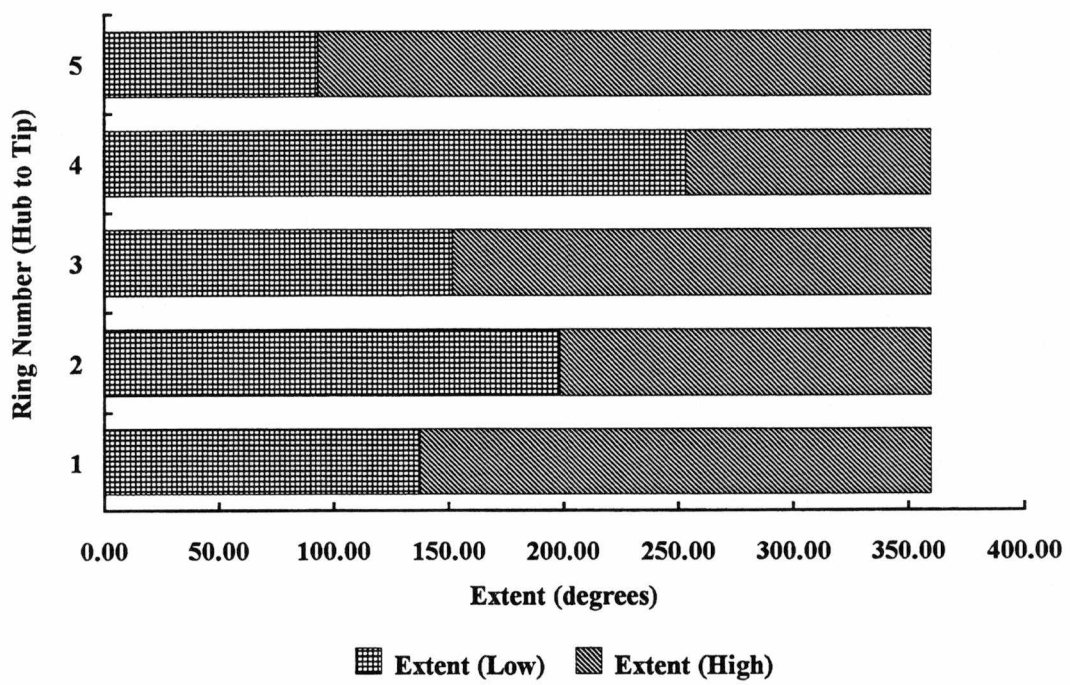


Figure 40, Data Point 179 "Peak" Circumferential Extent

Table 18, Individual Probe Pressures from Data Point 179 "Post-Peak"

RAKE	A 14°	D 57°	G 99°	K 141°	N 184°	R 226°	T 268°	Y 332°
RING								
HUB	5.487	5.483	5.491	5.684	5.704	5.796	5.539	5.752
2	5.770	5.559	5.664	5.496	5.564	5.664	5.803	5.794
3	5.763	5.680	5.736	5.545	5.719	5.739	5.861	5.400
4	5.589	5.836	5.796	5.740	5.733	5.748	5.679	5.866
TIP	5.333	5.599	6.026	5.710	5.698	5.709	5.648	5.861

Table 19, Data Point 179 "Post-Peak" Reduced Data

Ring Number	PAV (psia)	PAVLOW (psia)	DPC/P	DPR/P	Extent (Low) (degrees)	Extent (High) (degrees)	PFAV (psia)
1	5.701	5.589	0.0196	-0.0030	170.54	189.46	5.684
2	5.750	5.714	0.0062	-0.0116	194.49	165.51	5.684
3	5.677	5.573	0.0185	0.0011	132.37	227.63	5.684
4	5.672	5.588	0.0148	0.0020	210.84	149.16	5.684
5	5.619	5.526	0.0166	0.0115	155.43	204.57	5.684

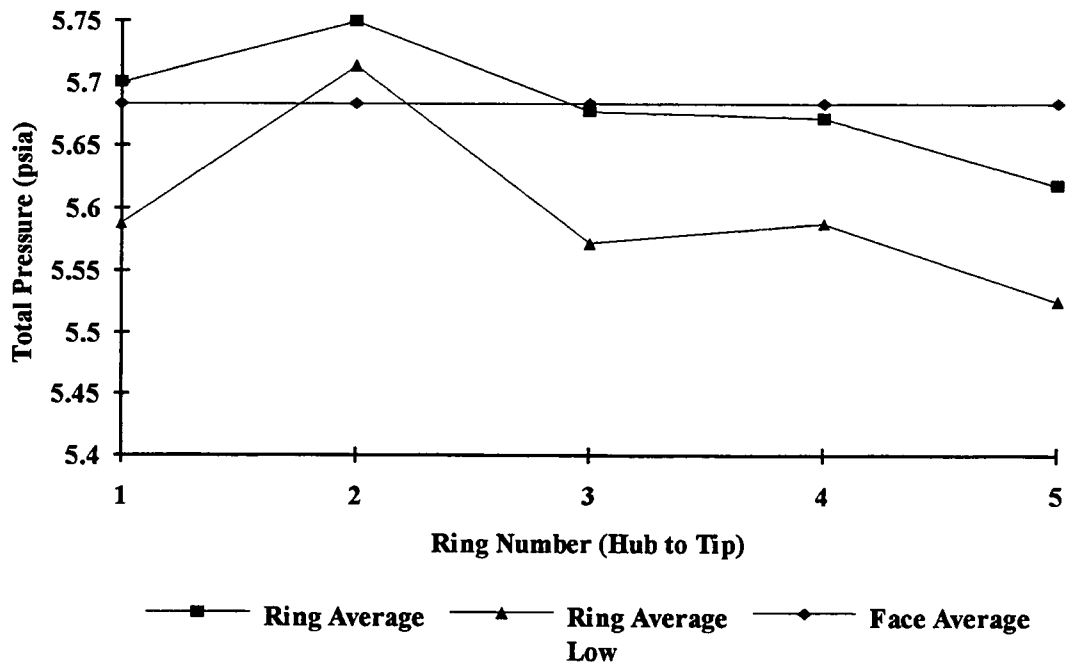


Figure 41, Data Point 179 "Post-Peak" Ring Average Total Pressure

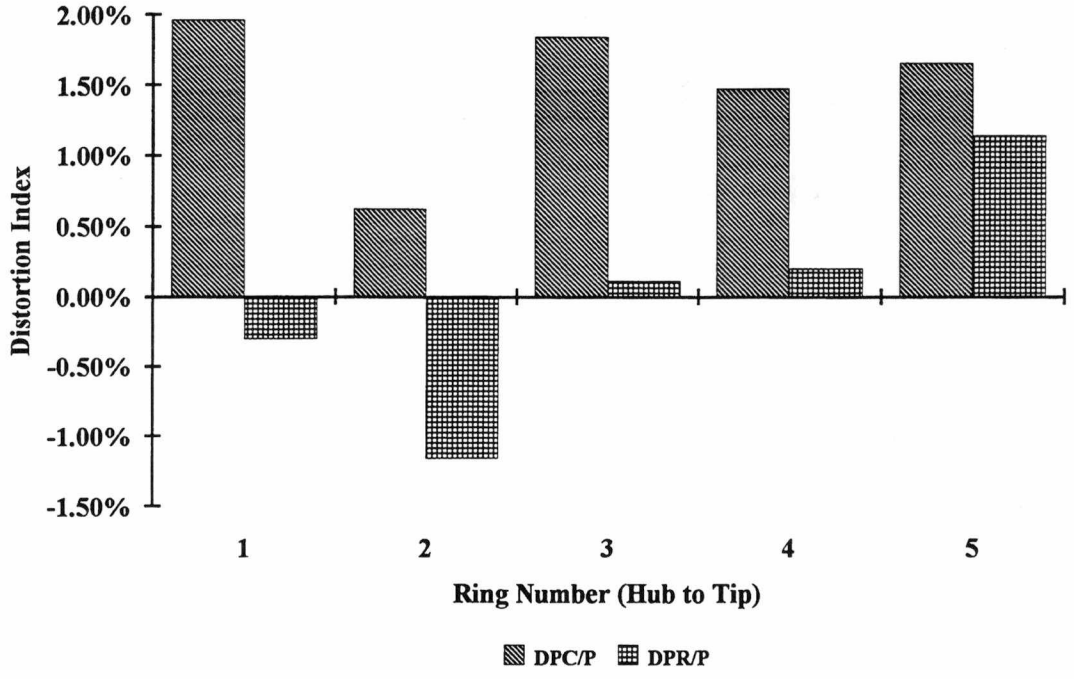


Figure 42, Data Point 179 "Post-Peak" Circumferential and Radial Distortion Intensity

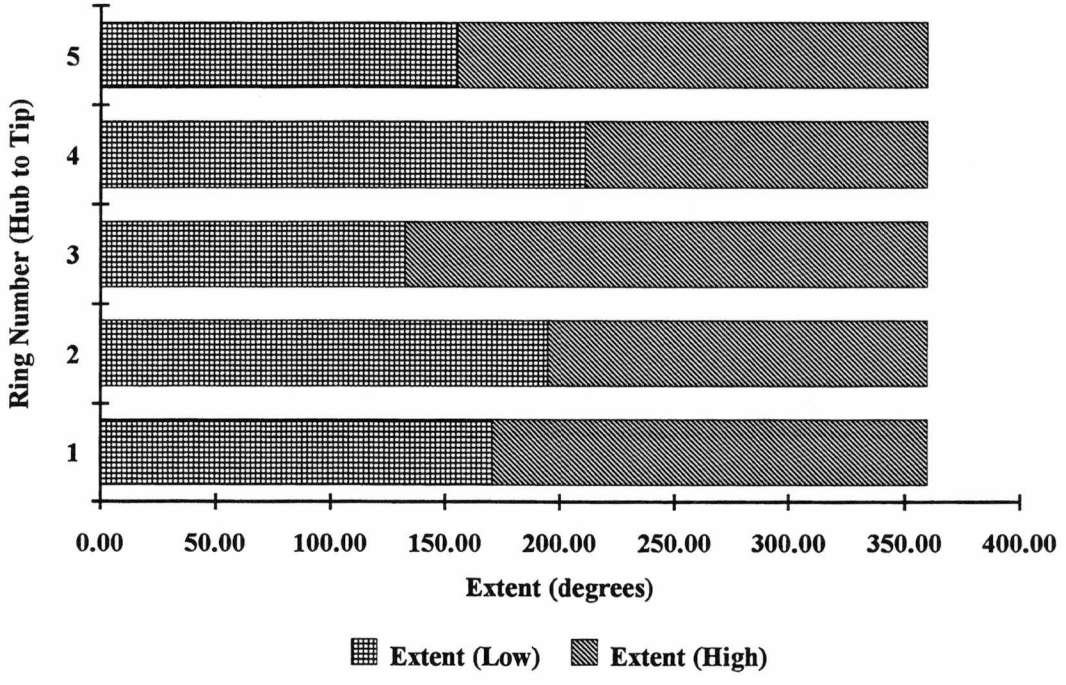


Figure 43, Data Point 179 "Post-Peak" Circumferential Extent

Table 20, Individual Probe Pressures from Data Point 179 "Pre-Valley"

RAKE	A 14°	D 57°	G 99°	K 141°	N 184°	R 226°	T 268°	Y 332°
RING								
HUB	5.197	5.182	5.156	5.301	5.405	5.343	5.218	5.310
2	5.407	5.258	5.310	5.190	5.269	5.310	5.370	5.365
3	5.372	5.306	5.388	5.230	5.394	5.270	5.442	5.048
4	5.304	5.526	5.442	5.401	5.390	5.416	5.341	5.508
TIP	5.333	5.599	6.026	5.710	5.698	5.709	5.648	5.861

Table 21, Data Point 179 "Pre-Valley" Reduced Data

Ring Number	PAV (psia)	PAVLOW (psia)	DPC/P	DPR/P	Extent (Low) (degrees)	Extent (High) (degrees)	PFAV (psia)
1	5.701	5.589	0.0196	-0.0558	188.71	171.29	5.399
2	5.417	5.385	0.0058	-0.0032	187.21	172.79	5.399
3	5.303	5.218	0.0160	0.0179	131.72	228.28	5.399
4	5.313	5.266	0.0090	0.0160	216.69	143.31	5.399
5	5.264	5.207	0.0109	0.0251	155.43	204.57	5.399

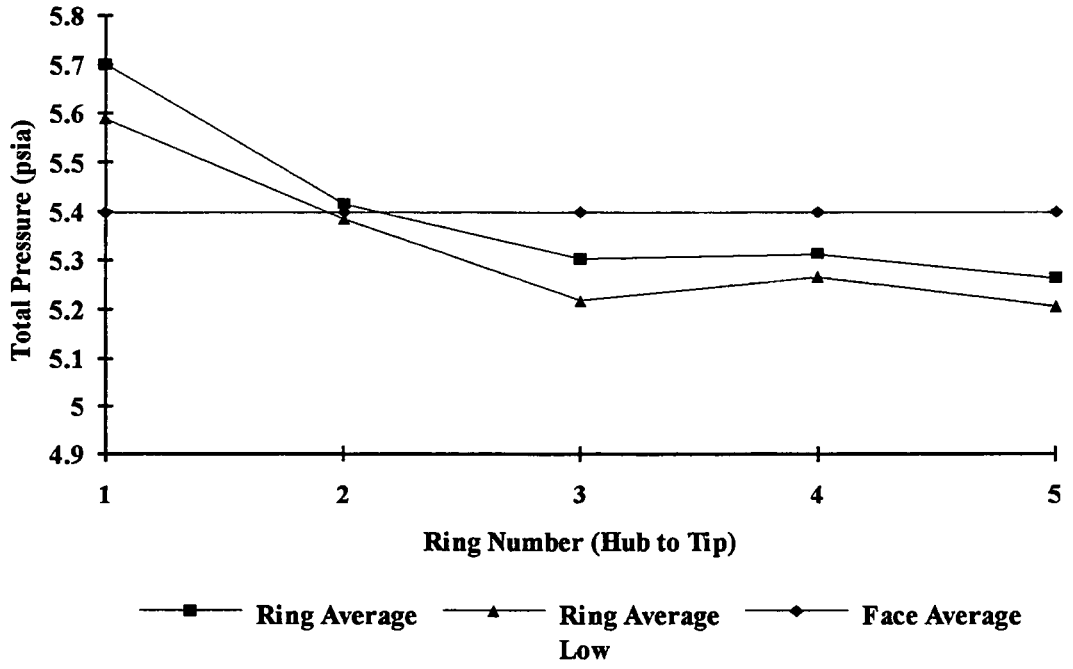


Figure 44, Data Point 179 "Pre-Valley" Ring Average Total Pressure

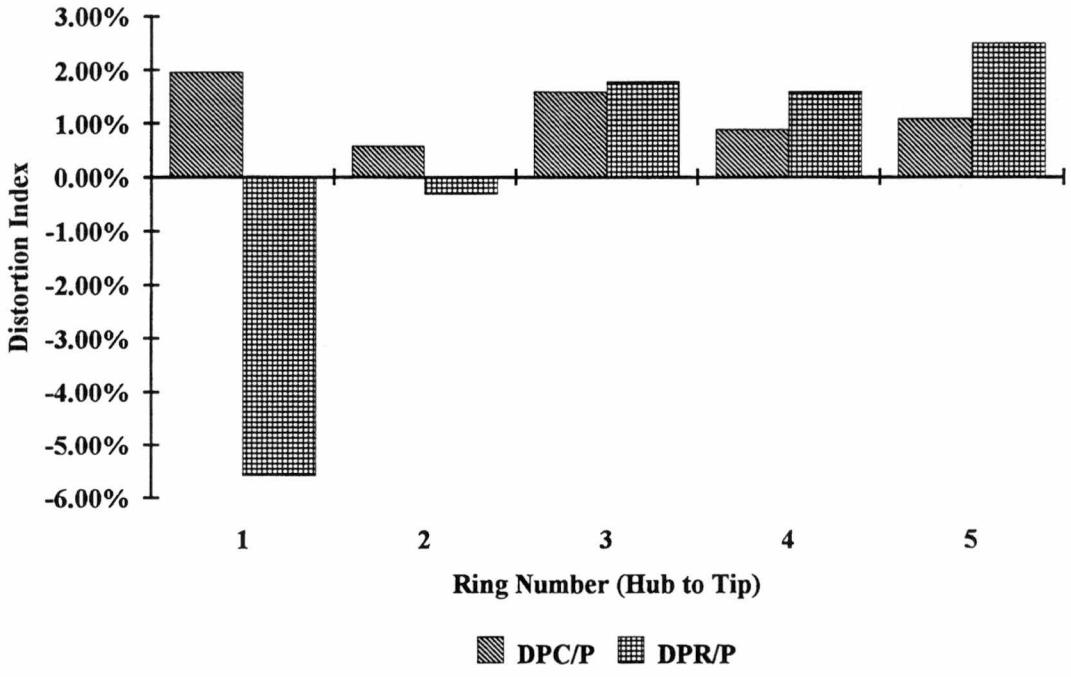


Figure 45, Data Point 179 "Pre-Valley" Circumferential and Radial Distortion Intensity

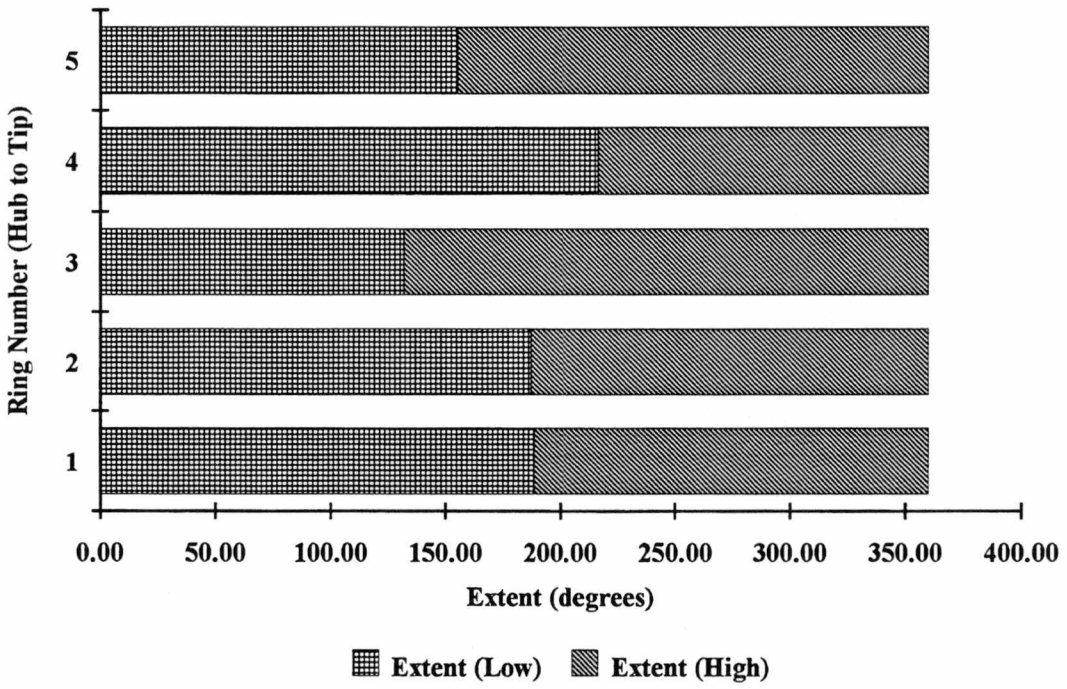


Figure 46, Data Point 179 "Pre-Valley" Circumferential Extent

Table 22, Individual Probe Pressures from Data Point 179 "Valley"

RAKE	A 14°	D 57°	G 99°	K 141°	N 184°	R 226°	T 268°	Y 332°
RING								
HUB	5.093	5.049	5.065	5.124	5.221	5.109	5.089	5.091
2	5.183	5.129	5.138	5.109	5.174	5.138	5.137	5.093
3	5.161	5.136	5.268	5.187	5.218	5.103	5.189	4.829
4	5.152	5.292	5.371	5.238	5.224	5.248	5.193	5.269
TIP	4.976	5.190	5.426	5.159	5.188	5.110	5.192	5.260

Table 23, Data Point 179 "Valley" Reduced Data

Ring Number	PAV (psia)	PAVLOW (psia)	DPC/P	DPR/P	Extent (Low) (degrees)	Extent (High) (degrees)	PFAV (psia)
1	5.190	5.131	0.0113	-0.0055	251.09	108.91	5.161
2	5.247	5.220	0.0053	-0.0167	180.71	179.29	5.161
3	5.129	5.006	0.0240	0.0063	113.26	246.74	5.161
4	5.136	5.121	0.0029	0.0048	236.92	123.08	5.161
5	5.104	5.082	0.0044	0.0110	205.13	154.87	5.161

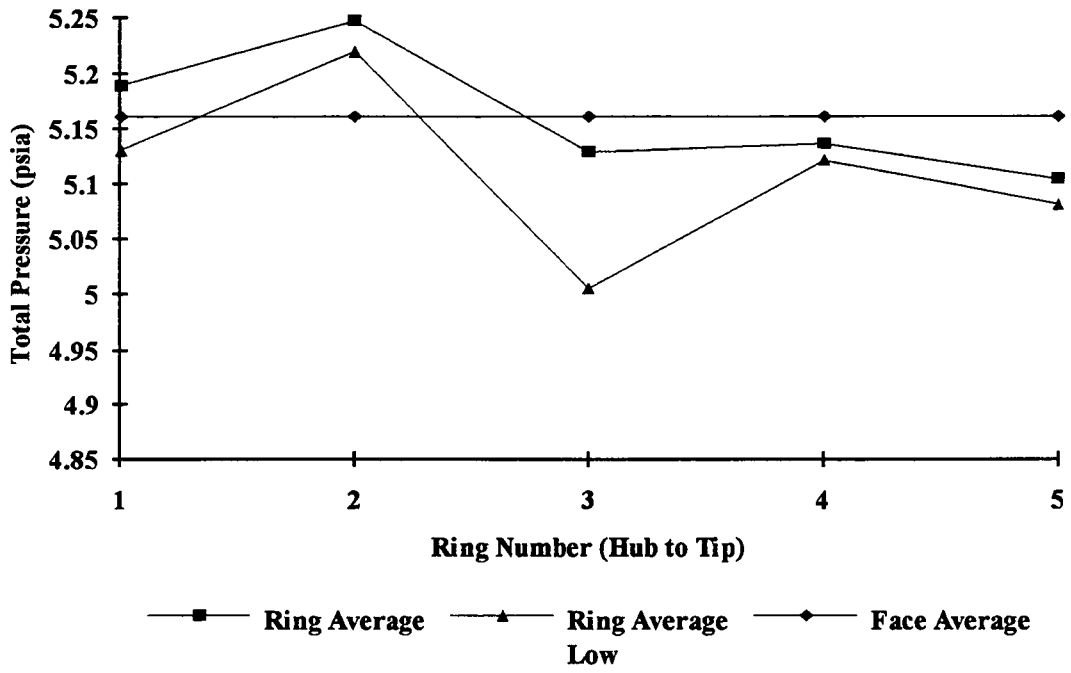


Figure 47, Data Point 179 "Valley" Ring Average Total Pressure

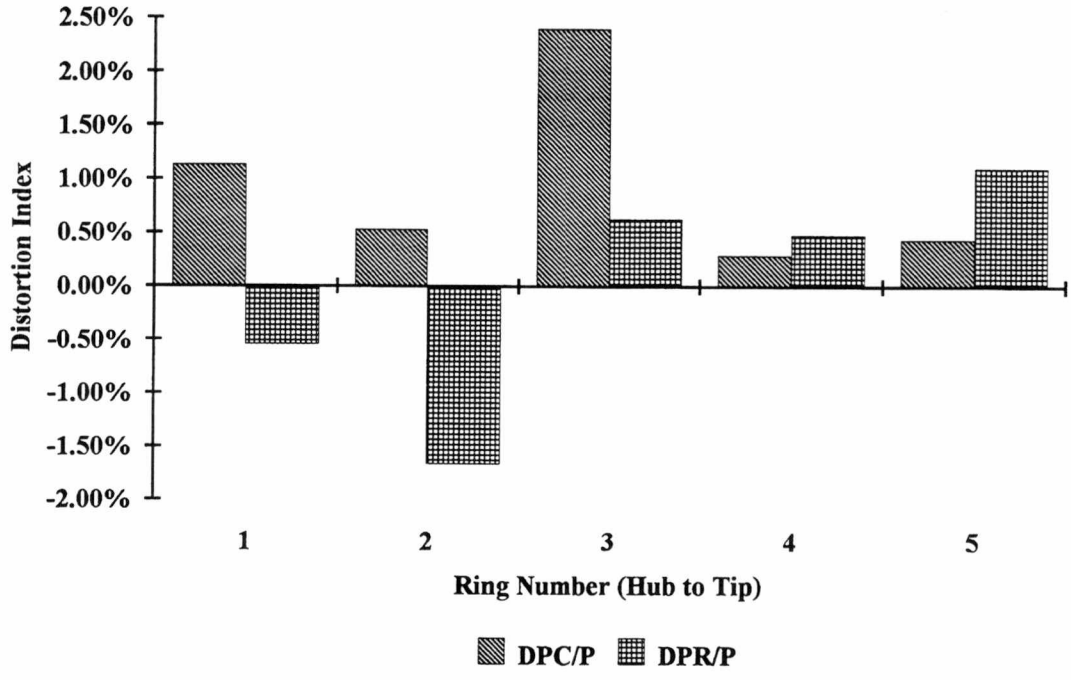


Figure 48, Data Point 179 "Valley" Circumferential and Radial Distortion Intensity

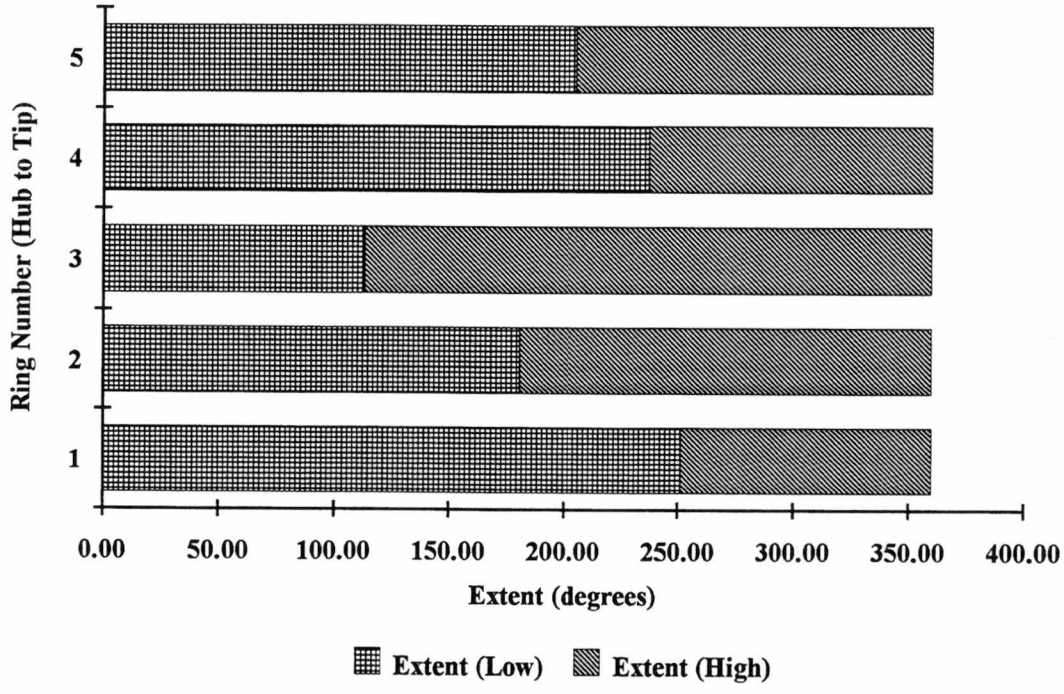


Figure 49, Data Point 179 "Valley" Circumferential Extent

Table 24, Individual Probe Pressures from Data Point 179 "Post-Valley"

RAKE	A 14°	D 57°	G 99°	K 141°	N 184°	R 226°	T 268°	Y 332°
RING								
HUB	5.216	5.192	5.257	5.129	5.188	5.071	5.147	5.057
2	5.145	5.296	5.204	5.362	5.269	5.204	5.090	5.060
3	5.180	5.195	5.493	5.397	5.222	5.132	5.137	4.805
4	5.285	5.273	5.571	5.315	5.252	5.308	5.269	5.193
TIP	5.095	5.375	5.516	5.269	5.276	5.195	5.282	5.203

Table 25, Data Point 179 "Post-Valley" Reduced Data

Ring Number	PAV (psia)	PAVLOW (psia)	DPC/P	DPR/P	Extent (Low) (degrees)	Extent (High) (degrees)	PFAV (psia)
1	5.274	5.220	0.0103	-0.0100	187.66	172.34	5.222
2	5.303	5.262	0.0078	-0.0156	159.73	200.27	5.222
3	5.182	5.046	0.0263	0.0077	176.15	183.85	5.222
4	5.196	5.108	0.0170	0.0049	263.91	96.09	5.222
5	5.154	5.111	0.0083	0.0130	239.15	120.85	5.222

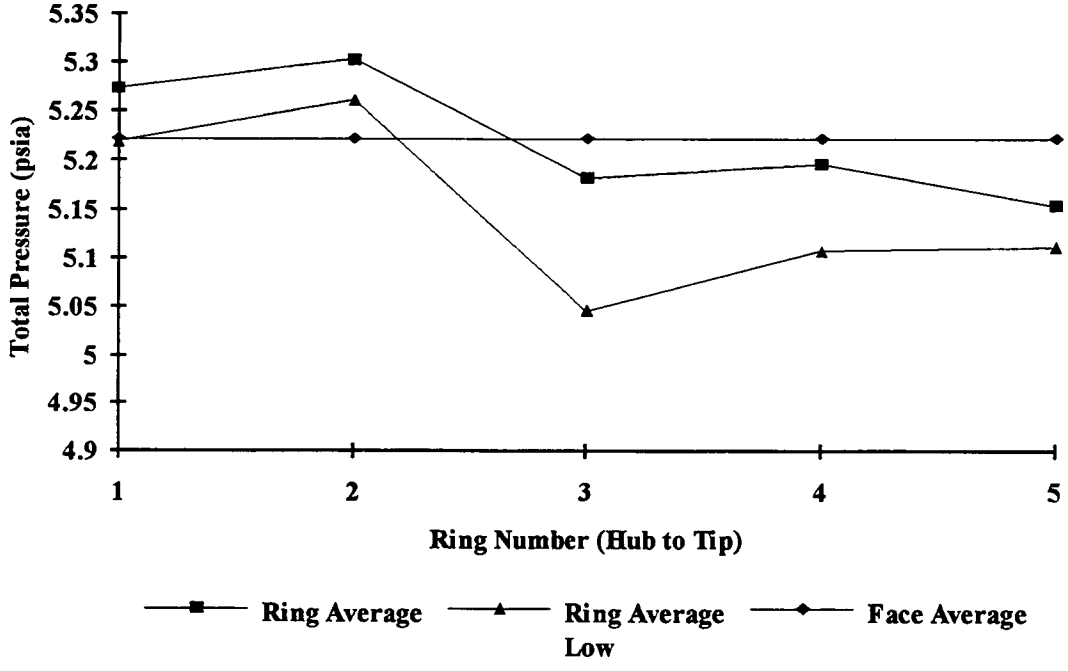


Figure 50, Data Point 179 "Post-Valley" Ring Average Total Pressure

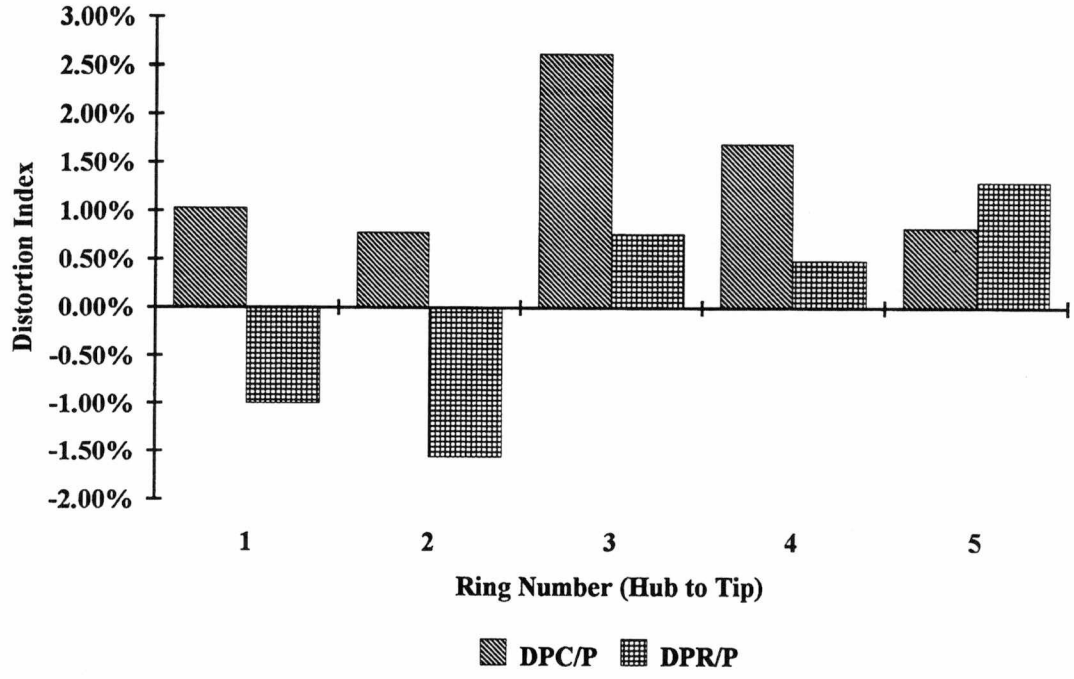


Figure 51, Data Point 179 "Post-Valley" Circumferential and Radial Distortion Intensity

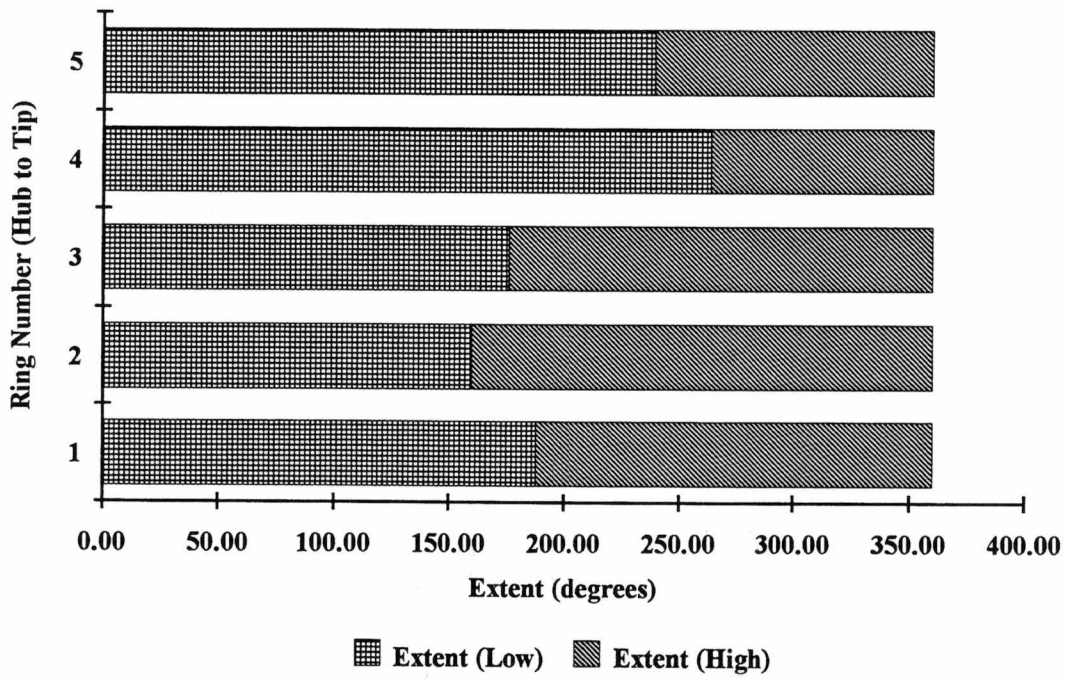


Figure 52, Data Point 179 "Post-Valley" Circumferential Extent

Table 26, Average Distortion Indices

Ring	Data Point 65 (DPR/P)	Data Point 179 (DPR/P)	Data Point 65 (DPC/P)	Data Point 179 (DPC/P)
1 (Hub)	-0.26%	-1.39%	1.88%	0.78%
2	-0.82%	-1.36%	0.75%	1.14%
3	-0.93%	0.76%	2.34%	1.02%
4	0.01%	0.46%	1.10%	0.76%
5 (Tip)	1.99%	1.52%	1.04%	0.67%

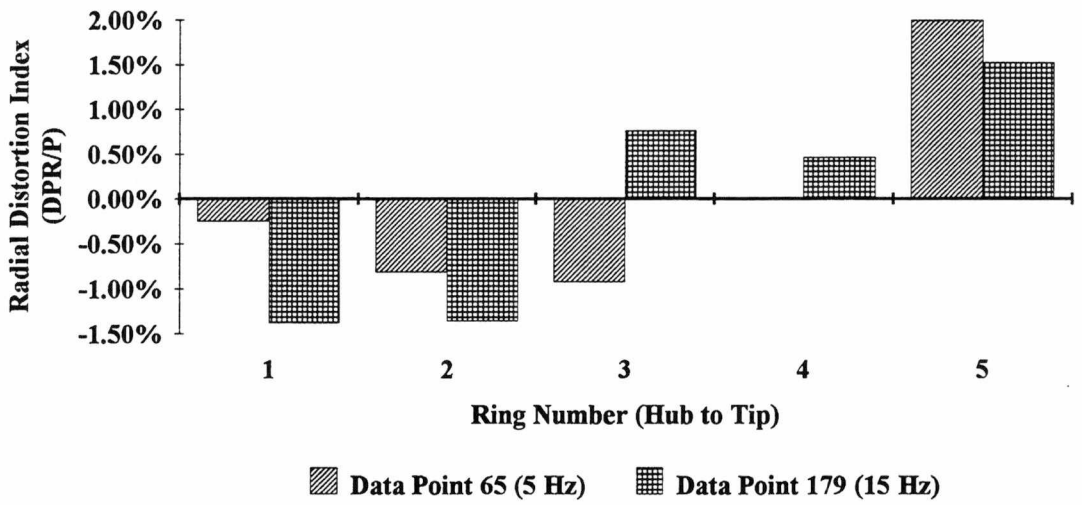


Figure 53, Average Radial Distortion for Data Points 65 and 179

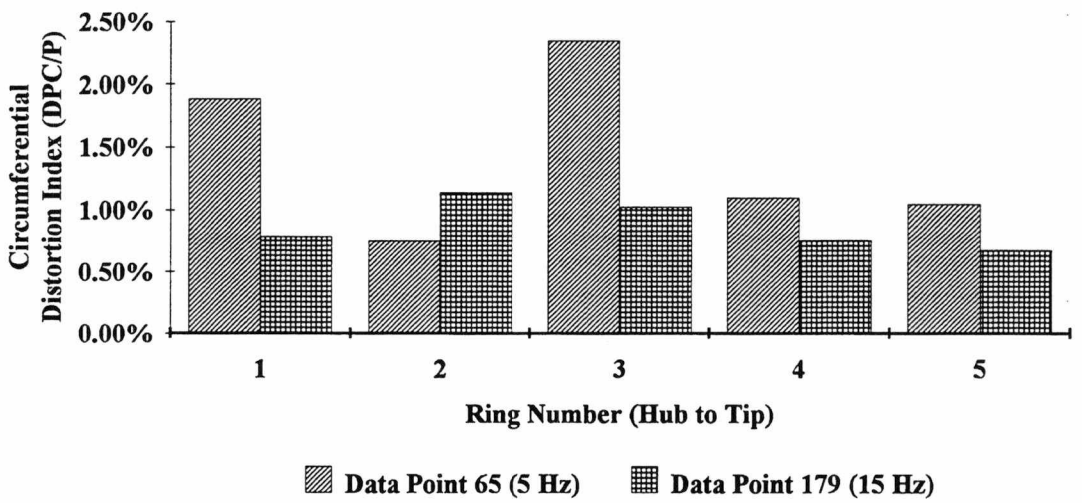


Figure 54, Average Circumferential Distortion for Data Points 65 and 179

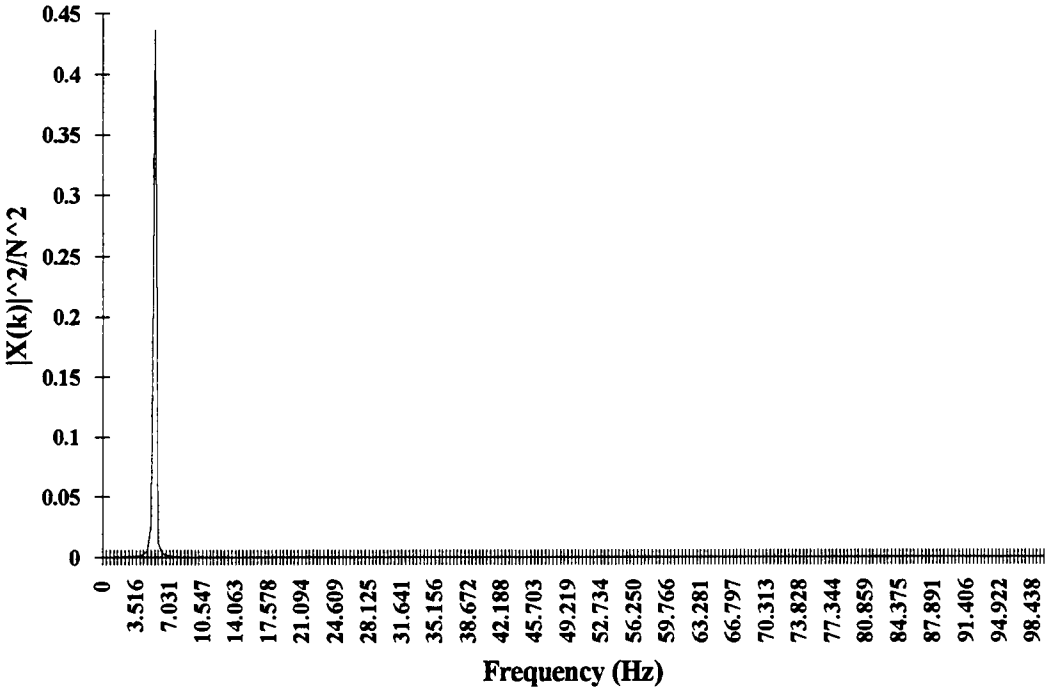


Figure 55, PSD of a 5 Hertz, Unity Amplitude, Cosine Wave

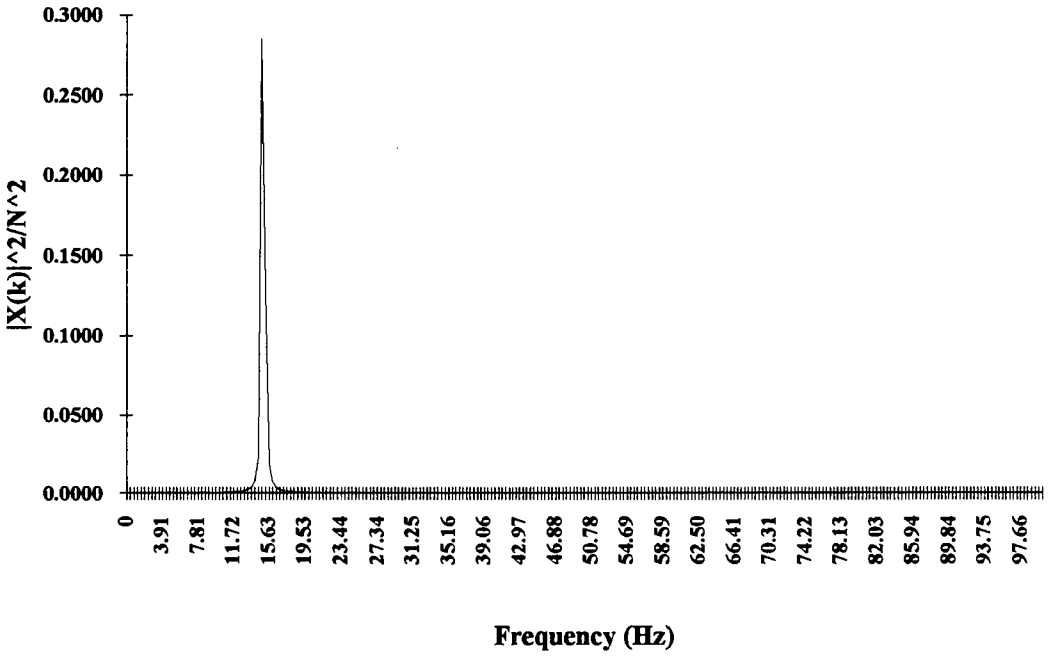


Figure 56, PSD of a 15 Hertz, Unity Amplitude, Cosine Wave

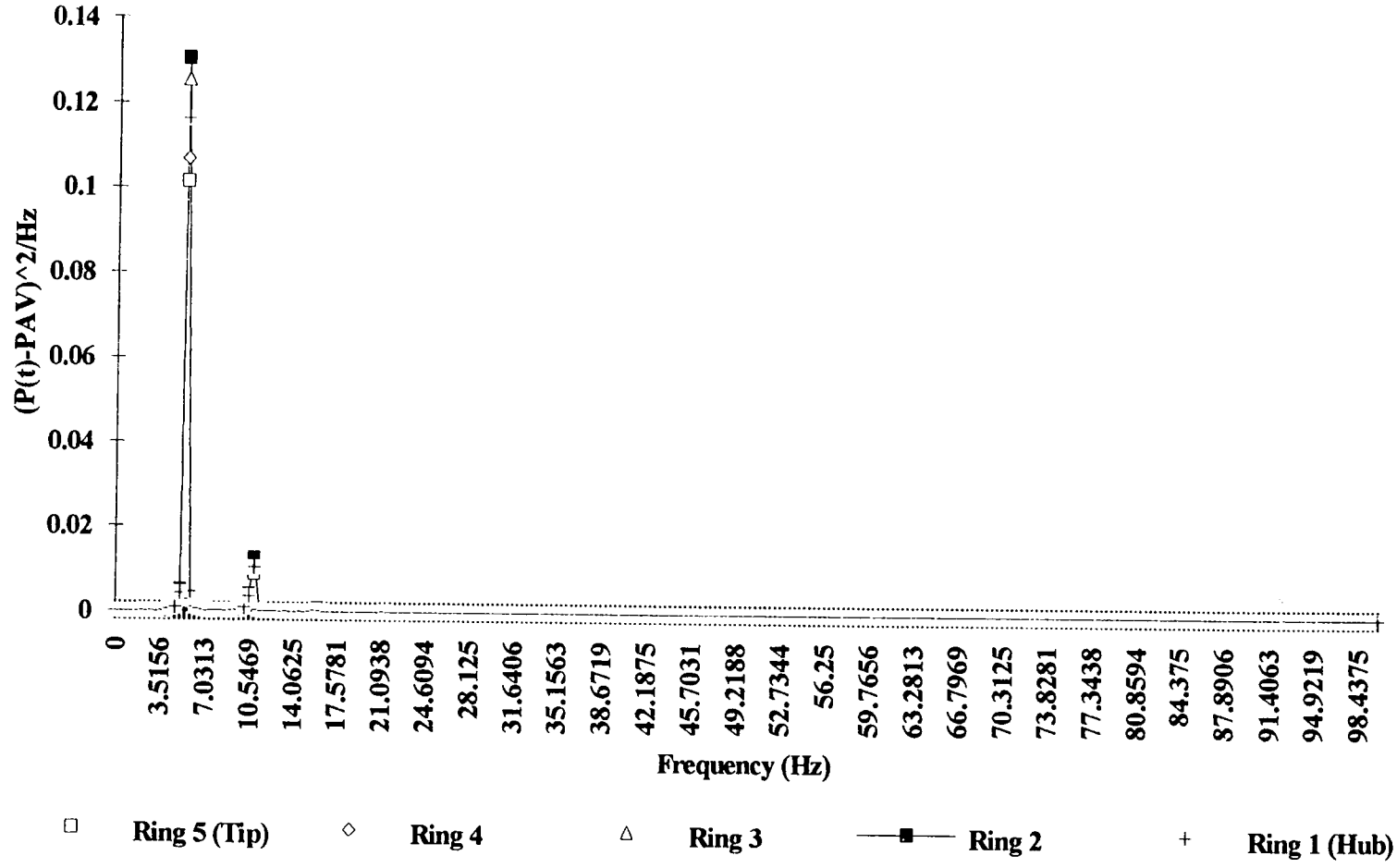


Figure 57, Data Point 65: 5 Hertz Planar Wave Power Spectral Density

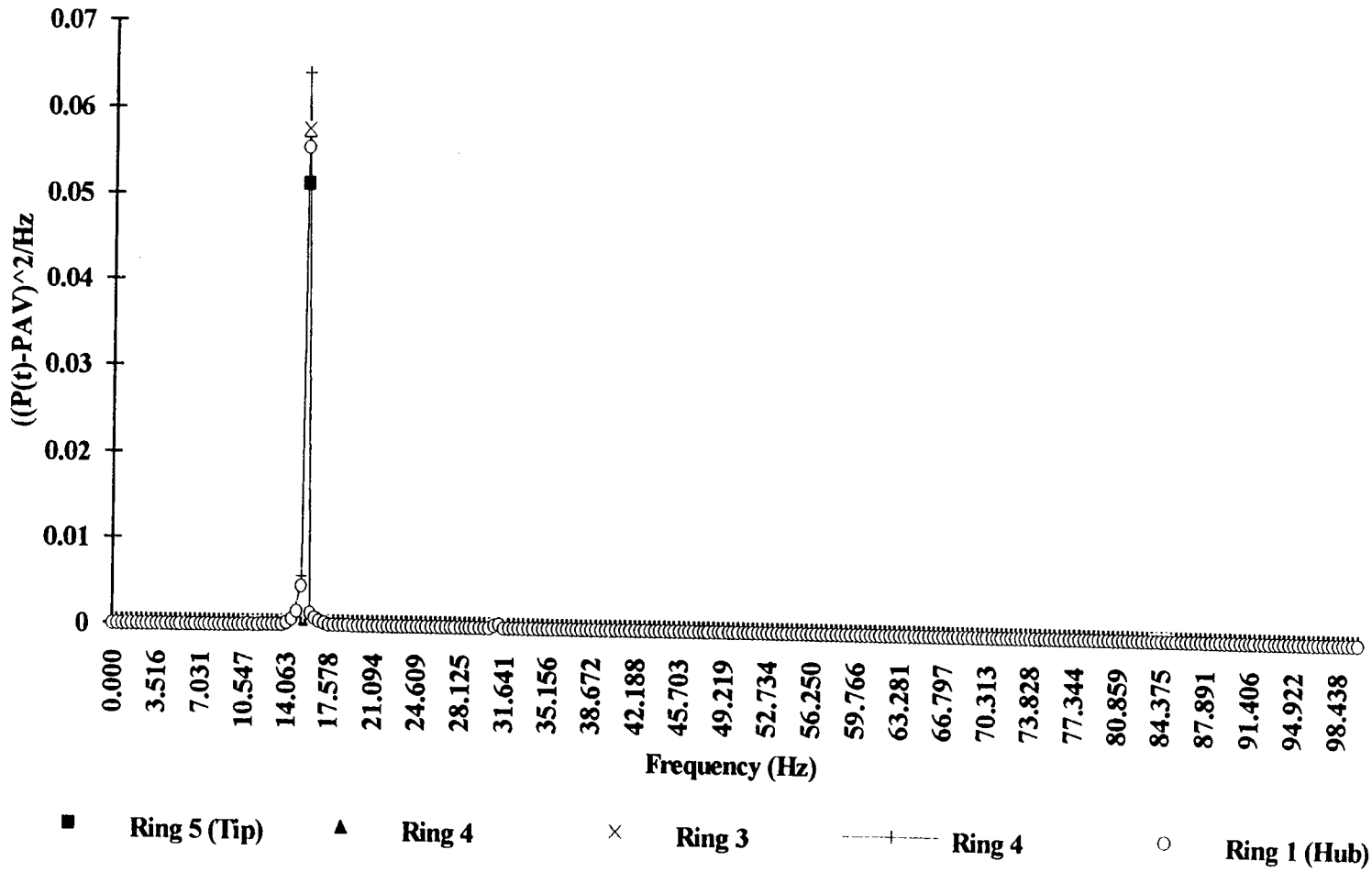


Figure 58, Data Point 179: 15 Hertz Planar Wave Power Spectral Density

VITA

Stanford Thomas Verigood was born in Pittsburgh, Pennsylvania on December 14, 1958. He graduated from Hopewell Area High School in June, 1976. The following October he enlisted in the United States Air Force and was assigned as a jet engine mechanic to Nellis AFB, Nevada. In 1984 he was selected for the USAF Airman's Education and Commissioning Program. The following May he entered the Pennsylvania State University and in May, 1988 received the degree of Bachelor of Science in Aerospace Engineering. He was commissioned a second lieutenant in the USAF in September, 1988. In January, 1989 he entered the University of Tennessee Space Institute at Tullahoma, Tennessee and in August, 1995 received a Master of Science degree in Mechanical Engineering.

He is presently employed as an Installation and Test Engineer with Sverdrup Technology Inc. at the Arnold Engineering Development Center near Tullahoma, Tennessee.